



The Effect of Accelerators on Vulcanization of Natural Rubber Compounds

Murat TEKER , Ayşe USLUOĞLU , Esra ÖZTURK 

Department of Chemistry, Faculty of Science, Sakarya University, Sakarya, 54050, TURKEY

Abstract: The effect of accelerator type on vulcanization characteristics and mechanical properties of natural rubber was investigated. Also, the effect of growing quantity of MBTS on vulcanization characteristics and mechanical properties of natural rubber was investigated. The results show that the fastest cure time is obtained with thiurams and dithiocarbamates for natural rubber. Sulphenamides, especially TBBS gives the best tensile strength. Elongation at break first increases by increasing dose of MBTS and then decreases. The higher elongation at break is obtained with DPG.

Keywords: Natural Rubber, accelerator, vulcanization, dithiocarbamates, thiurams, sulphenamides

Submitted: July 20, 2023. **Accepted:** December 06, 2023.

Cite this: Teker, M., Usluoğlu, A., & Öztürk, E. (2024). The Effect of Accelerators on Vulcanization of Natural Rubber Compounds. *Journal of the Turkish Chemical Society, Section B: Chemical Engineering*, 7, 1–12. <https://doi.org/10.58692/jotcsb.1330292>

*Corresponding author. E-mail: teker@sakarya.edu.tr.

1 INTRODUCTION

Rubber plant was first introduced by a French botanist, François Fresneau (Savran, 2001). Natural rubber is obtained from the latex of plant whose name is *Hevea Brasiliensis* (Bateman, 1963). Christopher Columbus realized that Haitian natives was playing with the ball made of rubber during these Cond voyage to America in 1492 (kaucuk.org; Sabu et al., 2014). Vulcanization is the way to get the elastomers which is known as a different type of rubbers. Also, vulcanization is the one of the most significant technology in the modern industry. The fundamental part of vulcanization is to provide to form chemical bounds or ties combining rubber macro-molecules and converting polymeric molecules to the cross-linked form (Hoffman, 1989). Formation of crosslink is the primary condition in order to emerge the elastomeric features of the rubber (Walker & Rader, 1988). It is the most essential characteristic of an elastomer that is recovering the previous state in the following of the processes of tension or compression. In addition to this, the accelerators have the most vital role during the reaction of vulcanization by reducing the time (Susamma et al., 2001; Akiba & Hashim, 1997). Similarly, sulfur can be beneficial for the reaction of vulcanization, but that is neither profitable as commercially nor time-saving without accelerators (Sadequill et al.,

1998). Moreover, the type and quantity of accelerators and the ratio of sulfur-accelerator have a different effect on the value of hardening of rubber and its mechanical properties (Ismail et al. 2003; Fan et al. 2001; Pongdhorn et al. 2001).

NR has high rate of cross-linking along vulcanization. Natural rubber provides a good interference with other non-polar rubber because of non-polar formation. In addition, if it is intermixed by both SBR (styrene butadiene rubber) and BR (butadiene rubber), the resistance of abrasion & heat and properties of low heat is increased (Joseph et al., 1988). Similarly, in case of mixing with NBR (nitrile rubber) the endurance to oil and fuels can be enhanced and mixing with chloroprene rubber provides high air resistance (Sirishina et al., 2001; Choi, 2002).

The products from rubber a have great importance in every part of our lives. The achievement of this product depends on the interference of correct polymers, rubber chemicals and extenders with suitable ratios (Loyd, 1976).

There are principally as what we call a prescription goes like rubber, sulfur, zinc oxide, fatty acid, accelerator, extender, softener, and anti-oxidant (Savran, 2001; Singh et al., 2015).

The effect of extender substances on textures of rubber in regard to strengthening can be monitored by measuring two main features of extenders which are ultimate strength and the value of modulus (Choi et al., 2003). The energy needed to break up rubber by stretching is getting greater when the value of modulus of rubber increases. Bonding between extender and polymer is related with their surface energy and active functional groups and the extender's surface energy should be same with polymer's one or more than that. The highest power gained by rubber is provided by carbon black as an extender. Primary extender substances used in rubber industry is calcium carbonate, clay, talcum, silica(s), zinc oxide, and so on (Gungor, 2022).

Accelerators are used to make fast cross-linking between polymer chains by means of sulfur. Accelerators and activators create active accelerator complex and this complex forms active sulfurization compound. This active compound provides cross-linking between polymer chains (Puspitasari & Cifriadi, 2019). The choice of accelerators and other chemicals is connected with the type of elastomers and intended performance characteristics (Frederick & Eirich, 1978).

The speed of vulcanization is affected by pattern of rubber as well as accelerator texture. Number of double bonds in polymer and the allylic hydrogen count influence the rapidity of vulcanization. Entropy starts to fall down due to too much reactive groups which is also let the ratio of reaction enhance. Furthermore, vulcanization reaction are diffusion-controlled reactions. Zinc-accelerator complex should be diffused into the elastomer (Mostoni et al, 2019). As the surface area of zinc-accelerator complex grows, the diffusion speed and in this way, the vulcanization rapidity drops (Kresja & Koenig, 1993).

In this study, the features of vulcanization of the mixtures of natural rubber by using different accelerators and the features of this after vulcanization was examined. Also, it was investigated that how the physical characteristic of the mixture of natural rubber can be changed with varied amount of accelerators during vulcanization and after vulcanization.

2. EXPERIMENTAL SECTION

2.1. Materials and Method

The structure of natural rubber is 99% cis- and 1,4% trans- poly isoprene (Bateman, 1963).

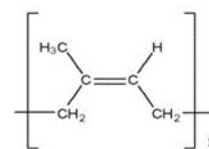


Figure 1: The structure of natural rubber (NR).

The presence of double bonds is necessary for vulcanization of sulfur. Nevertheless, this double bonds cause to aging effect by reacting with oxygen and ozone. Since the heat resistance of those is low, there is a tendency to reverse during vulcanization. Poly sulfidic crosslinks are thermally unstable and they are degraded into mono- or di-sulfidic links. The name of this process is called as reversion. In order to prevent this, the procedure of vulcanization should be carried out at low temperatures and hardening should be checked. Even though the unsaturation rate is various, there is an increment in mechanical performance (Sirqueira & Soares, 2003).

Initial: In this step, a free sulfur atom is degraded and amine is formed with MBT. Active sulfur is taken place as a result of reaction between amine and sulfur. It is also obtained that there is a reduction in the amount of sulfonamide in consequence of formation of accelerators & sulfur accelerator-poly-sulfite and di-sulfite. Until poly-sulfites reach at maximum level, this step ends.

Activation: Poly-sulfites' accelerator and di-sulfites begin to decrease and it is obtained some formations such as MBTSx. This step goes on until the accelerator is out.

Sulfurization and cross-linking: At the level of sulfonamide, di- and poly-sulfite is finished, polymeric bonds with the sulfur and cross-link is formed at the same time.

Aging and Reversion: When free sulfur runs out, accelerator complex goes on to reaction with cross-links which is poly-sulfidic. These reactions are as follows: Removing the sulfur from cross-links, breaking cross-links, development of cyclo-sulfur structure, formation of conjugate unsaturation in polymer, and collapsing zinc-sulfite.

2.2. Used Materials

SMR 10 CV and Dutralter 4038 as natural rubber and EPDM were used, respectively. Carbon blacks are labeled as FEF N 550 and HAF N 330. Along with these, accelerators used are MBT (2-mercaptobenzothiazole) MBTS (dibenzimidazole disulfur), CBS (N-cyclohexyl-2 benzimidazole sulfonamide), MBS (2-benzimidazole-N-sulfene morpholine), TBBS (N-tertiary butyl-2 benzimidazole sulfonamide), TMTD (tetramethylthiuram disulfide), TMTM (tetramethylthiuram monosulfide), ZDMC (zinc dimethyldithiocarbamate), ZDEC (zinc

diethyldithiocarbamate), ZEPC (zinc ethyl phenyldithiocarbamate), DPG (diphenylguanidine).

2.3. Preparation of Rubber Mixture

The mixture was prepared in the open laboratory two cylindered shaft. (ASTM D3182).

In the first trial, Natural rubber and various accelerators and a series of mixture were attained. There was a mixture prepared from the union of natural rubber. This mixture contains natural rubber 100 phr, Carbon Black 78.94 phr, Aromatic oil 6.31 phr, Zinc oxide 6.31 phr, stearic acid 1.84 phr, sulfide 1.00 phr, different accelators (MBT, MBTS, CBS, MBS, TBBS, TMTD, TMTM, ZDCM, ZDEC, ZEPC, DPG) 1 phr. Phr stands for parts per one hundred rubber.

In the second trial, different amounts of MBTS were used as accelerators and tests were performed. The recipe contains natural rubber 100 phr, Carbon Black 78.94 phr, Aromatic oil 6.31 phr, Zinc oxide 6.31 phr, stearic acid 1.84 phr, sulfide 1.00 phr, different amounts (0.40-0.60-0.80-1.00-1.20-1.40-1.60) of MBTS.

2.4. Used Devices and Features

2.4.1. Rheometer

It is used to measure the vulcanization characteristics of mixtures and to save vulcanization curve. It also applies oscillating stretch into mixture under high temperature and pressure and as a consequence of increase in a cross-link's intensity, an increment in torque is shown as a function of time. The unit of torque is N-m or lb-in (pounds inch) (Rader, 1985).

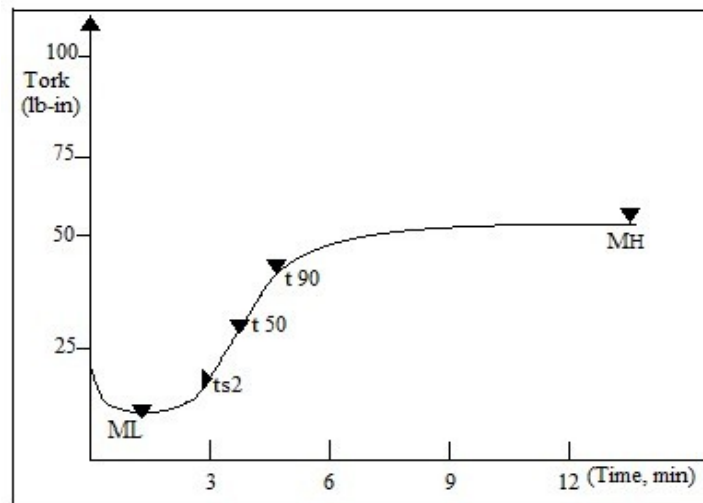


Figure 2: Graphic of curve of vulcanization.

Ts2 : Pre-vulcanization, Beginning time of hardening (scorch time) (min.)

MH : Maximum torque

T90 : Time when 90% of the maximum torque is reached (min)

ML : Minimum torque

Vulcanization state which is made ready with each distinctive accelerators was gauged by MDR-2000

Rheometer device. (ASTMD 5289). NR mix was tested throughout 5 minutes at 180 °C (Table 1). Later, hardening characteristics of NR mixture blended with a changing amount of MBTS was measured by Rheometer in the condition of 5 minutes and at 180 °C. (Table 2). (Teker et al, 2008).

Table 1 : The feature of vulcanization of NR mixture prepared with different types of accelerators.

	MBT	MBTS	CBS	MBS	TBBS	TMTD	TMTM	ZDMC	ZDEC	ZEPC	DPG
ML (lb-in)	2.00	1.73	1.45	1.83	1.74	1.33	1.28	1.54	1.46	1.29	1.48
MH (lb-in)	8.04	8.20	11.35	11.67	11.52	12.60	11.34	9.64	8.44	8.04	6.93
t90 (min)	1.38	1.28	1.47	1.75	1.59	0.69	0.94	0.61	0.73	0.76	1.46
ts2 (min)	0.57	0.57	0.70	0.75	0.69	0.41	0.62	0.36	0.43	0.41	0.53

Table 2: The feature of vulcanization of NR mixture prepared with changing amount of MBTS.

	MBTS of amounts (phr)					
	0.40	0.60	0.80	1.00	1.20	1.60
ML (lb-in)	1.51	1.30	1.83	1.51	1.86	1.84
MH (lb-in)	7.57	7.84	9.35	9.42	10.16	10.99
t90 (min)	1.57	1.35	1.24	1.12	1.10	1.02
ts2 (min)	0.60	0.56	0.57	0.60	0.59	0.60

2.4.2. Shoremeter

Followed by vulcanization, the toughness measurement was carried out with a Braiss Shore A Durometer (ASTM D2240). The results are given in Tables 3 and 4.

2.4.3. Tensometer

This apparatus makes an indication of both extension of product at the time of failure and fracture resistance of product after vulcanization. The thickness of sample cut as bow-tie was measured from three different part and it was hanged on between two wangs of tensiometer and the power was applied into sample. At the time of failure of sample, tensiometer saves failure-extension curve and gives the values of them.

Breaking Point: Ratio of forces between at the time of failure and at the of beginning.

Breaking Elongation: Ratio of length between changing at the failure and changing at the beginning.

Modulus: The amount of unit surface for the force applying for a specific extension.

3. RESULTS AND DISCUSSION

3.1. The Effect of Accelerators on Features of Natural Rubber Mixture

Vulcanization characteristics of natural rubber mixture prepared with different accelerators obtained after rheometer test were compared with the physical features of the ones obtained by tensiometer test after vulcanization.

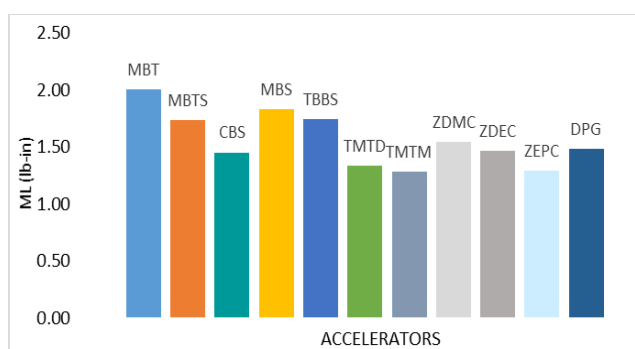
**Figure 3:** The effect of accelerators within natural rubber mix on ML value.

Table 3: The feature of vulcanization of NR mixture prepared with different type of accelerators.

	MBT	MBTS	CBS	MBS	TBBS	TMTD	TMTM	ZDMC	ZDEC	ZEPC	DPG
Hardness (Shore A)	58	59	62	59	65	62	62	63	61	61	53
Modulus (MPa)	10.17	10.59	15.64	13.72	16.74	15.90	15.46	13.03	11.26	10.71	7.19
Breaking strength (MPa)	16.53	17.82	21.46	20.90	23.18	18.60	19.79	20.62	19.15	17.94	12.39
Elongation at break (%)	417.9	473.4	414.9	445.5	423.8	355.7	381.7	477.8	479.6	462.2	446.1

Table 4: The feature of vulcanization of NR mixture prepared with changing amounts of MBTS.

	Amounts of MBTS (phr)					
	0.40	0.60	0.80	1.00	1.20	1.60
Hardness (Shore A)	53.00	55.00	56.00	57.00	59.00	60.00
Modulus (MPa)	8.56	9.53	11.20	18.95	20.04	20.18

According to Figure 3, The maximum ML value is provided with MBT, whereas the minimum ML value is carried out with TMTM and ZEPC.

As indicated in Figure 4, the maximum and minimum MH value is respectively reached by TMTD and DPG. With the TBBS, and sulfur donor, TMTD, a

quite high MH value is achieved. Similar results were obtained with previous studies. The highest MH values were obtained with TBBS and TMTM, while the lowest MH value was obtained with DPG. (Setyadewi et al. 2020). Also, the same features of dithiocarbamide providing rapid hardening is quite weak for rubber.

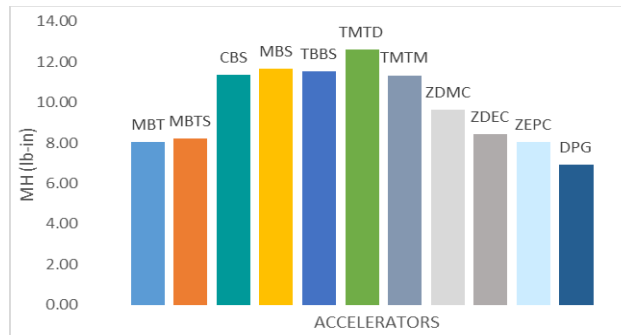


Figure 4: The effect of accelerators within natural rubber mix on MH value.

In Figure 5, the lowest hardening time, i.e., providing fastest hardening group, belongs to ZDMC and TMTD. The longest hardening time is given by sulfonamide group and DPG. Dithiocarbamate accelerators are used as ultra-fast accelerator for NR latex based compounds. Similar observations were presented in research work published by Formela et al. (2015).

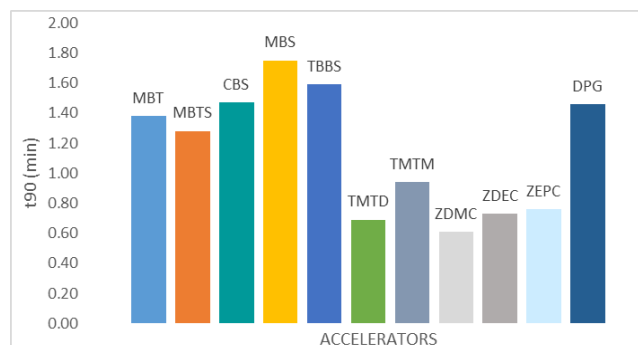


Figure 5: The effect of accelerators within natural rubber mix on t₉₀ value.

As demonstrated in Figure 6, sulfonamide has the safest processing related with the highest value of ts₂. Amines also facilitate the conversion of elemental sulfur (S₈) and/or polysulfide into active open chain sulfur through ring opening reaction. Amines might attack polysulfidic crosslink, either by direct reaction or by HS- generation (Heideman et al., 2004).

Also, TMTD and dithiocarbamide groups are the fastest one starting to harden. In another similar study, the lowest T90 and ts₂ values were obtained using TMTD accelerator (Koc&Tuken, 2019). Generally, TMTD accelerated vulcanization offers

short scorch time as TMTD is designated as an ultra-fast accelerator (Samarasinghe et al., 2020).

The comparison of toughness values after vulcanization is shown in Figure 7. According to that, the lowest is with DPG. Whereas the highest toughness value is with TBBS. ZDMC, Thiuram have also shown high hardness values. The crosslink density of rubber vulcanized also affects the hardness value. Their high stiffness was caused by the decreased mobility of polymer chains, what was also confirmed by the values of hardness and elongation-at-break (Nabil et al., 2014).

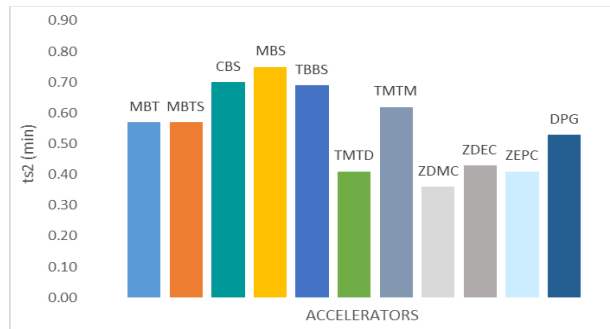


Figure 6: The effect of accelerators within natural rubber mix on ts₂ value.

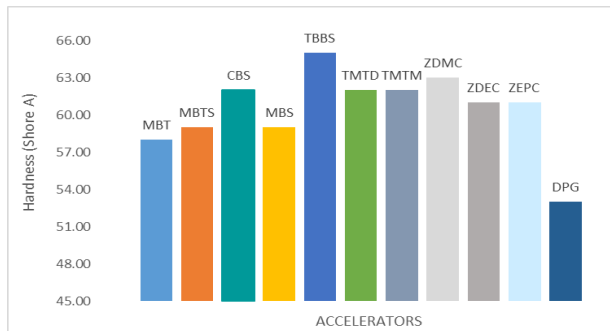


Figure 7: The effect of accelerators within natural rubber mix on hardness value.

The modulus value obtained with different accelerators is displayed in Figure 8. The top number of the modulus is materialized with thanks to TBBS, ZDMC and thiuram. In the study of Markovic et al. (2009), in the mechanical

comparison of MBT, TMTD and CBS in NR/CSM mixtures, it was found that mixtures made with TMTD had higher tensile strength values (Markovic et al., 2009).

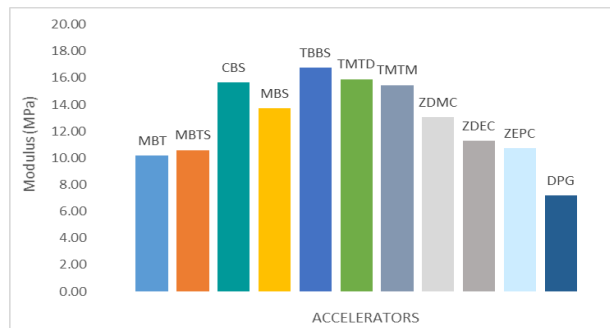


Figure 8: The effect of accelerators within natural rubber mix on modulus value.

The highest breaking strength is provided by TBBS and other sulfonamide. The comparison of these values are given in Figure 9. In contrast, the minimum value happens with DPG. However, it is

realized that the strengthening properties of DPG used generally as secondary accelerator is low. This is due to the chemical structure of DPG. (Formela et al., 2015)

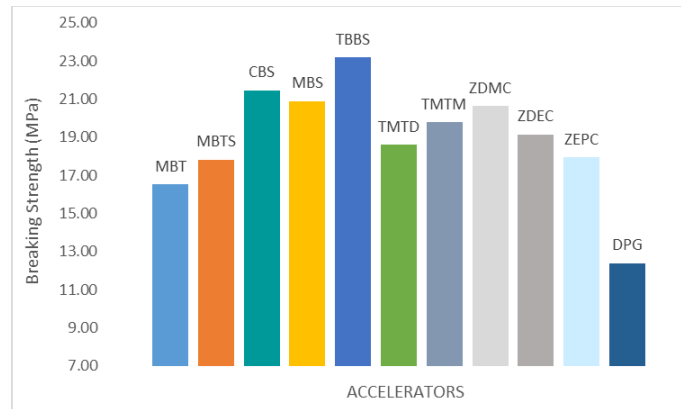


Figure 9: The effect of accelerators within natural rubber mix on breaking strength value.

When the elongation amounts are compared, the maximum and minimum level is respectively given by dithiocarbamate and thiuram groups (Figure 10). Compared to Figures 7, 8, 9, 10, as the hardness increases, the breaking strength increases, elongation decreases. High hardness can be evaluated as providing high crosslink density of

these groups. The high crosslink density causes the molecular chains to move less. Similar results were obtained in the study conducted by Comez et al. with Thiuram changes, the highest hardness and breaking strength values and the lowest elongation values are observed (Comez & Ozturk, 2023).

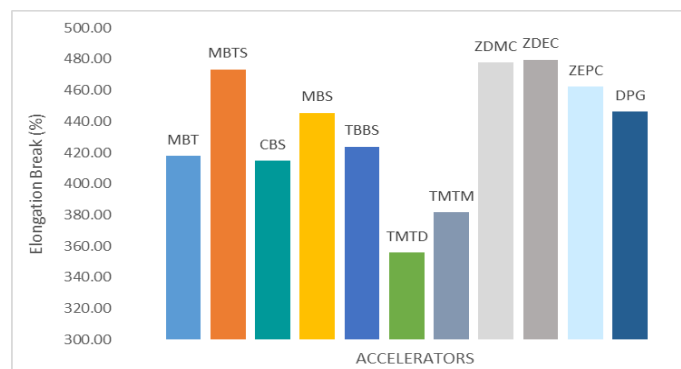


Figure 10: The effect of accelerators within natural rubber mix on elongation value.

Change in ML amount and MBTS increase in natural rubber mixture prepared according to rise in MBTS portion is demonstrated in Figure 11. ML value is

not changed more as the quantity of accelerators is varying. The cause for that can be said as being affected by mixing condition within the shaft.

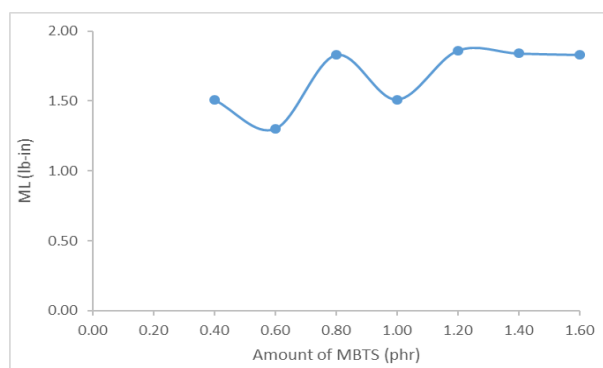


Figure 11: The change in ML value depending increase in MBTS.

As seen in Diagram 12, MH figure is generally raised with the portion of accelerators used. On the other

hand, after this level, there is no such a tremendous change.

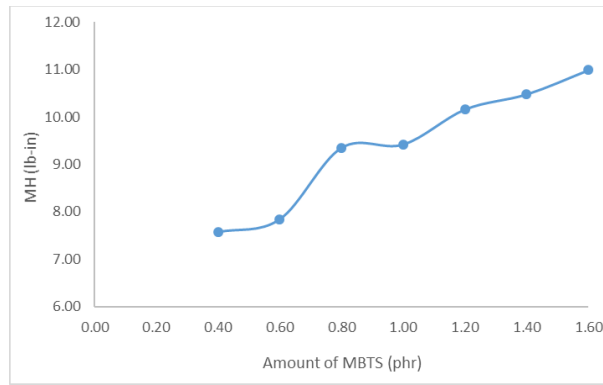


Figure 12: The change in MH value depending an increase in MBTS.

While the amount of accelerators increases, t90 value decreased as shown in Figure 13. In other words, vulcanization is accelerated.

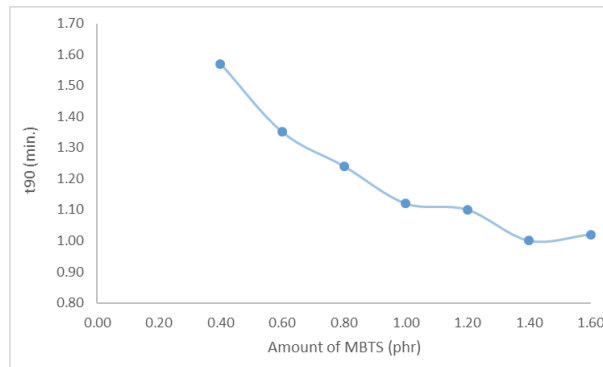


Figure 13: The change in t90 value depending an increase in MBTS.

Ts2, the time to start hardening, becomes shorter a little bit as the accelerator portion is gone up, but then, it raises and does not undergo a change so much. The values are compared in Figure 14.

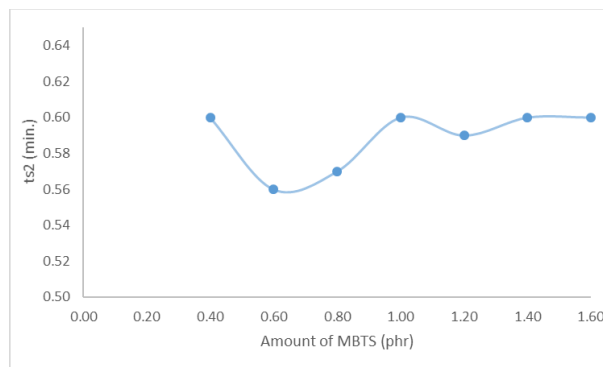


Figure 14: The change in ts2 value depending increase in MBTS.

The crosslink density of rubber increases with the rise in the amount of accelerators. So, hardness values increase.

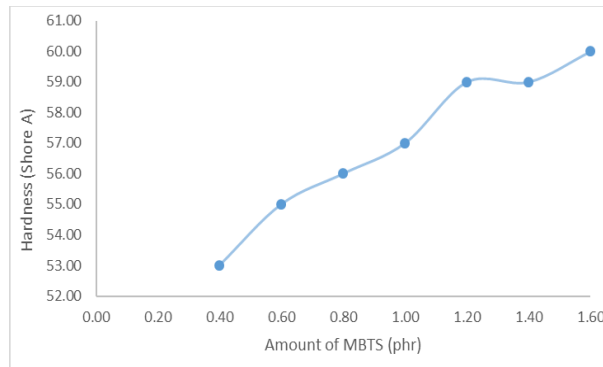


Figure 15: The change in toughness value depending increase in MBTS.

Modulus values increase with the rise in the amount of accelerators, but then, they do not undergo a

change so much. The change in modulus value depending increase in MBTS is shown in Figure 16.

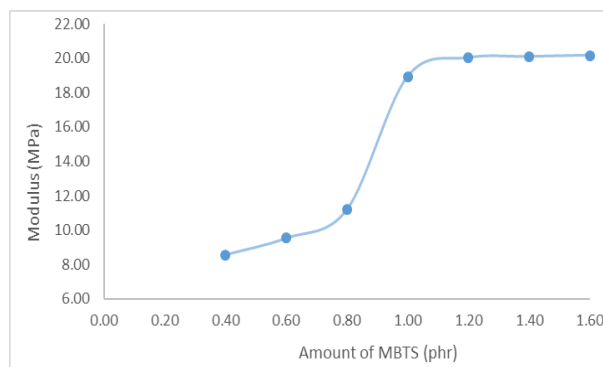


Figure 16: The change in modulus values depending increase in MBTS.

4. CONCLUSION

ML value named as number of minimum torque depends on mixing condition and time. ML values give an idea about the viscosity of mixture. For the natural rubber, the medium level accelerator provides high ML values, whereas rapid level accelerator gives low ML values. The lowest ML values were obtained for Thiuram and dithiocarbamate groups. The number of ML is interrelated with physical features such as stretching, breaking, and tearing resistance. The highest MH values were obtained with TBBS and TMTM, while the lowest MH value was obtained with DPG. TBBS among all sulfonamide provides the highest cross-linking intensity as an accelerators. Therefore, it shows good enough strength characteristics. Also, thiuram gives good cross-linking intensity in conventional systems and thus, they provide great breaking strength values. As a result of this, thiuram and sulfonamide having the highest MH values indicates sufficient breaking strength and modulus properties. Moreover, zinc dithiocarbamides give good breaking strength. Toughness features proportional with cross-linking intensity are also high in the mixture prepared with thiurams, dithiocarbamides, and TBBS. The minimum t90 value is obtained with thiurams and

dithiocarbamides whose rapidity of vulcanization is great. On the contrary, medium level accelerators such as mercapto compounds and sulfonamides give longer t90 value. Sulfonamide giving quite late activation of vulcanization provides the greatest ts2 values. Dithiocarbamides whose processing safety is pretty low and which reacts rapidly indicates very low ts2 values. In other words, they react as quickly as possible.

In the studies regarding to variance in the amount of MBTS, if the portion of acceleration increases, t90 value goes down, i.e., vulcanization steps up. As the intensity of cross-linking bond is gathered, MH quantity also rises and thus, breaking strength, modulus and toughness level increase, too. Additionally, ML and ts2 values are not affected so much from such kind of changes. Hence, the stability can not happen. At the beginning the elongation content is advanced because of similarities in the value of sulfur and accelerators & excess poly-sulfidic bonds. Later on, it can be diminished due to acting as an active system. Until the MBTS proportion reaches to the level as 1.6 phr, either MH or fall in toughness may be clarified with reversion.

Finally, while the cross-linking intensity increases, breaking strength, modulus, toughness values rises, too. Increment in this textures is generally directly proportional to augmentation in MH value. When t90 is short enough, MH becomes dominant, so intensity of cross-linking bond of rapid accelerators is greater. Elongation portions for natural rubbers except dithiocarbamate groups generally decreases as the time of vulcanization becomes shorter.

5. CONFLICT OF INTEREST

The authors declare no conflict of interest.

6. REFERENCES

- Akiba M. & Hashim A.S., (1997). Vulcanization and Crosslinking in Elastomers, *Prog. Polym. Sci.*, 22, 475-521. [https://doi.org/10.1016/S0079-6700\(96\)00015-9](https://doi.org/10.1016/S0079-6700(96)00015-9).
- Bateman L. (1963). *The chemistry and physics of rubber-like substances*. Maclaren London – Wiley Newyork.
- Choi S.S. (2002). Improvement of properties of silica-filled natural rubber compounds using polychloroprene, *J. Appl. Polym. Sci.* 83, 2609-2616, <https://doi.org/10.1002/app.10201>
- Choi S.S., Nah C., Lee S.G. & Joo C.W. (2003). Effect of filler-filler interaction on rheological behaviour of natural rubber compounds filled with both carbon black and silica, *Polym. Int.* 52, 23-28. <https://doi.org/10.1002/pi.975>.
- Comez E.E., Ozturk S., (2023), Investigating Rheological, Mechanical and Heat Aging Effects of Different Accelerator Systems at EPDM Compounds Investigating Rheological, Mechanical and Heat Aging Properties of Different Accelerator Systems at EPDM Compounds, *International Journal of Engineering Research and Development UMAGD*, 15(2), 654-664.
- Formela K., Dominik W.S., Formela M., Hejna A., Haponiuk J., (2015). Curing characteristics, mechanical and thermal properties of reclaimed ground tire rubber cured with various vulcanizing systems *Iran Polym J* 24:289-297. DOI 10.1007/s13726-015-0320-9
- Fan R. L., Zhang Y., Li F., Zhang Y. X., Sun K. & Fan Y. Z. (2001). Effect of high-temperature curing on the crosslink structures and dynamic mechanical properties of gum and N330-filled natural rubber vulcanizates, *Polymer Testing* 20, 925-936. [https://doi.org/10.1016/S0142-9418\(01\)00035-6](https://doi.org/10.1016/S0142-9418(01)00035-6)
- Frederick R. & Eirich E. (1978). *Science and technology of rubber*, Academic Press.
- Gordana Marković, Blaga Radovanović, Milena Marinović-Cincović & Jaroslava Budinski-Simendić (2009) The Effect of Accelerators on Curing Characteristics and Properties of Natural Rubber/Chlorosulphonated Polyethylene Rubber Blend, *Materials and Manufacturing Processes*, 24:10-11, 1224-1228, DOI: 10.1080/10426910902967087
- Gungor A., (2022). Components used in the vulcanization of rubber. *Engineering Applications*, 1(2), 132-136
- Heideman, G., Datta, R. N., Noordermeer, J. W. M., & van Baarle, B. (2004). Activators in accelerated sulfur vulcanization. *Rubber Chemistry and Technology*, 77(3), 512-541. <https://doi.org/10.5254/1.3547834>
- Hoffman W. (1989). *Rubber Technology Handbook*. Hanser Publishing Munich.
- <http://www.kaucuk.org/kaucuk.asp>
- Ismail H., Ahmad Z. & Mohd Ishak Z.A. (2003). Effects of cetyltrimethylammonium maleate on curing characteristics and mechanical properties of polychloroprene rubber, *Polymer Testing*, 22, 179-183. [https://doi.org/10.1016/S0142-9418\(02\)00067-3](https://doi.org/10.1016/S0142-9418(02)00067-3)
- Joseph R., George K.E. & Francis D. J. (1988). Studies on the cure characteristics and vulcanizate properties of 50/50 NR/SBR blend , *J. Appl. Polym. Sci.* 35, 1003-1017. <https://doi.org/10.1002/app.1988.070350415>
- Koc A., Tuken T., (2019). The Effects Of Accelerators Used In Sulfur Vulcanization Systems Epdm Rubber Compound On Rheological Properties, *Ç.Ü Fen ve Mühendislik Bilimleri Dergisi*, Cilt: 38-3.
- Kresja M.R. & Koenig J.L. (1993). *Rubber Chem. Technol*, 66, 376.
- Loyd D.G. (1976). Rubber chemicals as a means of making polymers work, *Plastics and Rubber*, 1, 4.
- Mostoni, S., Milana, P., Di Credico, B., D'Arienzo, M., & Scotti, R. (2019). Zinc-based curing activators: new trends for reducing zinc content in rubber vulcanization process. *Catalysts*, 9(8), 664.
- Nabil H, Ismail H, Azura AR (2014). Optimization of Accelerators on Curing Characteristics, Tensile, and Dynamic Mechanical Properties of (Natural Rubber)/(Recycled Ethylene-PropyleneDiene-Monomer) Blends. *J Vinyl Addit Techn.* Volume21, Issue2, Pages 79-88 <https://doi.org/10.1002/vnl.21358>
- Pongdhorn S.Q, Chakrit S., Uthai T. & Phuchong T., (2001). Influence of accelerator type on properties of NR/EPDM blends, *Polymer Testing* 20, 925-936. <https://doi.org/10.1016/j.polymertesting.2007.07.004>
- Puspitasari S., Cifriadi A. (2019). Design of Elastomeric Bridge Bearing Pad Compound Formula Based on Hydrogenated Natural Rubber, *J. Eng . Technol. Sci.*, Vo l. 51, No . 5, 649-661
- Rader, C.P. (1985). *Vulcanization, Intermediate Correspondence Course*, Rubber Division, ACS, Akron, OH.
- Sabu T., Hanna J.M., Joy J., Chan C.H., Pothen L. A., (2014), *Natural Rubber Materials Volume 2: Composites and Nanocomposites*, The Royal Society of Chemistry, Cambridge UK.

- Sadequil A.M., Ishiaku U.S., Ismail H. & Poh B.T., (1998). The effect of accelerator/sulfur ratio on the scorch time of epoxidized natural rubber, *Eur. Polym. J.* 34 (1), 51-57. [https://doi.org/10.1016/S0014-3057\(97\)00067-0](https://doi.org/10.1016/S0014-3057(97)00067-0)
- Samarasinghe IHK, Walpalage S., Edirisinghe D.G., SM Egodage S.M., (2020). Study on sulfur vulcanized natural rubber formulated with nitrosamine safe diisopropylxanthogen polysulfide/tertiarybutyl benzothiazole sulphenamide binary accelerator system, *Progress in Rubber Plastics and Recycling Technology*, 1-13, DOI: 10.1177/1477760620977499.
- Savran H. O., *Elastomer Teknolojisi* 2, (2001). Kauçuk Derneđi Yayınları. İstanbul.
- Setyadawi M. N., Mayasari H.E., (2020). Curing Characteristic of Various Accelerators on Natural Rubber/Chloroprene Rubber Blends, *Jurnal Dinamika Penelitian Industri* Vol. 31 No. 2.
- Singh G., Mahajan A., Kumar M., (2015). A Review Paper on Vulcanization of Rubber and It's properties *GLOBAL JOURNAL OF ENGINEERING SCIENCE AND RESEARCHES*, August, 2(8).
- Sirishina C., Limcharoen S.B. & Thunyarittikorn J. (2001) Relationships among blending conditions, size of dispersed phase, and oil resistance in natural rubber and nitrile rubber blends, *J. Appl. Polym. Sci.* 82, 1232. <https://doi.org/10.1002/app.1957>
- Sirqueira A. S. & Soares B. G. (2003) The effect of mercapto- and thioacetate-modified EPDM on the curing parameters and mechanical properties of natural rubber/EPDM blends, *European Polymer Journal*, 39, 2283-2290. [https://doi.org/10.1016/S0014-3057\(03\)00163-0](https://doi.org/10.1016/S0014-3057(03)00163-0)
- Susamma A.P., Mini V.T.E. & Kuriakose A.P., (2001). Studies on Novel Accelerator System in the Sulphur Vulcanization of Natural Rubber, *Journal of Applied Polymer Science*, 79, 1-8. [https://doi.org/10.1002/1097-4628\(20010103\)79:1](https://doi.org/10.1002/1097-4628(20010103)79:1)
- Teker M., Öztürk E. (2008). Master Thesis, Farklı kauçuk karışımlarının vulkanizasyonuna hızlandırıcıların etkisi, University of Sakarya, Sakarya.
- Walker B. M. & Rader C.P. (1988). Rader, Handbook of Thermoplastic Elastomers. Van Nostrand Reinhold, Newyork.



Optimization and PID Control of pH and Temperature in an Electrocoagulation Process

Şule Camcıoğlu¹ , Baran Özyurt^{1*} 

¹Ankara University, Faculty of Engineering, Department of Chemical Engineering, Ankara, Turkey

Abstract: In this work, effects of temperature and pH in batch treatment of pulp and paper mill wastewater using electrocoagulation has been investigated. Conductivity, temperature, and pH are selected as controlled variables; supporting electrolyte, cooling water, acid and base flow rates are selected as manipulated variables, respectively. Real time experimental multi input-multi output (MIMO) control of conductivity, temperature, and pH under constant current conditions are achieved using MIMO Proportional Integral Derivative (PID) control algorithms coded in MATLAB™. A central composite design (CCD) has been applied to the system under controlled conditions and optimum pH and temperature values are obtained using response surface methodology (RSM). Both controlled and uncontrolled experiments are performed using optimum values and results are compared in terms of removal efficiencies of pollutants. Results show that 34.47% chemical oxygen demand (COD), 98.06% total suspended solids (TSS), 99.80% turbidity, 99.93% color, and 13.40% SO₄²⁻ removal is achieved in 45 minutes of process operation under controlled conditions and COD, TSS, turbidity, color and SO₄²⁻ removal are increased by 10.92, 2.97, 4.06, 2.89, 3.17 respectively in comparison with uncontrolled operation. The highest removal percentages are obtained under controlled operating conditions as 98.5% and 98.3% for turbidity and color, respectively, for 10 minutes operation. It is concluded that optimum process operating conditions for removal of turbidity and color of pulp and paper mill wastewater is obtained under constant 6.45 pH, 23.24 °C temperature, 1.78 mS/cm conductivity, and power consumption is reduced by 25.3% under controlled conditions.

Keywords: Pulp and paper mill wastewater, pH, temperature, electrocoagulation, PID control, RSM.

Submitted: August 31, 2023. **Accepted:** January 13, 2024.

Cite this: Camcıoğlu, S., & Özyurt, B. (2024). Optimization and PID Control of pH and Temperature in an Electrocoagulation Process. *Journal of the Turkish Chemical Society, Section B: Chemical Engineering*, 7(1), 13–24. <https://doi.org/10.58692/jotcsb.1353347>

***Corresponding author. E-mail:** bozyurt@ankara.edu.tr

1. INTRODUCTION

The pulp and paper industry has high pollutant discharges to the environment and they consume considerable amount of wood, water and energy. In terms of freshwater withdrawal, the pulp and paper making industry is one of the most water demanding industry and position third in the world, after the primary metals and the chemical industries (Sridhar et al., 2011). The industrial wastewaters cause several problems such as color, slime growth, thermal impacts, and scum formation in the environment. They also affect the ecosystem, enlarge the quantity of toxic substances in the water, and pollute scenic beauty (Pokhrel & Viraraghavan, 2004). Water turbidity generated by the presence of suspended solids and colloidal particles cannot be treated by conventional methods such as filtration and sedimentation (Özyurt et al.,

2021; Terrazas et al., 2010). Electrocoagulation process has been confirmed to be effective in destabilizing colloidal particles and color removal (Linares-Hernández et al., 2009). As an electrolytic technology, it consists of anodic dissolution of a metal electrode within the effluent to be treated, with the simultaneous formation of hydroxyl ions and hydrogen gas. Compared with traditional methods, electrocoagulation, in theory, has the advantage of removing the smallest colloidal particles; the smallest charged particles have better probability of being coagulated because of the electric field that sets them in motion (Mollah et al., 2004; Terrazas et al., 2010). Treatment of pulp and paper mill wastewater by electrocoagulation is highly complex process and is greatly influenced by many factors such as electrode configuration and material, current density, electrolysis time, electrical conductivity, pH and temperature (El-Ashtoukhy et al., 2009; Kalyani et al., 2009; Katal

& Pahlavanzadeh, 2011; Khansorthong & Hunsom, 2009; Soloman et al., 2009; Uğurlu et al., 2008; Zaid & Bellakhal, 2009). Among these operational parameters, temperature and pH were found to be more significant than the others. Temperature affects the pollutant removal in many ways such as rate of reactions, solubility of metal hydroxides, liquid conductivity and kinetics of gas bubbles or small colloidal particles (Attour et al., 2014). It is reported that the increase in the temperature of the solution cause increasing the solubility of aluminum (Vepsäläinen et al., 2009). For that reason the precipitation of the aluminum is increased at lower temperatures, which results in a better removal (Katal & Pahlavanzadeh, 2011). In electrocoagulation process direct electrical current applied between metal electrodes immersed in wastewater causes the dissolution of aluminum or iron electrodes into wastewater. Chemical dissolution of metal electrodes is strongly influenced by the pH of the solution. The dissolved metal ions, at an appropriate pH, can form wide ranges of coagulated species and metal hydroxides that destabilize and aggregate suspended particles or precipitate and adsorb dissolved contaminants (Cañizares et al., 2005; Merzouk et al., 2009). At low pH (2-3) cationic monomeric species Al^{3+} and $Al(OH)^{2+}$ dominate. When pH is between 4 and 9, the Al^{3+} and OH^- ions generated by the electrodes react to form various monomeric species such as $Al(OH)^{2+}$, $Al(OH)_2^{2+}$, and polymeric species such as $Al_6(OH)_{15}^{3+}$, $Al_7(OH)_{17}^{4+}$, $Al_{13}(OH)_{34}^{5+}$ that finally transform into insoluble amorphous $Al(OH)_{3(s)}$ through complex precipitation kinetics (Bayramoglu

et al., 2004). When pH is higher than 10, the monomeric $Al(OH)_4^-$ anion concentration increases (Alinsafi et al., 2005). It is reported that there is a 1-2 units of increase in pH during electrocoagulation (Camcıoğlu et al., 2017b). Accordingly formations of ionic compounds that have high solubility in water cause a decrease in removal efficiencies. As a result control of pH and temperature in their optimum values come up as a necessity.

In this study the effects of temperature and pH in treatment of pulp and paper mill wastewater with electrocoagulation has been investigated. A CCD has been applied to the system and optimum pH and temperature values are obtained using RSM. In order to determine the effect of constant electrical conductivity, pH and temperature on removal efficiencies during electrocoagulation, experiments were performed under controlled and uncontrolled conditions of operating parameters using optimum values and the results were compared in terms of COD, TSS, turbidity, color, SO_4^{2-} and Cl^- removal efficiencies.

2. EXPERIMENTAL SECTION

2.1. Experimental Procedure

Experiments were carried out in batch process using a 2000 mL electrocoagulation reactor made of flex-glass. In each run, 1000 mL of sedimented pulp and paper mill wastewater was fed into the reactor. Characteristics of sedimented pulp and paper mill wastewater are given below in Table 1.

Table 1: Characteristics of pulp and paper mill wastewater.

Chemical Oxygen Demand (mg/L)	Total Suspended Solids (mg/L)	Turbidity (NTU)	Color (CU)	Conductivity (mS/cm)	pH	SO_4^{2-} (mg/L)	Cl^- (mg/L)
681.72	118	173	923	1.80	7.5	281	105.42

Six electrodes made of aluminum with dimensions of 60 mm x 60 mm x 2 mm were positioned in mono-polar parallel arrangement with a gap separation between them of 10 mm. In order to conduct the experiments under constant current conditions, the electrodes were connected to a DC power supply (MAY 11-PS Constant Current Power Supply) operating in the range of 0-2 A. 0.04 M NaCl, 0.1 M HCl and 0.1 M NaOH solutions were added to the wastewater with peristaltic pumps (Longer Pump LEAD-2). A stirrer (MTOPS MS-3020) was used to maintain uniform concentration and temperature dispersion in the reactor. During experiments a heating/cooling water circulator (Hoefer RCB 20-PLUS) was used at 12 °C in order to keep temperature constant at a desired value and avoid possible temperature increase.

A pH meter, conductivity meter and a thermocouple were used for on-line measurements of pH, conductivity and temperature during wastewater treatment. These probes were placed into a

separate chamber inside the reactor to avoid the measurements to be influenced from charge distribution occurring in the reactor. Sample circulation between the chamber and reactor was carried out using a peristaltic pump (Aspen Standard Pump).

On-line signals of pH, conductivity and temperature from measurement devices are sampled and transferred towards controller using data acquisition device (MAY 11-ESA Electrophoresis Control Unit) and calculated signals from controller is transferred to related manipulated variable via the data acquisition device and input variables are adjusted. In electrical control studies 0.04 M NaCl solution flow rate is the input variable and is adjusted by the electrical conductivity controller signals transferred to the peristaltic pump. pH control studies are carried out using 0.1 M HCl solution and 0.1 M NaOH solution flow rate as the input variables and their values are adjusted by the pH controller signals transferred to the peristaltic pumps. Temperature

control studies were performed using on/off position of cooling water valve as the manipulated variable and its position is regulated by the temperature controller. Experimental setup is given in Figure 1.

Experiments were carried out in 1 A constant current and 45 minutes electrocoagulation time conditions.

A multi-purpose real-time MATLAB/Simulink model and a PID controller program were designed for performing electrocoagulation studies, monitoring input and output variables, carrying out dynamic analyses and control experiments in electrochemical reactor. Real-time MATLAB/Simulink model is given in Figure 2.

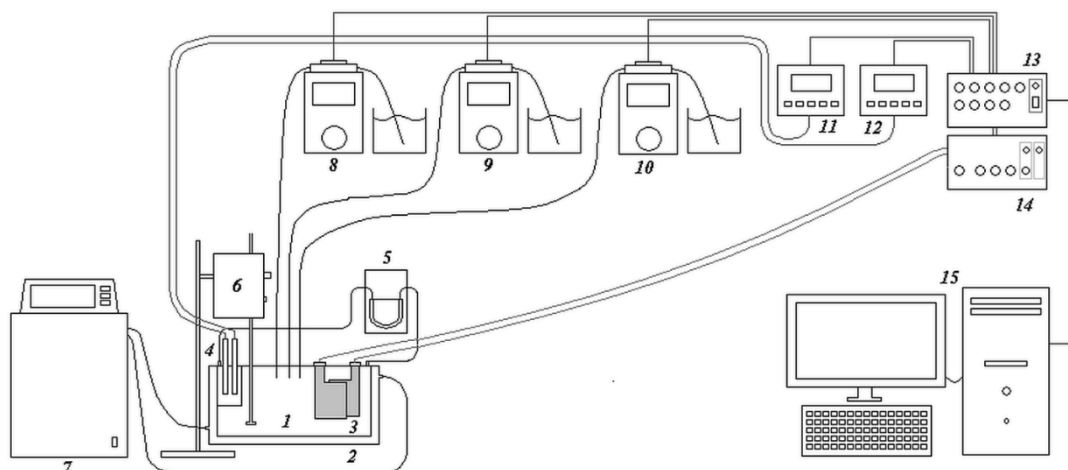


Figure 1: Experimental set-up (1: electrocoagulation reactor, 2: electrocoagulation reactor heating/cooling jacket, 3: electrodes, 4: pH meter, conductivity meter, thermocouple, 5: sample circulation pump, 6: mechanical stirrer, 7: heating/cooling water circulator, 8: acid pump, 9: base pump, 10: supporting electrolyte pump, 11: pH and temperature display, 12: conductivity display, 13: control unit, 14: power supply, 15: computer).

2.2. Analytical Procedure

50 mL of the samples were taken after treatment processes and kept 3 h at 20 °C for sedimentation. Supernatants were collected for analyses. COD analyses were performed according to SM 5220 D (Eaton et al., 2005). 2.5 mL of samples were treated with 1.5 mL of high range digestion solution and 3.5 mL of sulfuric acid reagent in 16 x 100 mm culture tubes. Treated samples were digested at 150 °C for 2 h using a thermoreactor (Velp ECO-16). After digestion process, tubes were cooled down to room temperature and absorbance of the samples were read at 600 nm using a spectrophotometer (PG Instruments T60V). The COD of the samples were

calculated with a calibration curve prepared using potassium hydrogen phthalate standard. Color analyses were performed in accordance with SM 2120 C (Eaton et al., 2005). Sample absorbances were read at 456 nm using the spectrophotometer. Color values were calculated by a calibration curve prepared previously using 500 CU Pt-Co stock solution. Sample turbidities were measured using a turbidity meter (Aqualytic AL250T-IR). TSS analyses were performed accordingly according to SM 2540 D (Eaton et al., 2005). SO_4^{2-} and Cl^- analyses are performed in accordance with SM 4500 SO_4^{2-} E and SM 4500 Cl^- B (Eaton et al., 2005) respectively.

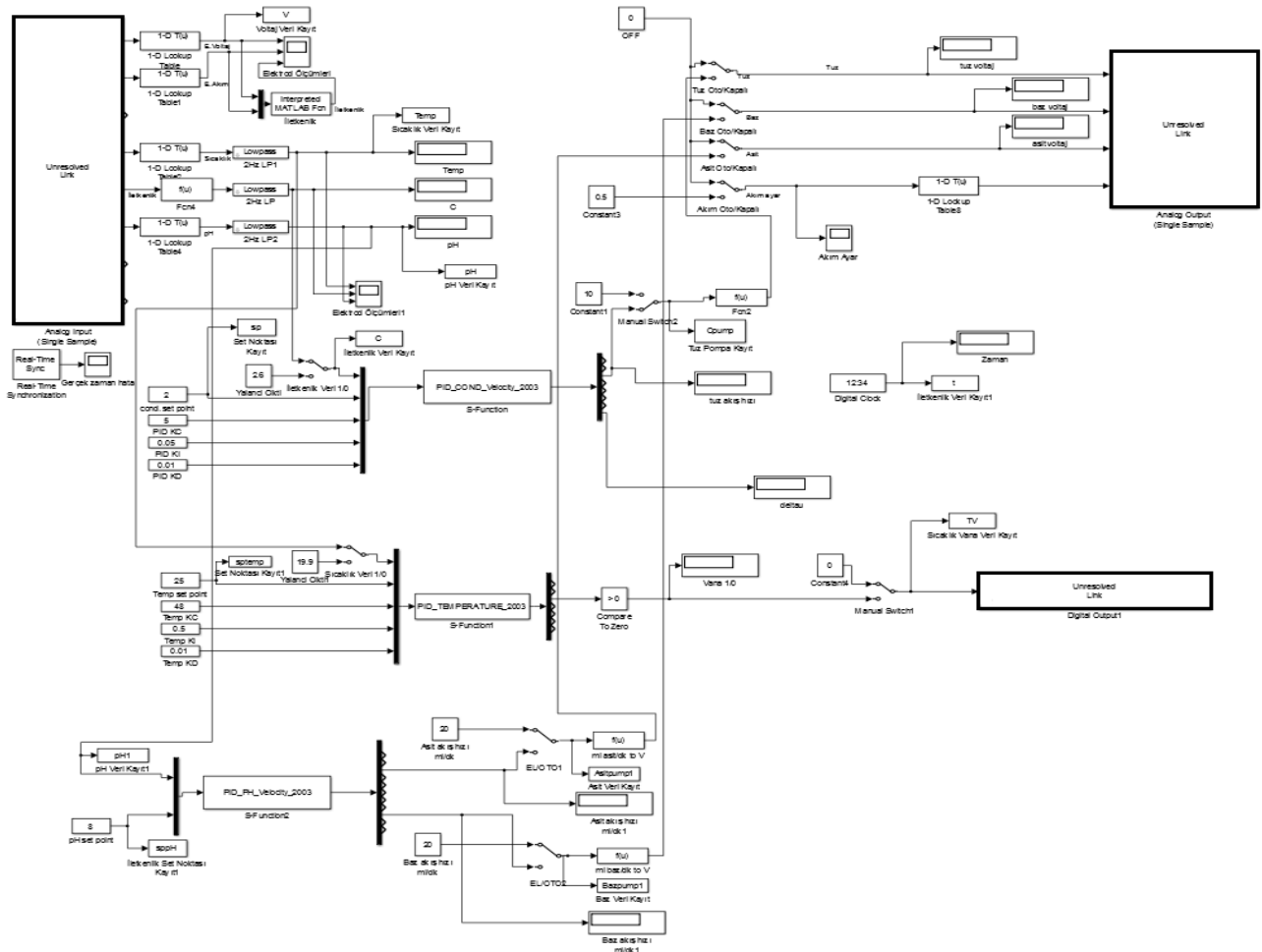


Figure 2: Real-time MATLAB/Simulink model.

3. RESULTS AND DISCUSSION

3.1. Determination of Optimum pH and Temperature

RSM was used to determine the model that gives the relation between dependent variables turbidity removal (y_1) and color removal (y_2) and the independent variables pH (x_1) and temperature (x_2). Experiments were also carried out to find the

optimum values of operating parameters for maximum turbidity and color removal. CCD with 2 factors was applied using Minitab 17 statistical software. A total number of 14 experiments consisting of 4 factorial points, 4 axial points and 6 replicates in the center points were employed in this work. Experimental design matrix in terms of uncoded factors and measured responses are given in Table 2.

Table 2: Design of experiments and results for electrocoagulation treatment.

Run	x_1 pH	x_2 Temperature (°C)	y_1 Turbidity removal (%)	y_2 Color removal (%)
1	7.50	22.50	100.00	100.00
2	12.45	22.50	14.20	10.33
3	7.50	22.50	99.99	100.00
4	7.50	22.50	98.12	98.33
5	7.50	11.89	98.68	99.23
6	2.55	22.50	74.68	76.43
7	7.50	33.11	99.34	99.17
8	11.00	15.00	50.18	43.44
9	7.50	22.50	100.00	99.52
10	4.00	30.00	74.43	75.29
11	4.00	15.00	69.43	70.29
12	11.00	30.00	54.70	37.80
13	7.50	22.50	98.83	98.53
14	7.50	22.50	98.59	98.94

Color and turbidity removal results of the samples taken at 15 minute time intervals for each run are presented in Figure 3. A nonlinear regression method was used to fit the experimental data to second-order polynomial equation to identify model terms for turbidity and color removal using Minitab 17 statistical software. Mathematical form of second-order polynomial equation considering all the linear, square and linear by linear interaction terms is given in Equation (1).

$$Y = \beta_0 + \sum_{i=1}^k \beta_i x_i + \sum_{i=1}^k \beta_{ii} x_i^2 + \sum_{i=1}^{k-1} \sum_{j=2}^k \beta_{ij} x_i x_j + \varepsilon$$

(Eq. 1)

Where Y is the predicted response, x_i and x_j are the input variables (i and j range from 1 to k), β_0 is the model intercept coefficient, β_i , β_{ii} , β_{ij} are the regression coefficients for the linear, quadratic and interaction terms respectively, k is the number of independent variables and ε is the interaction effect (Korkmaz et al., 2017).

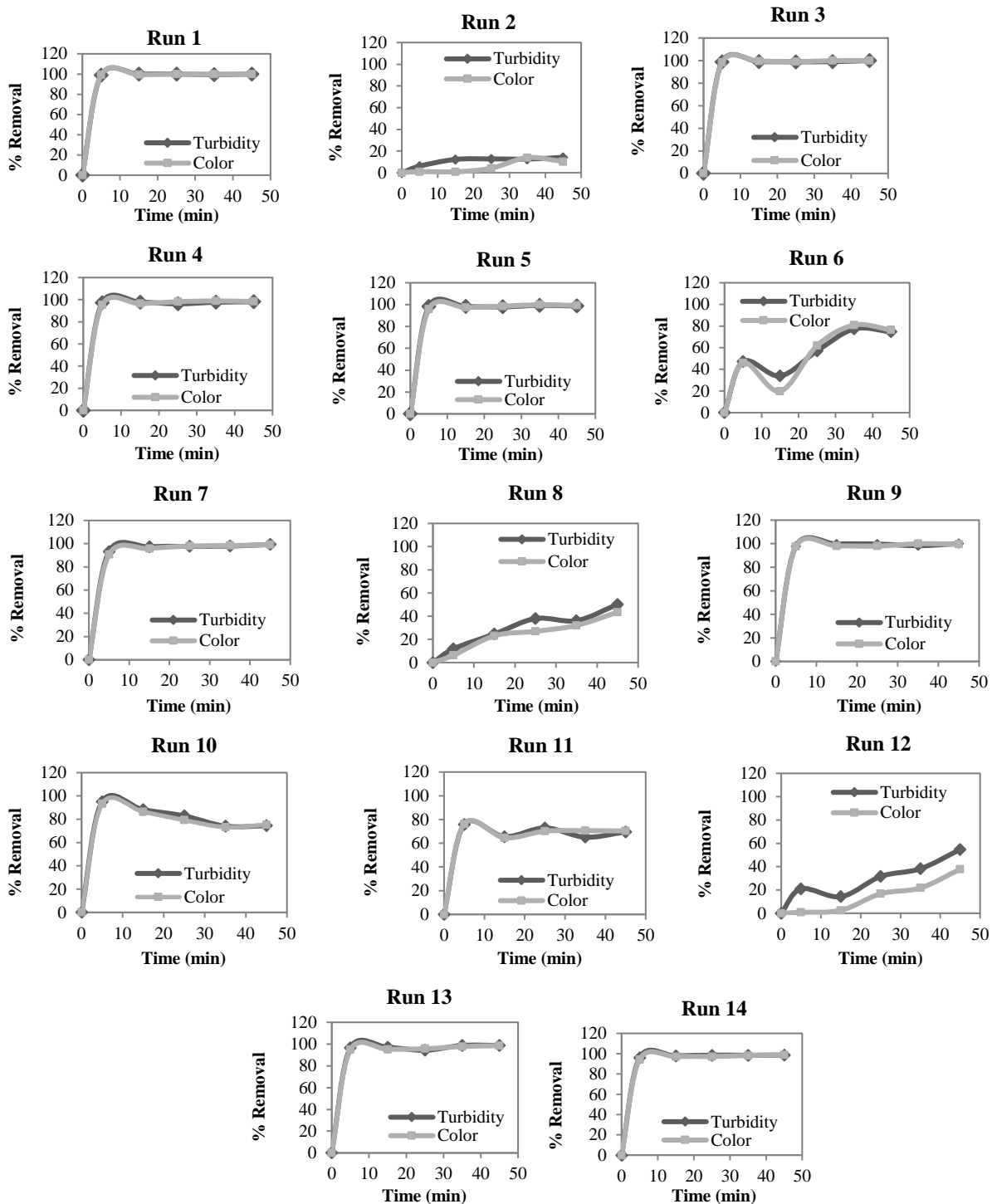


Figure 3: Variation of turbidity and color removal with time for run 1-14.

The second-order polynomial equations for turbidity removal and color removal in terms of uncoded factors are given in Equation 2 (2) and Equation (3), respectively.

$$y_1 = -30.7 + 32.03x_1 + 2.18x_2 - 2.432x_1^2 - 0.0446x_2^2 \quad (2)$$

$$y_2 = -36.1 + 33.02x_1 + 2.91x_2 - 2.577x_1^2 - 0.065x_2^2 \quad (3)$$

The statistical significance of the models were justified through analysis of variance (ANOVA) with F-test at 95% confidence level. Results of regression analysis are shown in Tables 3 and 4 for turbidity and color removal, respectively.

Table 3: Regression analysis results for turbidity removal in terms of coded factors.

Predictor	Coef	SE Coef	T	P	
Constant	99.25	2.73	36.35	0.000	
x ₁	-15.56	2.36	-6.58	0.000	
x ₂	1.31	2.36	0.55	0.596	
x ₁ ²	-29.79	2.46	-12.11	0.000	
x ₂ ²	-2.51	2.46	-1.02	0.338	
Analysis of Variance					
Source	DF	SS	MS	F	P
Model	5	8614.04	1722.81	38.51	0.000
Blocks	1	107.88	107.88	2.41	0.159
Linear	2	1951.13	975.56	21.81	0.001
pH	1	1937.48	1937.48	43.31	0.000
Temp	1	13.65	13.65	0.31	0.596
Square	2	6555.03	3277.52	73.27	0.000
pH*pH	1	6554.68	6554.68	146.54	0.000
Temp*Temp	1	46.50	46.50	1.04	0.338
Error	8	357.85	44.73		
Lack-of-fit	4	354.37	88.59	101.77	0.000
Pure Error	4	3.48	0.87		
Total	13	8971.89			

P and t tests were used to determine the compatibility of second order polynomial equations with the experimental results. Terms including temperature were found to be the least effective in the model. ANOVA results presented in Table 4 and 5 indicate higher F-values for regression of turbidity and color models than F distribution table value of 3.69. The large F-value shows that most of the variation in the output can be explained by the developed regression model (Camcıoğlu et al., 2017a). The associated P-value is also used as an indicator for whether F is large enough to indicate

statistical significance. The P-values of reduced quadratic models are <0.001 which clearly confirm good fit of experimental data. The values of R², adjusted R², predicted R² and lack of fit of models are obtained to investigate the accuracy of the suggested polynomials. In order to emphasize the relationships between factors and responses and also to determine the optimum conditions, Equations (2) and (3) are expressed as response surfaces. The value of R² gives the correlation of total variation in the effluent removal efficiencies predicted by developed models.

Table 4: Regression analysis results for color removal in terms of coded factors.

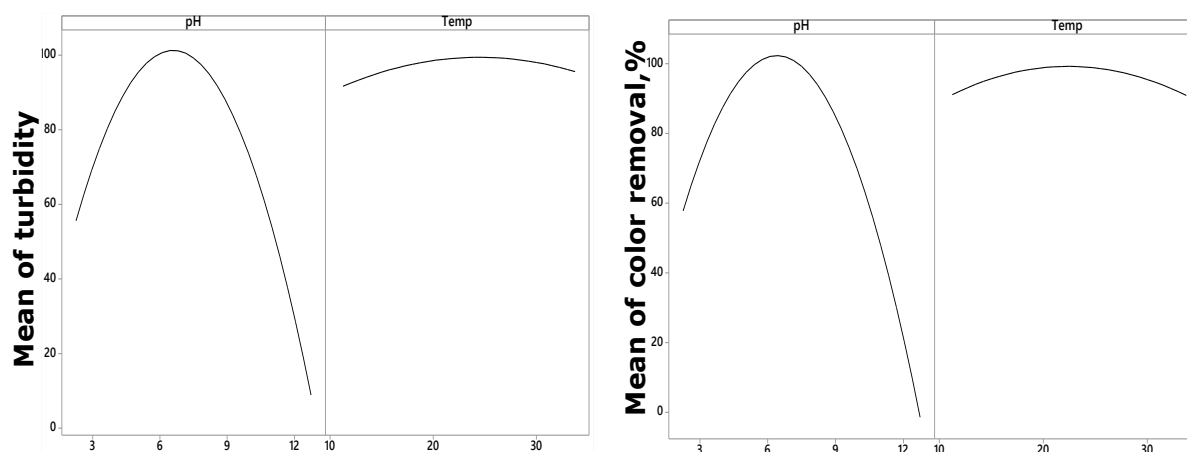
Predictor	Coef	SE Coef	T	P
Constant	99.22	2.53	39.16	0.000
x ₁	-19.73	2.19	-8.99	0.000
x ₂	-0.09	2.19	-0.04	0.968
x ₁ ²	-31.57	2.28	-13.82	0.000
x ₂ ²	-3.66	2.28	-1.60	0.148

Analysis of Variance					
Source	DF	SS	MS	F	P
Model	5	10737.1	2147.42	55.76	0.000
Blocks	1	254.3	254.29	6.60	0.033
Linear	2	3113.5	1556.74	40.42	0.000
pH	1	3113.4	3113.41	80.84	0.000
Temp	1	0.1	0.07	0.00	0.968
Square	2	7369.3	3684.67	95.67	0.000
pH*pH	1	7358.1	7358.12	191.05	0.000
Temp*Temp	1	98.8	98.77	2.56	0.148
Error	8	308.1	38.51		
Lack-of-fit	4	305.8	76.44	129.81	0.000
Pure Error	4	2.4	0.59		
Total	13	11045.2			

For turbidity and color removal, R² values are calculated as 0.9601 and 0.9721 for reduced quadratic models which ensure an acceptable fit to experimental data (Rai et al., 2016). Adjusted R² values for the models are 0.9352 and 0.9547 which also high enough to support acceptable correlation between experimental and predicted value. The predicted R² values for the present models are 0.7459, 0.8613 and suggest how good the models predict the effluent removal. The adjusted R² and predicted R² should be within 20% of each other to be in reasonable agreement (Bozoglu et al., 2015).

These values offer 74.59 and 86.13% of variability in predicting new observation in comparison to approximately 96.01 and 97.21% variability in the original data.

Main effect plot was drawn in order to determine the effects of factors causing significant changes in turbidity and color removal efficiencies when factor levels were changed. Mean turbidity and color removal efficiencies were drawn against pH and temperature with levels and shown in Figure 4.

**Figure 4:** Main effects plot for turbidity and color removal.

As can be seen from the figure, pH and temperature have various effects since the variation in factor levels from low to middle range caused increase in turbidity and color removal efficiencies while a significant decrease is observed in the middle – high factor levels range.

Single interaction plots for two factors were plotted. An interaction plot is a plot of means for each level of a factor with the level of a second factor held

constant. Interaction is present when the response at a factor level depends upon the levels of other factors. Parallel lines in an interaction plot indicate no interaction (Bozoglu et al., 2015). The greater the departure of the lines from the parallel state, the higher the degree of interaction. However, the interaction plot does not indicate statistical significance. The interaction of pH and temperature was examined in Figure 5.

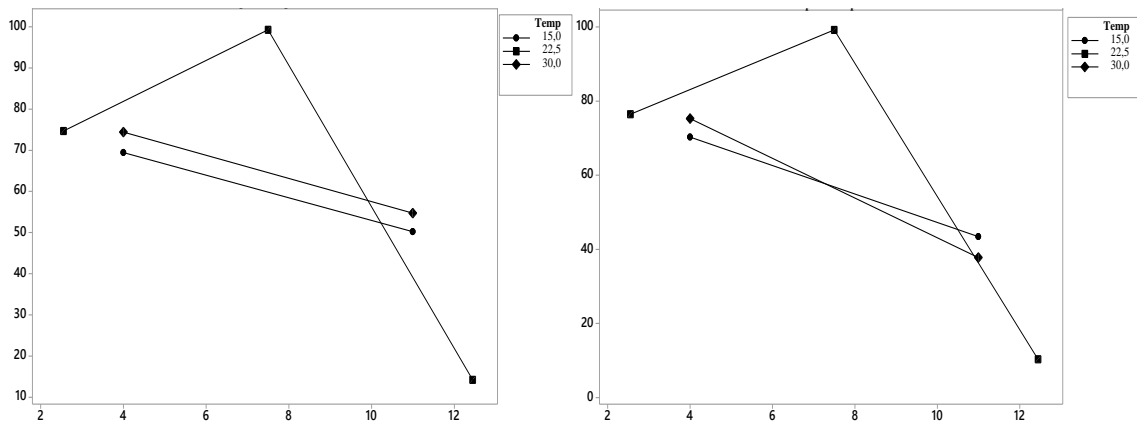


Figure 5: Interaction plot for turbidity and color removal.

The two-factor interaction of pH and temperature was observed for both turbidity and color removal cases. If low and high levels of factors were compared only, the results would be elusory. Although midpoint experiments indicated the interaction between factors, it could not be detected by experiments at low and high range for turbidity removal. The highest mean removal was reached at 22.5 °C and pH 7.5 while the lowest mean removal was obtained at 22.5 °C and pH 12.45.

The optimal condition giving maximum turbidity and color removal was determined by evaluating obtained models in Minitab 17 and reported as 6.45 for pH and 23.25 °C for temperature. The surface response and contour plots of the reduced quadratic models for turbidity and color removal varying with temperature and pH are shown in Figure 6 and 7, respectively.

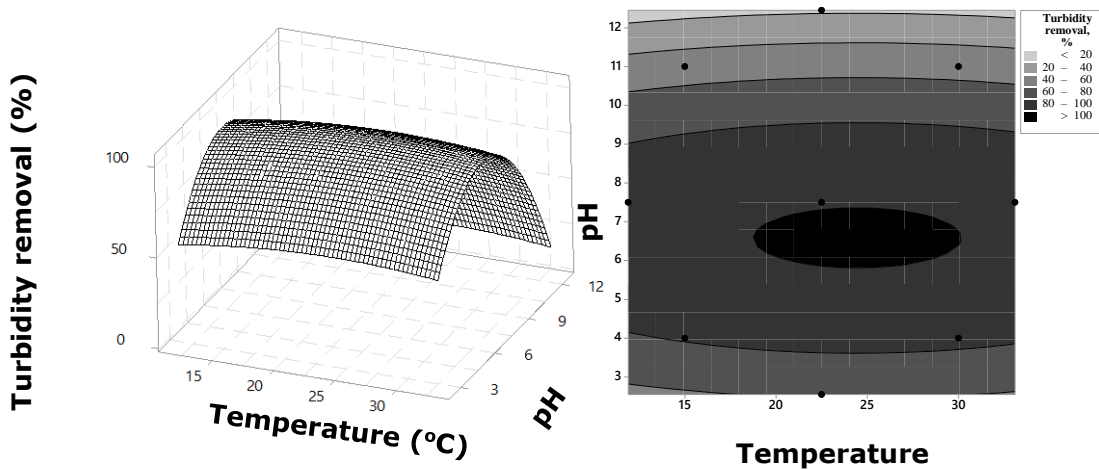


Figure 6: Surface and contour plot for turbidity removal as a function of temperature and pH.

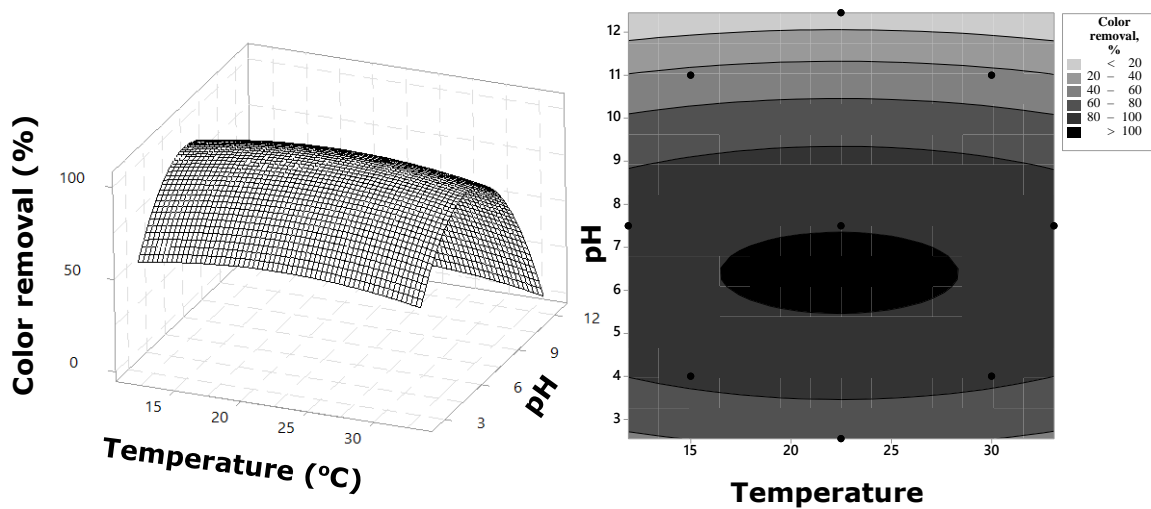


Figure 7: Surface and contour plot for color removal as a function of temperature and pH.

3.2. Effect of Process Controlled Operation on Treatment Performance

The conventional PID feedback control is the most frequently applied feedback control strategy because of its robustness, ease of operation and the lack of specified process knowledge required for the controller designs (Camcioğlu et al., 2017). Real time experimental MIMO control of conductivity, temperature and pH under constant current conditions are performed using Simulink™ based digital MIMO PID controllers designed in our previous study (Camcioğlu et al., 2017b).

Algorithms are adapted to a designed real time Simulink™ model which has the ability to transfer real time data of input measurement signals from conductivity, temperature and pH sensors to designed controller and calculated controller output signals to supporting electrolyte, acid and base pumps and cooling water valve simultaneously. Conductivity, temperature and pH are selected as controlled variables; cooling water, supporting electrolyte, acid and base flow-rate are selected as manipulated variables. PID parameters of controllers are given in Table 5.

Table 5: PID parameters of controllers.

Controller	Parameters		
	Proportional	Integral	Derivative
Conductivity	5	0.05	0.01
Temperature	48	0.5	0.01
pH (Acid)	1000	0.05	0.01
pH (Base)	1	0.06	0.04

In order to determine the effect of constant conductivity, pH and temperature on removal efficiencies and power consumption during electrocoagulation treatment, experiments were performed under controlled and uncontrolled conditions using optimum pH and temperature values and the results were compared in terms of turbidity and color removal. Initial values of pH and

temperature were set to 6.45 and 23.24 °C respectively at natural wastewater conductivity in both uncontrolled and controlled electrocoagulation studies. Variation of pH and temperature under uncontrolled and controlled conditions are presented in Figures 8 and 9, respectively.

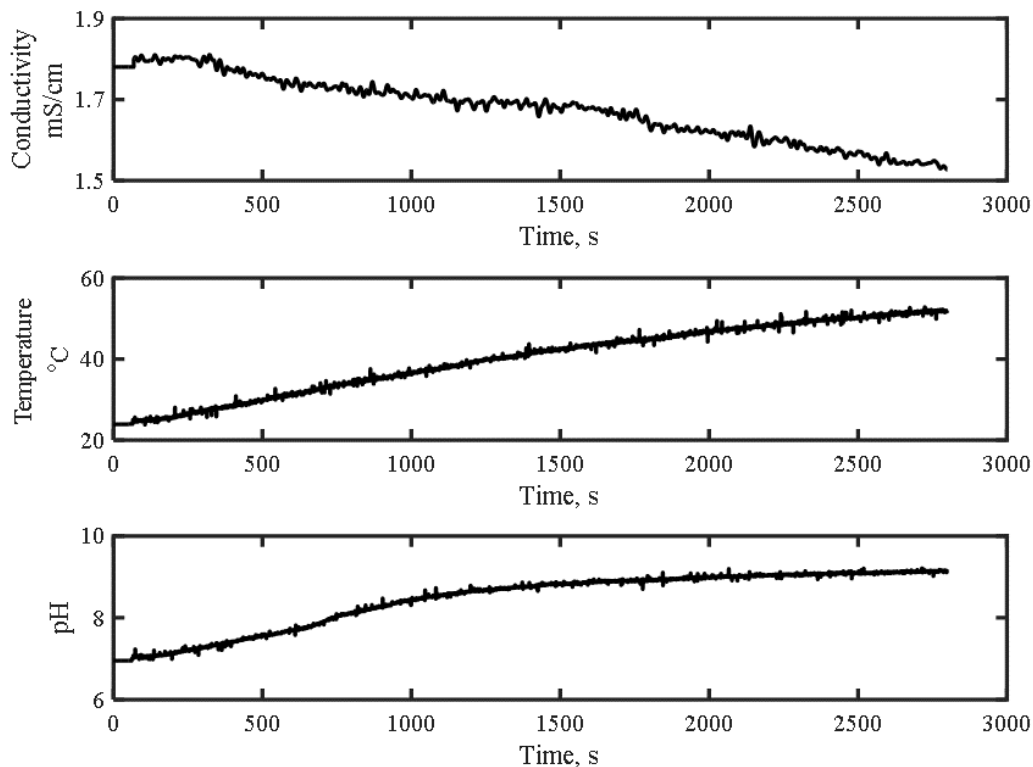


Figure 8: Variation of operating conditions with time for uncontrolled case.

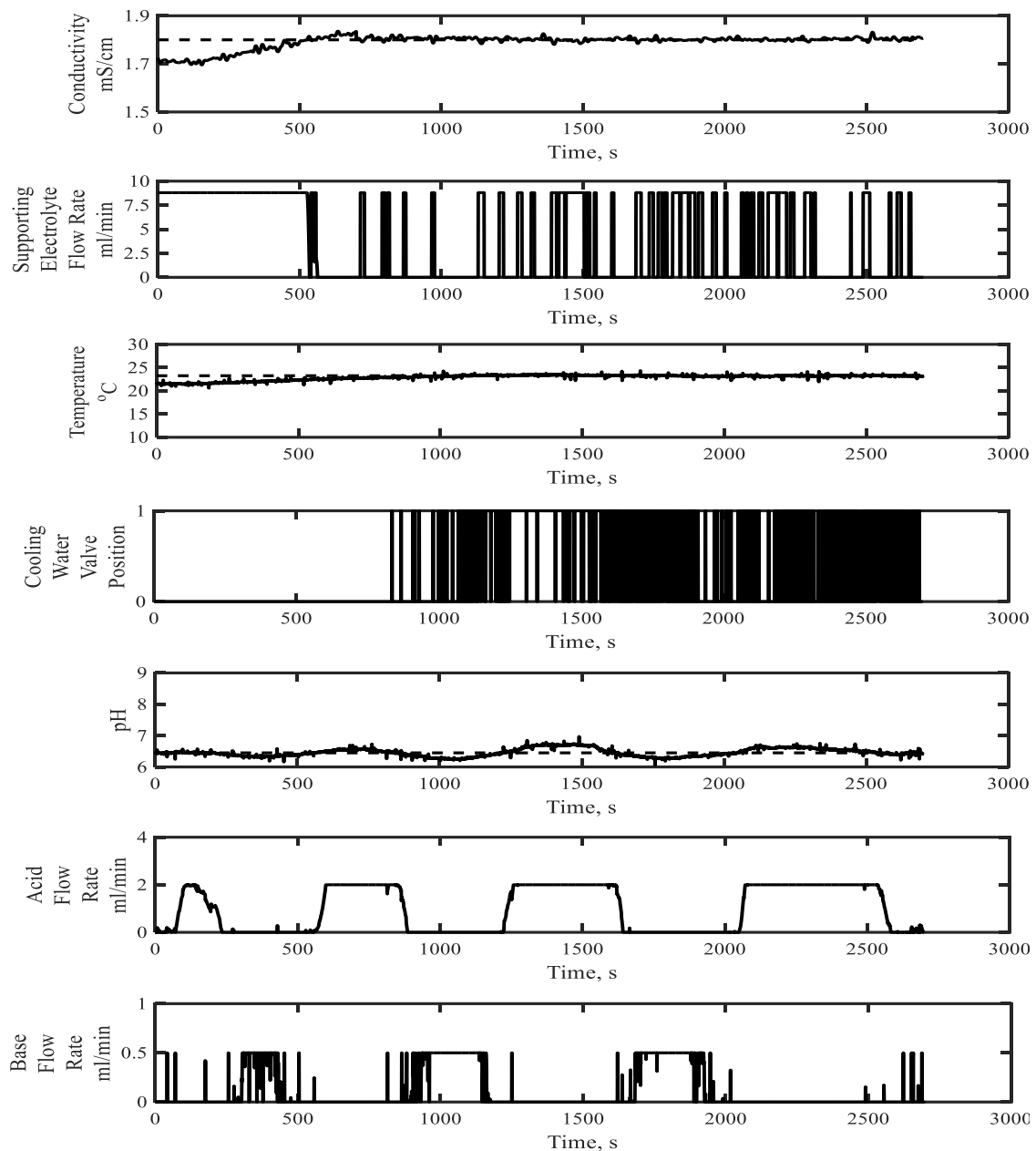


Figure 9: Variation of operating conditions with time for controlled case.

Removal of turbidity and color by time were investigated for uncontrolled and controlled cases at the optimum operating conditions and the results were given in Figure 10.

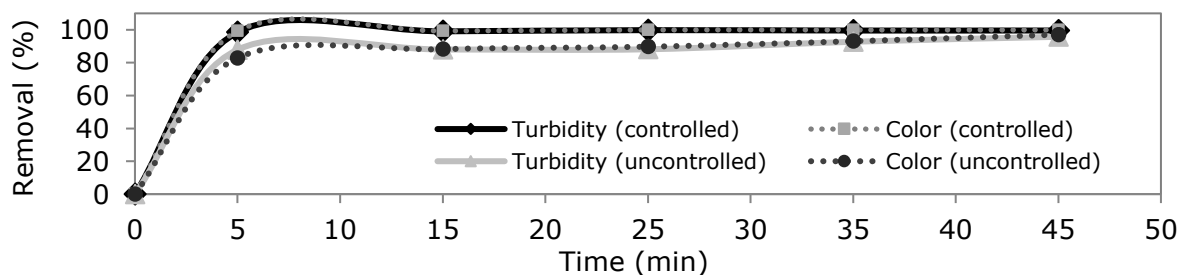


Figure 10: Removal of turbidity and color for uncontrolled and controlled cases.

Results show that 10 minute batch process operation is sufficient for complete removal of turbidity and color under controlled conditions.

Power consumption of uncontrolled and controlled cases are calculated as 26.14 kWh/m³ and 19.53 kWh/m³ respectively. Results show that

conductivity control leads to a 25.3% power consumption reduction. Treatment results of pulp and paper mill wastewater by means of

electrocoagulation for 45 minutes under optimum operating conditions are given below in Table 6.

Table 6: Effluent removal results.

Treatment	COD removal (%)	TSS removal (%)	Turbidity removal (%)	Color removal (%)	SO ₄ ²⁻ removal (%)	Cl ⁻ removal (%)
Controlled	34.47	98.06	99.80	99.93	13.40	-
Uncontrolled	23.55	95.09	95.74	97.04	10.23	9.84

Experimental results, throughout the present study, have shown that MIMO control of conductivity, pH and temperature increased removal efficiency of COD, TSS, turbidity, color and SO₄²⁻ compared with uncontrolled condition. Besides less power consumption is required for a higher effluent removal. Cl⁻ removal cannot be achieved under controlled conditions due to supporting electrolyte addition for conductivity control.

4. CONCLUSION

Removal of COD, TSS, turbidity, color and SO₄²⁻ from pulp and paper mill wastewater is successfully achieved in a batch electrocoagulation reactor. Operating parameters of process were selected as conductivity, pH and temperature respectively. It is observed that under uncontrolled conditions conductivity was dropped 0.28 mS/cm, pH was increased 2.10 units and temperature was increased 28.39 °C during 45 min process. Results show that 87.9% turbidity and 82.9% color removal is achieved in 10 minutes of process operation under uncontrolled conditions. Removal percentages are increased as 7.8 and 14.1% for turbidity and color, respectively. Power consumption is reduced by 25.3% under controlled conditions. The highest removal percentages are obtained under controlled operating conditions as 98.5% and 98.3% for turbidity and color, respectively, for 5 minutes of operation. Under controlled optimum operating conditions, COD, TSS, turbidity, color and SO₄²⁻ removal is increased by 10.92, 2.97, 4.06, 2.89, 3.17, respectively for 45 minutes of process operation in comparison with uncontrolled operation. It is concluded that optimum process operation for removal of turbidity and color of pulp and paper mill wastewater is obtained under constant 6.45 pH, 23.24 °C temperature, 1.78 mS/cm conductivity and 5 minutes time.

5. CONFLICT OF INTEREST

The authors have no conflict of interest.

6. REFERENCES

Alinsafi, A., Khemis, M., Pons, M. N., Leclerc, J. P., Yaacoubi, A., Benhammou, A., & Nejmeddine, A. (2005). Electro-coagulation of reactive textile dyes and textile wastewater. *Chemical Engineering and Processing: Process Intensification*, 44(4), 461–470.

<https://doi.org/https://doi.org/10.1016/j.cep.2004.06.010>

Attour, A., Touati, M., Tlili, M., Ben Amor, M., Lopicque, F., & Leclerc, J.-P. (2014). Influence of operating parameters on phosphate removal from water by electrocoagulation using aluminum electrodes. *Separation and Purification Technology*, 123, 124–129. <https://doi.org/https://doi.org/10.1016/j.seppur.2013.12.030>

Bayramoglu, M., Kobya, M., Can, O. T., & Sozbir, M. (2004). Operating cost analysis of electrocoagulation of textile dye wastewater. *Separation and Purification Technology*, 37(2), 117–125. <https://doi.org/https://doi.org/10.1016/j.seppur.2003.09.002>

Bozoglu, M. D., Ertunc, S., Akay, B., Bursali, N., Vural, N., Hapoglu, H., & Demirci, Y. (2015). The effect of temperature, pH and SO₂ on ethanol concentration and sugar consumption rate (SCR) in apple wine process. *Journal of the Chemical Society of Pakistan*, 37(3), 431–439.

Camcıoğlu, S., Ozyurt, B., & Hapoglu, H. (2017a). Effect of process control on optimization of pulp and paper mill wastewater treatment by electrocoagulation. *Process Safety and Environmental Protection*, 111, 300–319. <https://doi.org/https://doi.org/10.1016/j.psep.2017.07.014>

Camcıoğlu, S., Ozyurt, B., & Hapoglu, H. (2017b). MIMO control application for pulp and paper mill wastewater treatment by electrocoagulation. *Desalination and Water Treatment*, 93, 200–213.

Camcıoğlu, Ş., Özyurt, B., Doğan, İ. C., & Hapoğlu, H. (2017). Application of response surface methodology as a new PID tuning method in an electrocoagulation process control case. *Water Science and Technology*, 76(12), 3410–3427. <https://doi.org/10.2166/wst.2017.506>

Cañizares, P., Carmona, M., Lobato, J., Martínez, F., & Rodrigo, M. A. (2005). Electro-dissolution of Aluminum Electrodes in Electrocoagulation Processes. *Industrial & Engineering Chemistry Research*, 44(12), 4178–4185. <https://doi.org/10.1021/ie048858a>

Eaton, A. D., Clesceri, L. S., Franson, M. A. H., Association, A. P. H., Rice, E. W., Greenberg, A. E., Association, A. W. W., & Federation, W. E. (2005). *Standard Methods for the Examination of Water & Wastewater* (Issue 21).

- c.). American Public Health Association. <https://books.google.com.tr/books?id=buTn1r mfSI4C>
- El-Ashtoukhy, E.-S. Z., Amin, N. K., & Abdelwahab, O. (2009). Treatment of paper mill effluents in a batch-stirred electrochemical tank reactor. *Chemical Engineering Journal*, 146(2), 205–210. <https://doi.org/https://doi.org/10.1016/j.cej.2008.05.037>
- Kalyani, K. S. P., Balasubramanian, N., & Srinivasakannan, C. (2009). Decolorization and COD reduction of paper industrial effluent using electro-coagulation. *Chemical Engineering Journal*, 151(1), 97–104. <https://doi.org/https://doi.org/10.1016/j.cej.2009.01.050>
- Katal, R., & Pahlavanzadeh, H. (2011). Influence of different combinations of aluminum and iron electrode on electrocoagulation efficiency: Application to the treatment of paper mill wastewater. *Desalination*, 265(1), 199–205. <https://doi.org/https://doi.org/10.1016/j.desal.2010.07.052>
- Khansorhthong, S., & Hunsom, M. (2009). Remediation of wastewater from pulp and paper mill industry by the electrochemical technique. *Chemical Engineering Journal*, 151(1), 228–234. <https://doi.org/https://doi.org/10.1016/j.cej.2009.02.038>
- Korkmaz, M., Özmetin, C., Cirtlik, A., & Siğirci, Ş. I. (2017). Full factorial design of experiments for boron removal from solutions by PuroLite S 108 resin converted to hydroxyl form. *Particulate Science and Technology*, 35(6), 742–748. <https://doi.org/10.1080/02726351.2016.1196277>
- Linares-Hernández, I., Barrera-Díaz, C., Roa-Morales, G., Bilyeu, B., & Ureña-Núñez, F. (2009). Influence of the anodic material on electrocoagulation performance. *Chemical Engineering Journal*, 148(1), 97–105. <https://doi.org/https://doi.org/10.1016/j.cej.2008.08.007>
- Merzouk, B., Gourich, B., Sekki, A., Madani, K., Vial, C., & Barkaoui, M. (2009). Studies on the decolorization of textile dye wastewater by continuous electrocoagulation process. *Chemical Engineering Journal*, 149(1), 207–214. <https://doi.org/https://doi.org/10.1016/j.cej.2008.10.018>
- Mollah, M. Y. A., Morkovsky, P., Gomes, J. A. G., Kesmez, M., Parga, J., & Cocke, D. L. (2004). Fundamentals, present and future perspectives of electrocoagulation. *Journal of Hazardous Materials*, 114(1), 199–210. <https://doi.org/https://doi.org/10.1016/j.jhazmat.2004.08.009>
- Özyurt, B., Camcıoğlu, Ş., Karatokuş, T., & Yüksek, C. (2021). Ayçiçek yağı endüstrisi atık sularının koagülasyon-flokülasyon ve elektro-Fenton yöntemleriyle arıtılması . *Gazi Üniversitesi Mühendislik Mimarlık Fakültesi Dergisi* , 36(1), 275–290. <https://doi.org/10.17341/gazimmfd.553847>
- Pokhrel, D., & Viraraghavan, T. (2004). Treatment of pulp and paper mill wastewater—a review. *Science of The Total Environment*, 333(1), 37–58. <https://doi.org/https://doi.org/10.1016/j.scitotenv.2004.05.017>
- Rai, A., Mohanty, B., & Bhargava, R. (2016). Supercritical extraction of sunflower oil: A central composite design for extraction variables. *Food Chemistry*, 192, 647–659. <https://doi.org/https://doi.org/10.1016/j.foodchem.2015.07.070>
- Soloman, P. A., Ahmed Basha, C., Velan, M., Balasubramanian, N., & Marimuthu, P. (2009). Augmentation of biodegradability of pulp and paper industry wastewater by electrochemical pre-treatment and optimization by RSM. *Separation and Purification Technology*, 69(1), 109–117. <https://doi.org/https://doi.org/10.1016/j.seppur.2009.07.002>
- Sridhar, R., Sivakumar, V., Prince Immanuel, V., & Prakash Maran, J. (2011). Treatment of pulp and paper industry bleaching effluent by electrocoagulant process. *Journal of Hazardous Materials*, 186(2), 1495–1502. <https://doi.org/https://doi.org/10.1016/j.jhazmat.2010.12.028>
- Terrazas, E., Vázquez, A., Briones, R., Lázaro, I., & Rodríguez, I. (2010). EC treatment for reuse of tissue paper wastewater: Aspects that affect energy consumption. *Journal of Hazardous Materials*, 181(1), 809–816. <https://doi.org/https://doi.org/10.1016/j.jhazmat.2010.05.086>
- Uğurlu, M., Gürses, A., Doğar, Ç., & Yalçın, M. (2008). The removal of lignin and phenol from paper mill effluents by electrocoagulation. *Journal of Environmental Management*, 87(3), 420–428. <https://doi.org/https://doi.org/10.1016/j.jenvman.2007.01.007>
- Vepsäläinen, M., Ghiasvand, M., Selin, J., Pienimaa, J., Repo, E., Pulliainen, M., & Sillanpää, M. (2009). Investigations of the effects of temperature and initial sample pH on natural organic matter (NOM) removal with electrocoagulation using response surface method (RSM). *Separation and Purification Technology*, 69(3), 255–261. <https://doi.org/https://doi.org/10.1016/j.seppur.2009.08.001>
- Zaied, M., & Bellakhal, N. (2009). Electrocoagulation treatment of black liquor from paper industry. *Journal of Hazardous Materials*, 163(2), 995–1000. <https://doi.org/https://doi.org/10.1016/j.jhazmat.2008.07.115>



Optimizing Activated Carbon Production from Waste Cashew Nut Shell with Zinc Chloride: A Box-Behnken Design and Group Method of Data Handling (GMDH) Application

Karinate Valentine Okiy  and Joseph Tagbo Nwabanne 

Department of Chemical Engineering, Nnamdi Azikiwe University, P.M.B. 5025, Awka 420218, Nigeria

Abstract: In this study, Response surface methodology (RSM) and innovative Group Method of Data Handling (GMDH) approaches are applied to investigate the optimal process conditions of Zinc Chloride activated cashew nut production process. The effects of activation conditions (i.e. activation temperature, activation time, and impregnation ratio) on the achievable BET surface areas were studied with the aid of Box Behnken Design (BBD) and GMDH. Comparative analysis of RSM and GMDH-type neural models were further researched. During the process, the polynomial model equations developed were modified and fine-tuned to predict the highest BET surface area(s) using regression analysis and GMDH multi-layered iterative algorithm (MIA). Analysis of Variance (ANOVA) revealed that the significant factor(s) were impregnation ratio, impregnation ratio product and the 2-way interactions (activation temperature and impregnation ratio) for $ZnCl_2$ activated cashew nut shell. The best activation conditions for producing highest BET surface area of $504 \text{ m}^2 \cdot \text{g}^{-1}$ was activation temperature (873K), activation time (60 min), and impregnation ratio (1.50). The proposed GMDH-type BET model was ascertained to be the best model with average correlation coefficient (R) and root mean square error (RMSE) of 0.925 & 32.0 respectively. Sensitivity analysis conducted for GMDH-type neural network also revealed that the activation temperature and activation time with sensitivity values of 90.6% and 74.1% respectively were the most influential parameters in the basic ($ZnCl_2$) activation process. The results of this study show that RSM and GMDH-type neural network could be applied as effective analytical tools for optimizing the ZCNS manufacturing process.

Keywords: Cheaper Agro-wastes derived Porous Carbons, Box Behnken Design (BBD), Basic activation, Group Method of Data Handling (GMDH), Process Optimization.

Submitted: January 17, 2024. **Accepted:** February 20, 2024.

Cite this: Okiy, K. V., & Nwabanne, J. T. (2024). Optimizing Activated Carbon Production from Waste Cashew Nut Shell with Zinc Chloride: A Box-Behnken Design and Group Method of Data Handling (GMDH) Application. *Journal of the Turkish Chemical Society, Section B: Chemical Engineering*, 7(1), 25-42. <https://doi.org/10.58692/jotcsb.1421501>.

Corresponding author. Email: karinateokiy@gmail.com

1. INTRODUCTION

Industrial activities are major sources of effluent discharges into rivers, water bodies, streams and reservoirs causing serious environmental pollution (Howard et al., 1986). Many industries including iron and steel, battery manufacturing, mining, petrochemicals/refineries, tanneries, microelectronics, non-ferrous metals, textile & leather, breweries, metal processing, pharmaceutical, photographic, glassware, electroplating, paints, pulp & paper, pesticides manufacturing, dyeing, breweries, ceramics and chemical manufacturing generate significant volumes

of effluent containing pollutants like biodegradable organics, cyanide, dissolved inorganic solids, suspended solids, phenols, chlorinated organic compounds, refractory organics, mineral oil, polychlorinated biphenyls (PCBs), dyes and heavy metals (Shi, 2009; Dawei, 2012; Ajemba, 2014; Kulkarni et al., 2014). Heavy metals are metals with molecular weight in the range of 63.5 to 200.6 and density greater than $5 \text{ g} \cdot \text{cm}^{-3}$ (Wang, 2011). Toxic heavy metals such as lead, chromium, mercury, arsenic & nickel are considered as major pollutants of great environmental significance (Wang., 2011; Singh et al., 2011). Wastewaters contaminated with toxic

heavy metals ions require exhaustive treatment in order to remove the toxic metal ions down to minimal (trace) outlet concentrations before discharge into receiving water bodies for economic and environmental reasons (Okiy, 2006).

Numerous conventional separation techniques exist for the removal of toxic heavy metals from aqueous solutions/wastewater and these include adsorption, chemical precipitation, freeze crystallization, gamma irradiation, foam flotation, ultrafiltration, ozonation, vapour recovery, reverse osmosis, membrane separation, solvent extraction, ion exchange, electrodialysis, coagulation, evaporation, nanofiltration, flocculation, electrochemical process and biosorption methods. Whilst some of these treatment technologies have proven successful for treatment of heavy metal-contaminated wastewater, other methods have a number of downsides limiting their use such as fouling, high capital, and operational costs as well as the generation of bulk quantities of chemical sludge requiring proper disposal into the environment (Demirbas, 2008; Nwabanne and Okoye., 2013; Srivastava et al., 2015; Malik et al., 2016). Amid these, adsorption method is considered as an excellent option and is widely utilized for the treatment of effluent emanating from chemical industries (Akinbiyi, 2000; Xu et al., 2013). Activated carbon (AC) is the adsorbent of choice worldwide due to its high efficiency and versatility for adsorbing different pollutants present in municipal and industrial wastewater (Gupta et al., 2009; Malik et al., 2016). However, the price of commercial activated carbons normally produced from naturally occurring raw materials (precursors) such as lignite, peat, wood, petroleum residues, anthracite, and coal varies from 0.8 to 10 Euros per kilogram depending on process type and the activation method utilized (Stavropoulos and Zabaniotou, 2009). In order to reduce these exorbitant material costs, there is need for concerted efforts to be directed towards production of low-cost activated carbons from agro-wastes such as cashew nut shells.

Cashew nut (*Anacardium occidentale* L.) is predominantly found in Asian, African, and Latin American countries such as Vietnam, India, Tanzania, Cote d'Ivoire, Nigeria, and Brazil. Nigeria is the world's second largest producer of cashew nuts with an annual production of 836,500 Metric Tonnes (Adeigbe et al., 2015). Cashew nuts are commonly eaten as a snack and utilized in preparation of meals, desserts, and confectioneries. Nigeria is also a major exporter of cashew nuts, with a significant portion of the produce being sold to international markets. In fact, Nigeria is one of the largest producers and exporters of cashew nuts in the world. The export market provides income opportunities for farmers and contributes about 24 billion naira to Nigeria's foreign exchange earnings. Nigeria is a major consumer of cashew nuts, both for domestic consumption and as an ingredient in various dishes (Adeigbe et al., 2015). Cashew nut shells are a byproduct of cashew processing and are typically

discarded. The waste shells are hard and contain a toxic resin called cardol, which can cause skin irritation and other health issues if handled improperly. Improper disposal of the shells can lead to land and water pollution, as well as create breeding grounds for insects and pests. Thus, the proper disposal and management of cashew nut shells is a major area of environmental concern in Nigeria that requires attention and sustainable solutions. Efforts have been made to find alternative uses for cashew nut shells to mitigate these disposal challenges. For example, some companies and entrepreneurs have explored the utilization of cashew nut shells for energy generation, production of industrial materials like adhesives, or conversion into animal feed and organic fertilizers (Ademola et al., 2021). However, the scale of these initiatives is relatively limited. Hitherto, few studies utilizing cashew nut shells for the production of activated carbons have been conducted in the past. In this study, cashew nut shell was chosen for the production of activated carbon.

According to Dyk (2000), the predominant characteristic for classifying activated carbons industrially is BET surface area. The manufacture of activated carbon is also affected by several process variables (factors) including activation temperature, impregnation ratio, and activation time (Essa et al., 2013). The classical approach in dealing with many factors is the one factor at a time (OFAT) experimentation. This method entails studying the effect of each parameter on the response of interest by successively varying each parameter within a specified ambit, while maintaining the other parameters constant at the zero (median) level (Elibol, 2002). OFAT is painstakingly tedious and does not provide any information on the interaction (combined) effects of the process variables (factors) (Onu et al., 2021). Instead of considering each factor in isolation, it is also possible to combine the series of independent studies into one study.

Response Surface Methodology (RSM) is a useful tool for studying the interaction of two or more parameters (factors) on a response. RSM is a compendium of mathematical and statistical techniques used for process development, upgrading and optimization. RSM approach encompasses four major stages (i) the design and conduction of experiments for measuring the studied response (ii) response surface modeling via non-linear model fitting over experimental data (iii) visualization of the interactive and main effects of the independent variables on the studied response via two-dimensional (2-D) & three-dimensional (3-D) plots and, (iii) process optimization (Essa et al., 2013). A major benefit of RSM is the minimal material costs and less number of experimental runs needed to assess main and interaction effects of several parameters for the system under consideration (Montgomery, 2017). Interaction effects of the various factors could be attained using RSM with design of experiments (DoE). Box Behnken design (BBD) is one of the more

established statistical experimental designs for RSM modeling (Okewale et al., 2015). BBD comprises of the factorial 2^k level designs and incomplete block designs with a number of core factorial runs in the design (n_F), number of experimental runs at the high and/or low values of the factors in the design (n_i) and the number of runs at the centre (median) point values of the factors in the design (n_0) (Okewale et al., 2015). The BBD design is more suitable when the number of factor(s) is between 3 and 4, as minimal numbers of experimental runs are needed for optimal response (Ozer et al., 2009; Montgomery., 2017). However, statistical methods such as RSM are difficult to implement for modeling complex and non-linear real-world problems. Unlike statistical approaches, other data driven models such as artificial neural network (ANN) feature exceptional ability to handle complex (noisy) non-linear problems (Palani et al., 2009; Nkurlu et al., 2020). Nonetheless, there are a number of drawbacks associated with standard ANN including poor model generalization ability (over-fitting), slow

trial & error process associated with user-led specification of network architecture (i.e hidden layers, hidden nodes), and network algorithm convergence at local minimum. The group method of data handling (GMDH) is an improvement over the ANN technique, due to the GMDH algorithm's self-organizing (intelligent) control in identification of optimal network structure and process modeling (Li et al., 2017).

Group method of data handling (GMDH) is a grouping of mathematical modeling and non-linear regression algorithms (polynomial neural networks) for computational-based modeling of experimental dataset(s) characterised by fully automatic determination of model structure, hidden nodes, number of hidden levels and parametric model optimization (Madala & Ivakhneko., 1994; Voss., 2002). Complex non-linear systems with several inputs and one output are modeled with GMDH employing the Kolmogorov-Gabor polynomial given as:

$$Y = a_0 + \sum_{i=1}^m a_i x_i + \sum_{i=1}^m \sum_{j=1}^m a_{ij} x_i x_j + \sum_{i=1}^m \sum_{j=1}^m \sum_{k=1}^n a_{ijk} x_i x_j x_k \dots \quad (\text{Eq. 1})$$

The GMDH method was initially proposed in 1968 at the Institute of Cybernetics, Kyiv by an Ukrainian scientist and mathematician named Professor Alexey Grigorevich Ivakhnenko (Stanley, 1981). The GMDH analysis protocol is based on an amalgamation of (1) the neural approach which uses the threshold logic (selection criterion) & network connectionism and, (2) the black box concept, which examines non-linear input-output variable relationships (Nkurlu et al., 2020). The external criterion describes the requirements for selection of a model of optimal complexity that unravels the hidden law from input data. Whilst, network connectionism defines the mapping accuracy of the region between input and output dataset(s) (Li et al., 2017).

GMDH-type neural network is computationally faster, circumvents over-fitting problems, objectively selects the optimum model, and eliminates the slow trial & error process of optimal algorithmic (i.e number of hidden layers, neurons) parameters selection required for efficient neural network design (Nkurlu et al., 2020). The novel GMDH has never been utilized before for process modeling and optimization in the field of engineering. This marks the first time that GMDH is applied to model a chemical process such as the production of activated carbon from cashew nutshell (CNS) with chemical (ZnCl_2) activation. In this present study, RSM (BBD) and GMDH methods will be employed to analyze the alkaline CNS activation process and predict the maximum BET surface area of ZnCl_2 -activated cashew nut shell (CNS).

Therefore, this work aims to (i) explore the preparation of activated carbons from cashew nut shells with

chemical (ZnCl_2) activation (ii) select optimal CNS activated carbons with maximum BET surface areas based on RSM (BBD) design (iii) utilise GMDH technique for optimizing the manufacture of ZnCl_2 activated CNS under different preparation conditions of impregnation ration, time, and activation temperature (iv) comparatively analyse the ZnCl_2 -activated CNS production process using BBD with the RSM approach and a GMDH-type neural network to determine the optimal conditions for maximum achievable BET surface area.

2. MATERIALS AND METHODS

2.1. Adsorbent preparation

The raw cashew nut shells were procured from Eke-Awka market at Awka South Local Government Area, Anambra State in the Eastern part of Nigeria (N: $6^\circ 13' 8''$; E: $7^\circ 5' 13''$). Chemical activation of cashew nut shell sample with Zinc chloride as reagent was performed according to the chemical activation procedure reported by Senthil Kumar et al., (2012) and Subramaniam & Ponnusamy, (2015) with minor modification. The experimental procedure for producing the cashew nut shell activated carbon is presented in Figure 1. 300 grams of raw cashew nut shell sample was pre-treated by washing with 5000 grams of distilled water and 3945 grams of ethanol to remove dirt and other soluble impurities. Consequently, the washed avocado pear seed samples were dried in a Mermert oven at a temperature of 343K for 24 hours. Then, the dried cashew nut shell samples were ground into fine particles utilising a Jencod grinding machine and sieved using a standard Taylor Sieve with mesh size of 300 μm . 300g of cashew

nut shell sample was then carbonised at a 973K for 2 hours. Thereafter, 300 grams of carbonised cashew nut shell was mixed with 88.4 grams of 30% Zinc chloride reagent according to the impregnation ratios (0.5:1, 1:1, and 1.5:1) for 2 hours and heated in a Mermert oven at 378K for 24 hours. The dried zinc chloride impregnated cashew nut shell was then thermally activated in a Muffle furnace at different activation temperatures (873K, 1023K, and 1173K) and times (60, 90, and 120 minutes). The $ZnCl_2$ treated sample was cooled, and repeatedly washed to remove disorganised carbon, products of decomposition and

traces of sulphuric acid. The activated carbon samples were also transferred to a beaker containing 250 ml solution of HCl (about 0.1mol) for 1 hour and washed again with distilled water till a pH of 6-7 is achieved. The washed activated carbon sample was filtered with Whatman No.1 filter paper and dried in a Mermert oven at 353K for 3 hours before usage. Textural characterisation of the Zinc chloride activated carbon sample was performed using a Quantachrome NOVA4200e BET Analyzer (Anton-Paar GmbH, Austria) to determine the texture feature (BET surface area).

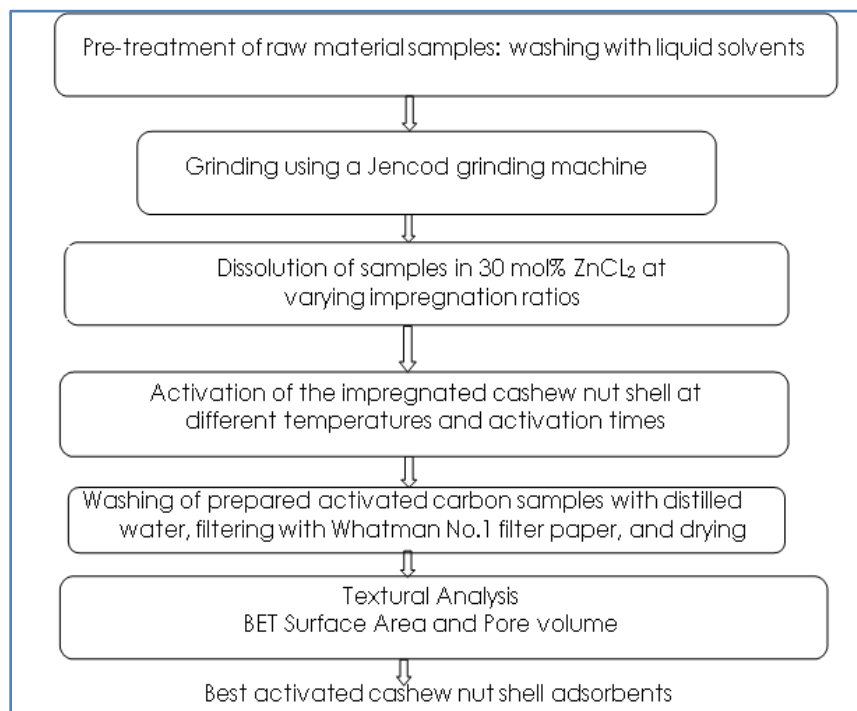


Figure 1: Flowchart showing the method of producing Zinc chloride activated carbon from cashew nut shells.

2.1.1. Design of experiment (DOE) for APS activation by BBD modeling

Box Behnken (BBD) design was chosen for accurate and precise experimental data collection in only few runs to allow for adequate approximation of the response surface (Montgomery, 2017). The effect of independent variables (activation temperature, time and impregnation ratio) on the production of optimal APS activated carbons with highest achievable BET surface area (response variable) was studied using Box

Behnken (BBD) design. The lower and upper limits of the independent variables (factors) chosen for the BBD are shown in Table 1.

The ranges of the independent variables were chosen based on literature reviews and prior studies (Essa et al., 2013; Buasri et al., 2023). For the BBD design, the total number of experimental runs was determined using Eq. (2) (Melvin et al., 2015).

$$N = K^2 + K + C_p \quad \text{Eq. (2)}$$

Where, N is the number of experimental runs, C_p is the replicate number of the central point, and K is the factor number.

Table 1: Independent Variables and Their Levels for Box Behnken Experimental design.

Independent Variable(s)	Range and Level		
	-1	0	+1
Activation temperature (A, °C)	600	750	900
Activation time (B, min)	60	90	120
Impregnation ratio (C, Activating agent: raw material)	0.5	1.0	1.5

To improve the effectiveness of the BBD design and minimize random errors, the factorial and incomplete block (IBD) experimental runs were performed in triplets. In accordant with 9 centre (null) points, leading to a total of 54 experimental runs were utilized in the response surface methodology (RSM) analysis. The factorial points gave an equal variation of the high and low values, while the null points gave the estimate of experimental error and ensured reproducibility of the data (Essa et al., 2013; Onu et al., 2021).

The Behnken design is an orthogonal design, with values of the experimental factors (points) at the midpoint of the edges and the centre of a multi-dimensional sphere defining the experimental domain (Douglas and Montgomery, 2007; Anderson and Whitcomb., 2016). Box Behnken Experimental Design being of spherical (cubic) design, the independent

variables were coded for low, medium, and high settings, as -1, 0, and +1 and uniformly spaced (Douglas and Montgomery, 2007) as afore-presented in Table 1.

The statistical analysis was carried out using Design Expert Software version 13 (STAT-EASE Inc, USA) to predict the response of the studied system. The fifteen (15) experimental runs were performed in a random manner to avert systematic error. The analysis of variance (ANOVA) test was also used to evaluate the accuracy of the approximating polynomial model.

Furthermore, the reduction empirical model utilized in describing the $ZnCl_2$ -CNS fabrication process is represented by the ensuing second-order approximating polynomial model equation, in terms of coded factors:

$$Y = b_0 + \sum_{i=1}^n b_i X_i + \sum_{i=1}^n b_{ii} X_i^2 + \sum_{i=1}^{n-1} \sum_{j=2}^n b_{ij} X_i X_j + E \quad \text{Eq. (3)}$$

Where, Y is the predicted dependent variable, b_0 is the constant coefficient (intercept), n is the number of patterns, b_i , b_{ij} , and b_{ii} are the regression coefficients of the linear, and interaction terms respectively, X_i , and X_j are the independent factors studied, i, and j are index numbers, and E is the error term.

2.1.2. GMDH-type neural network

GMDH-type neural network is structured as a feed-forward neural network with multi-layered bi-nodal polynomial activation function(s) as depicted in Figure 2. GMDH can be presumed to be a polynomial network (Ayoub et al., 2019). The GMDH analysis protocol harnesses the benefits of multi-layered neural networks and self-organizing ability to select the intrinsic affiliation(s) between input data and network (output) predictions.

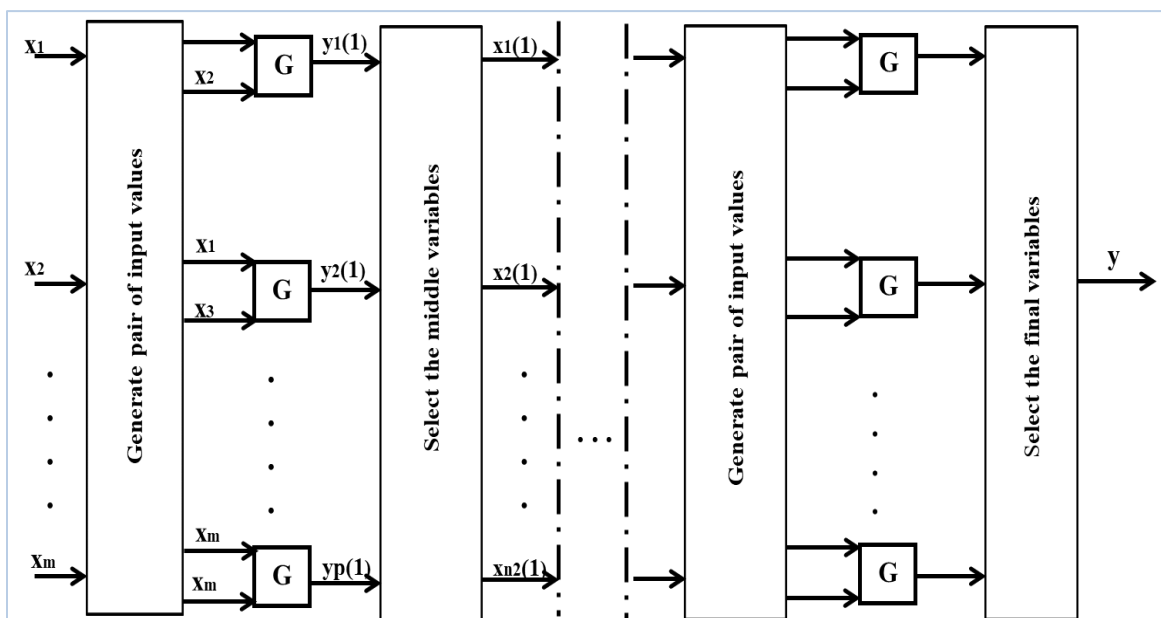


Figure 2: Schematic diagram of GMDH algorithm (Adapted from Li et al., 2017 p.9).

In Figure 2, x_i is the initial input variable, $y_i(k)$ is the output of the partial polynomials. G is the partial polynomials with quadratic polynomial for each two input variables. The partial polynomials are obtained by fitting the input data. $x_i(k)$ is the mediator, filtered by each layer criteria from $y_i(k)$, used as the input variable in the subsequent layer (Li et al., 2017).

During GMDH network design, the input dataset is split into training and test dataset(s). The training data is utilised to estimate the coefficients of the polynomial model, and the test data to choose the optimum model structure. The least squares minimization method is then applied to determine the polynomial coefficients for each of the nodal models. When all the possible outputs have been calculated, the estimated values of the neurons are crosschecked against the test data. The neurons whose mean-square-errors (MSE) are below the threshold (external criterion) were selected and the neuron with the smallest mean-square-error attained ($\min\text{MSE}_1$) also retained. The retained nodes are combined together to provide another set of inputs into the succeeding layer. The new layer's nodes are checked for compliance with the external criterion (MSE). The neurons with acceptable measure of fit are kept and the remaining neurons disposed. The best neurons are combined and assigned to nodes in the subsequent layer. Thereafter, the neurons estimated values are checked against test data to evaluate measure of fit and the process is continued iteratively until the optimal output node with smallest MSE achieved is selected. The quadratic polynomial connected to the optimal neuron is the non-physical model of the system (Voss, 2002; Nkurlu et al., 2020).

The experimental data collected for GMDH analysis was a statistic of evaluated BET surface areas for CNS activated carbon produced under different alkaline activation conditions. To improve GMDH modeling, the experimental dataset(s) were quadrupled to give a total of sixty (60) data-points (Onu et al., 2021), which were utilized in the GMDH analysis. The input dataset was subdivided into training and testing dataset(s), resulting in 51 training points utilized in estimation of the nodal polynomial equations, and 9 testing points utilized for ascertaining the fitness of the estimated polynomial equations in the network model.

The neural model training was carried out using GMDH source code which automates the training process.

3. RESULTS

3.1. Response surface modeling of CNS basic (ZnCl_2) activation process

A total of 54 experimental runs of Box Behnken (BBD) design were conducted by using the prepared activated carbon samples and the BET surface area(s) were measured. The Sequential Model Sum of Squares (SMSS) measures the desirability of each model for the activation process based on the Sum of Squares (SS) value, where appropriateness of the model for the process increases as the SS value increases (See Table 2). Consequently, the quadratic model was suggested by Design Expert Software for optimizing the achievable BET surface areas of produced ZnCl_2 -activated carbon(s).

Table 2: Sequential Model Sum of Squares Analysis [Type 1] for ZnCl₂ activated cashew nut shell.

Source	Sum of Squares	df	Mean Square	F-value	p-value	
Mean	5671257.41	1	5671257.41			
Linear	62129.44	3	20709.81	3.43	0.024	
2FI	81834.17	3	27278.06	5.82	0.00183	
Quadratic	153816.44	3	51272.15	33.85	1.69e-11	Suggested
Cubic	66652.97	3	22217.66			
Residual	0	41	0			
Total	6035690.43	54	111772.05			

The main and interaction effects were estimated by performing the Analysis of Variance (ANOVA). The significance probability value (P-value) was utilized to determine the model terms that are statistically significant. If the P-value is less than 0.05 it is safe to conclude that the effect (factor) under consideration is

significant at the 95% confidence level. The final model for the response was obtained by retaining only the significant factors ($P < 0.05$) based on the probability-test. The results of the ANOVA Analysis for the ZnCl₂ activated carbons are presented in Table 3.

Table 3: ANOVA Analysis for ZnCl₂ activated carbon.

Source	Sum of Squares	df	Mean Square	F-value	P-value
Model	2.978E+05	9	33086.67	21.84	< 0.0001
A-Activation temperature	1968.78	1	1968.78	1.30	0.2604
B-Activation time	48356.97	1	48356.97	31.92	< 0.0001
C-Impregnation ratio	8638.04	1	8638.04	5.70	0.0213
AB	774.51	1	774.51	0.5113	0.4784
AC	80599.21	1	80599.21	53.21	< 0.0001
BC	0.2139	1	0.2139	0.0001	0.9906
A ²	79093.85	1	79093.85	52.21	< 0.0001
B ²	432.94	1	432.94	0.2858	0.5956
C ²	58504.03	1	58504.03	38.62	< 0.0001
Residual	66652.97	44	1514.84		
Lack of Fit	66652.97	3	22217.66		
Pure Error	0.0000	41	0.0000		
Cor Total	3.644E+05	53			

The estimated response for BET surface area of ZnCl₂ activated cashew nutshell (CNS) is represented by Eq. 4:

$$\text{BETArea} = -1870.73 + 6.11 \times A - 3.70 \times B + 201.59 \times C + 0.00155 \times A \times B - 0.946 \times A \times C + 0.0086 \times B \times C - 0.0035 \times A^2 + 0.00648 \times B^2 + 271 \times C^2 \quad \text{Eq. (4)}$$

From the ANOVA for ZnCl₂-CNS presented in Table 3, it was observed that the P-value for the response surface model was less than 0.05 ($p\text{-value} < 0.0001$). This indicates that the second order polynomial model

is significant at the 95% confidence level. likewise, from the ANOVA results shown in Table 4, it can be concluded that the linear effects, Activation temperature (A), Impregnation ratio (C), the 2-way

interactions A*C (Impregnation ratio and Activation temperature), and the square effects A*A (Activation temperature product), C*C (Impregnation ratio product) had a statistically significant effect on the response, as all their P-values were not greater than 0.1 (Montgomery., 2017). On the other hand, the linear effect A (Activation temperature), 2-way interactions A*B (Activation temperature and Activation time), B*C (Activation time and Impregnation ratio), and the square effects B*B

(Activation time product) were found to be insignificant as their P-values were greater than 0.1 (Montgomery, 2017). Consequently, the conclusion can be reached that the studied response does not have any correlation with a change in these linear or combined independent variables i.e. A, A*B, B*C and B*B at specified values of the other variables (B&C), C, A, and (A&C) for the range of variables examined in Table 3. Therefore, eliminating all the insignificant terms, the final model is obtained as:

$$\text{BETArea} = -1870.73 - 3.70 \times B + 201.59 \times C - 0.946 \times A \times C - 0.0035 \times A^2 + 271 \times C^2 \quad \text{Eq. (5)}$$

The results of predicted response and experimental response are shown in Table 4.

Table 4: Model Predicted and Experimental BET Surface area for ZnCl₂ -activated CNS.

Point	BET Surface Area (Predicted)	BET Surface Area (Actual)	STD Error Fit	Square Residual
1	297.920	356.52	1.67387	3433.95
2	299.693	285.53	-0.40455	200.58
3	202.097	216.26	0.40455	200.58
4	231.700	173.10	-1.67387	3433.95
5	223.647	174.60	-1.40100	2405.63
6	381.285	405.00	0.67741	562.41
7	400.215	376.50	-0.67741	562.41
8	273.953	323.00	1.40100	2405.63
9	428.153	418.60	-0.27310	91.254
10	345.987	392.50	1.36911	2163.45
11	462.513	416.00	-1.36911	2163.45
12	380.863	393.60	0.37312	162.23
13	330.800	330.80	-0.00000	1.292E-26
14	330.800	330.80	-0.00000	1.292E-26
15	330.800	330.80	-0.00000	1.292E-26
16	297.920	356.52	1.67387	3433.95
17	299.693	285.53	-0.40455	200.58
18	202.097	216.26	0.40455	200.58
19	231.700	173.10	-1.67387	3433.95
20	223.647	174.60	-1.40100	2405.63
21	381.285	405.00	0.67741	562.41
22	400.215	376.50	-0.67741	562.41
23	273.953	323.00	1.40100	2405.63
24	428.153	418.60	-0.27310	91.254
25	345.987	392.50	1.36911	2163.45
26	462.513	416.00	-1.36911	2163.45
27	380.863	393.60	0.37312	162.23
28	330.800	330.80	-0.00000	1.292E-26
29	330.800	330.80	-0.00000	1.292E-26
30	330.800	330.80	-0.00000	1.292E-26
31	297.920	356.52	1.67387	3433.95
32	299.693	285.53	-0.40455	200.58
33	202.097	216.26	0.40455	200.58
34	231.700	173.10	-1.67387	3433.95
35	223.647	174.60	-1.40100	2405.63
36	381.285	405.00	0.67741	562.41
37	400.215	376.50	-0.67741	562.41
38	273.953	323.00	1.40100	2405.63

Point	BET Surface Area (Predicted)	BET Surface Area (Actual)	STD Error Fit	Square Residual
39	428.153	418.60	-0.27310	91.25
40	345.987	392.50	1.36911	2163.46
41	462.513	416.00	-1.36911	2163.46
42	380.863	393.60	0.37312	162.23
43	330.800	330.80	-0.00000	1.292E-26
44	330.800	330.80	-0.00000	1.292E-26
45	330.800	330.80	-0.00000	1.292E-26
46	297.920	356.52	1.67387	3433.95
47	299.693	285.53	-0.40455	200.58
48	202.097	216.26	0.40455	200.58
49	231.700	173.10	-1.67387	3433.95
50	223.647	174.60	-1.40100	2405.63
51	381.285	405.00	0.67741	562.41
52	400.215	376.50	-0.67741	562.41
53	273.953	323.00	1.40100	2405.63
54	428.153	418.60	-0.27310	91.25
				RMSE= 35.1

The graphical plot of the measured BET surface area against predicted BET surface area is shown in Figure 3.

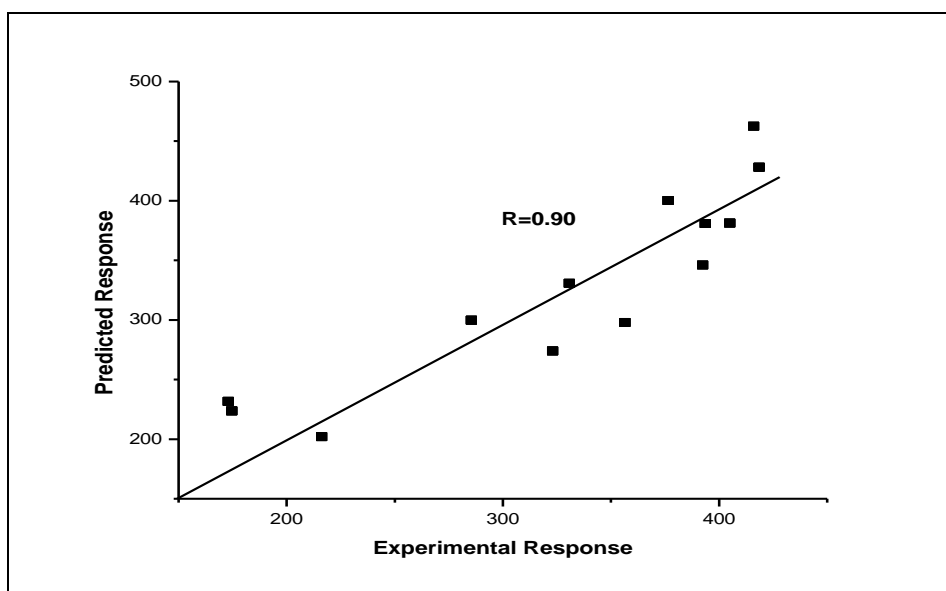


Figure 3: Plot of RSM predicted BET surface area against experimental data.

Figure 3 shows that the data points are un-evenly distributed about the 45° line without forming a definite pattern, indicating normality in the data values (minimum residual errors). Thus, signifying that the response surface model is adequate for predicting achievable surface area(s) of ZnCl₂-activated CNS. The high (correlation coefficient) R value of 0.90, confirmed that the achievable BET surface area for ZnCl₂-CNS activation can be predicted satisfactorily by the response model.

The normal plot of residuals depicted in Figure 4 was also utilised to check if the process data are normally distributed. The distribution of data points was similar at both the left and right portions of the plot, indicating normal distribution of the error residuals. This implies that there are no signs of problems with the process model or data (Antony, 2003).

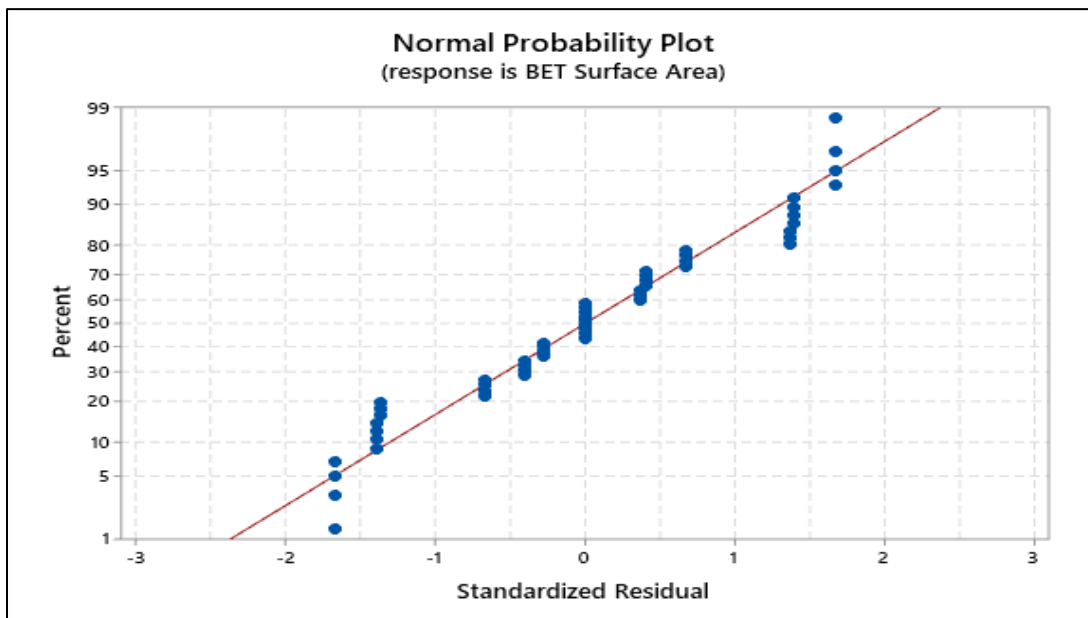


Figure 4: Normal Probability Plot of Residuals for the ZnCl₂ activated CNS.

The statistical significance of the estimated linear factors, interactions, and their products on the achievable BET surface area (studied response), in order of significance is represented by the Pareto diagram shown in Figure 5. The vertical (red) line

indicates the magnitude of the least statistically significant effect for a 95% confidence level and the corresponding t-test value is equal to 2.015. Any factor or its interaction that transcends the vertical line is considered significant (Montgomery, 2017).

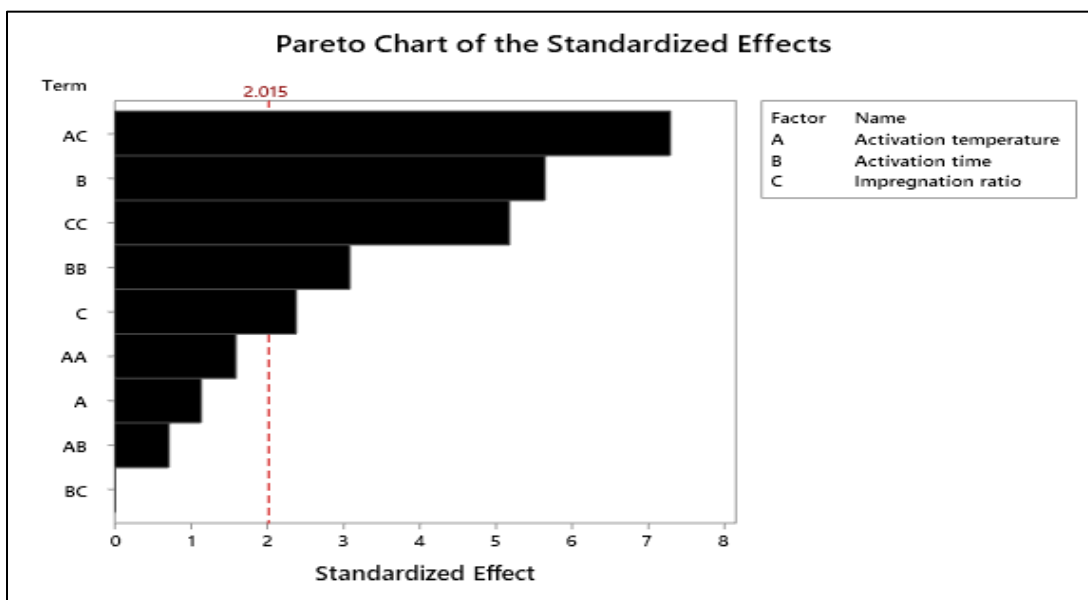


Figure 5: The Pareto plot for ZnCl₂ activated CNS.

Figure 5 shows that the most influential factors influencing the achievable BET surface area of ZnCl₂-activated CNS were the linear effect B (Activation time), 2-way interactions A*C (Activation temperature and Impregnation ratio), and the square effect C*C (Impregnation ratio product). Noteworthy, Prominent interactions are integral in attainment of overall process optimization.

The three dimensional (3-D) response surface plots generated to visualize the relationship between the independent variables (activation temperature, time, impregnation ratio) and response of interest (BET surface area) in terms of main, and interaction effects and also facilitate optimization of the ZnCl₂ activated CNS production process are showcased in Figure 6.

Each of the response diagrams were plotted as a function of two process variables in their respective

ranges (-1 to 1), with the third independent variable(s) was maintained at median (zero) level.

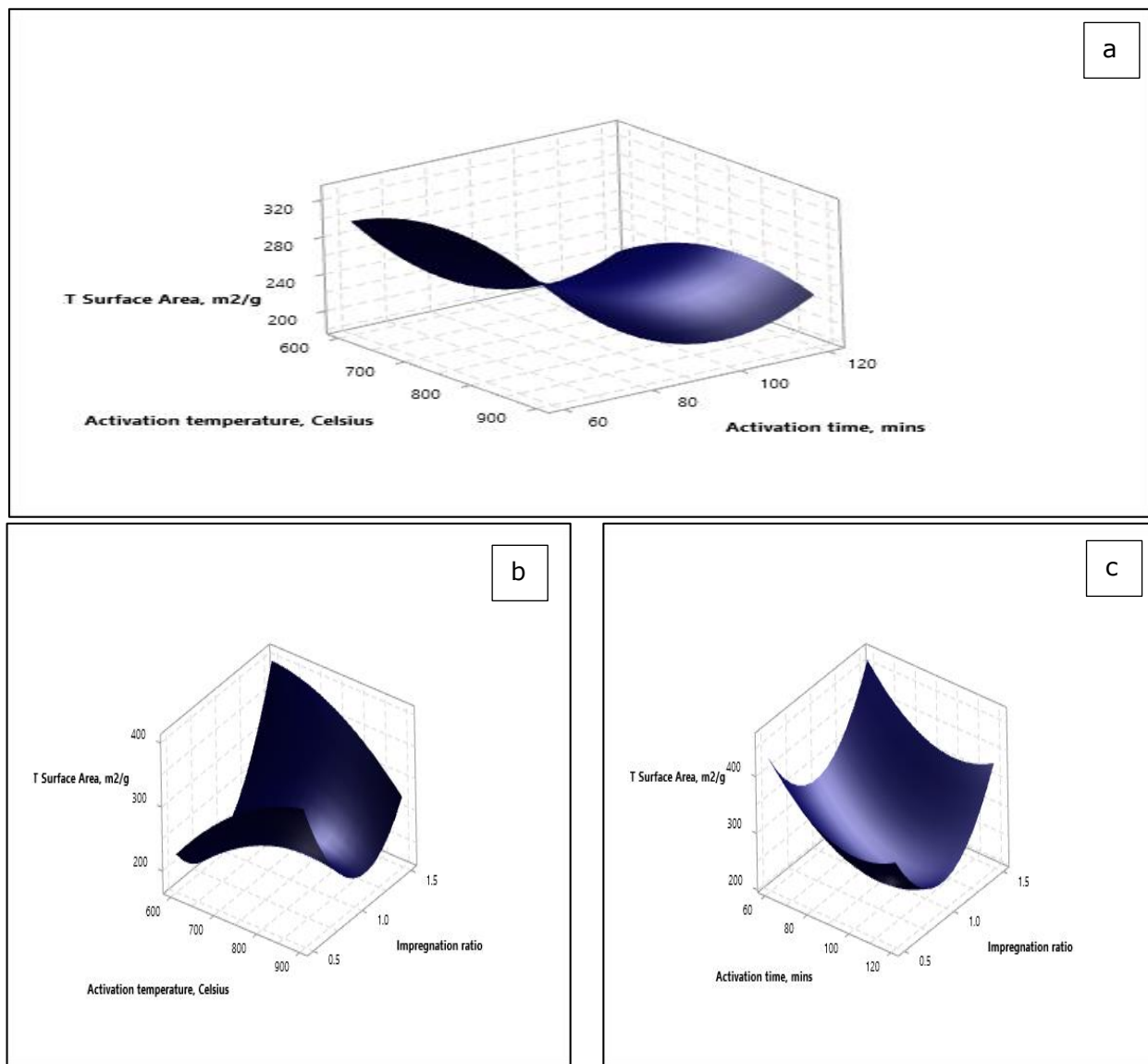


Figure 6: Response surface plots of BET surface area for (a) Impregnation ratio = 1.0 (b) Activation time = 90 min, and (c) Activation temperature = 750 °C.

From Fig 6a, it is evident that the BET surface area of ZnCl₂ activated carbon showed a slight decreasing trend with increase in activation temperature. Likewise, the estimated BET surface area of ZnCl₂ activated carbon showed a decreasing trend with increase in activation time. In Figure 6b, the BET surface area of ZnCl₂ activated carbon showed an increasing trend with increase in activation temperature, whilst the BET surface area of ZnCl₂ activated carbon initially showed decreasing trend with increasing impregnation ratio towards a minimum, and subsequently plateaued to a constant level. It is also apparent from Figure 6c, that the BET surface area of

ZnCl₂ activated carbon showed a decreasing trend with increasing activation time. Whereas, estimated BET surface area showed an increasing trend with increase in impregnation ratio towards a maximum level. Notably, the adsorption capacity of the prepared activated carbons is contingent on impregnation ratio, which produces additional surface active (binding) sites (Marsh and Reinoso, 2006). Consequently, it is important that impregnation ratio is considered in future optimization studies.

From the statistical optimization, the optimum BET surface area attained for ZnCl₂ activated CNS was

504m².g⁻¹ for activation temperature of 873K, activation time of 60min, and impregnation ratio of 1.50 respectively. Lastly, additional experimental run(s) using the optimal conditions was carried out,

and the empirical BET surface area for ZnCl₂ activated CNS was found to be 492m².g⁻¹ (See Table 5). These results validated the polynomial model explicated with RSM.

Table 5: Predicted and Observed Value(s) of BET surface area for ZnCl₂ activated CNS utilizing optimal activation conditions.

No of Replicates	Optimal Conditions			BET Surface Area (m ² /g)	
	Activation Time, min	Activation Temperature, K	Impregnation ratio	Experimental	Predicted
1	60	873	1.50	492	504

3.1.2. Modeling of the CNS base (ZnCl₂) activation process using GMDH

The GMDH-type neural model was implemented in MATLAB R2018a version 9.4. The architecture of the built GMDH network consists of one input layer, two hidden layers, in combination with one output layer as

shown in Figure 7. A total of two neurons were included in the first layer, and one neuron in the second layer of the model. After completion of network training using the training dataset with three inputs (activation time, activation temperature and impregnation ratio), the simulated (output) result was checked with the test data to determine its computation accuracy.

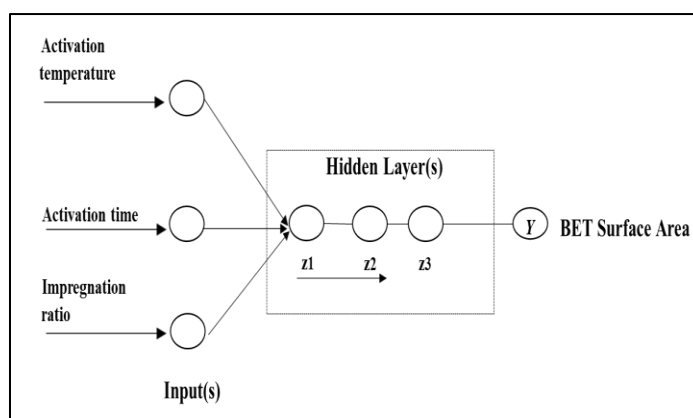


Figure 7: Architecture of proposed GMDH-type BET neural network.

The regression plots of training, overall, and evaluation are displayed in Figure 8 for the GMDH-type neural model. The optimal model for ZCNS activation corresponded to correlation coefficient (R) of 0.864 for training, and 0.932 for testing yielding an average R value of 0.925, indicating strong connection between

the input values and GMDH-type neural network predictions for achievable surface area (Nkurlu et al., 2020). This finding is also corroborated by the relatively low value obtained for the performance function (RMSE = 32.0).

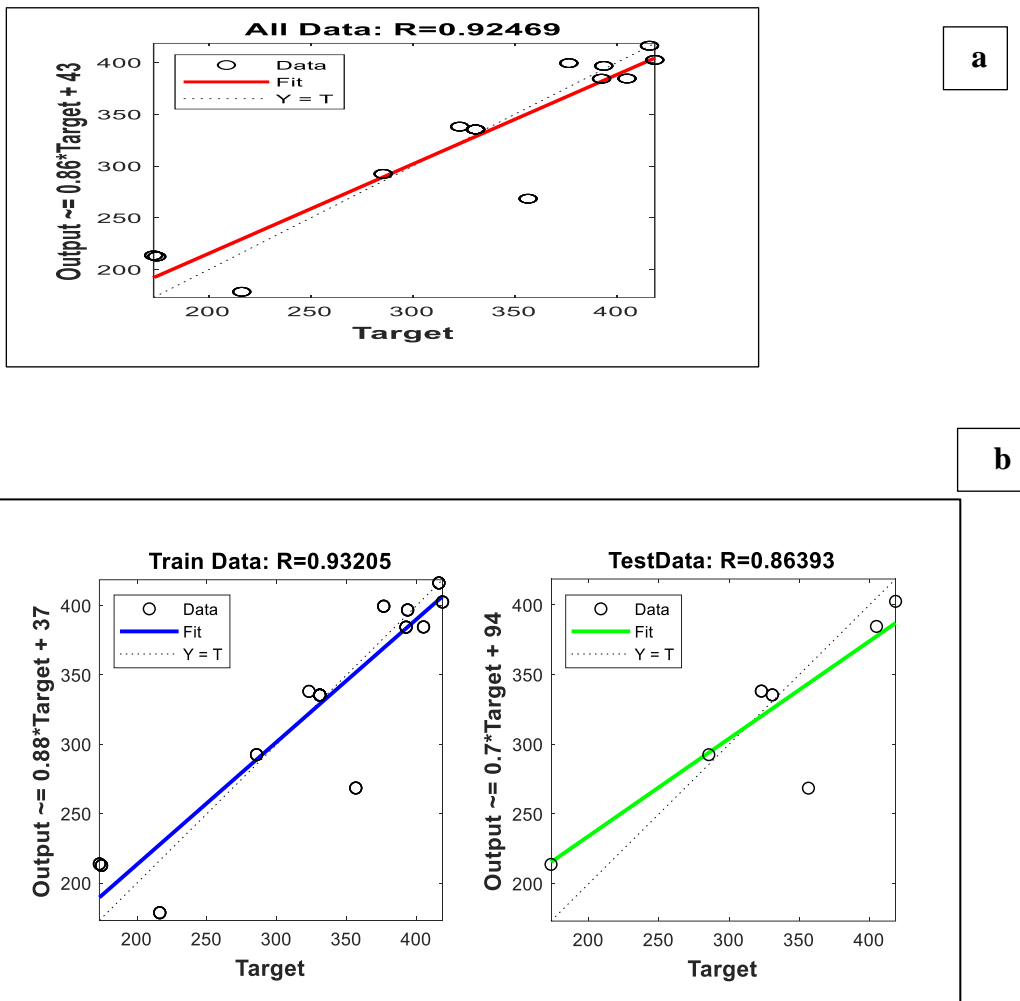


Figure 8: GMDH Regression plots for (a) overall (b) training, and testing data.

The GMDH-type neural model was further studied by comparing the GMDH prediction (outputs) and experimental outcomes (targets) for achievable BET surface area(s), as depicted in Figure 9.

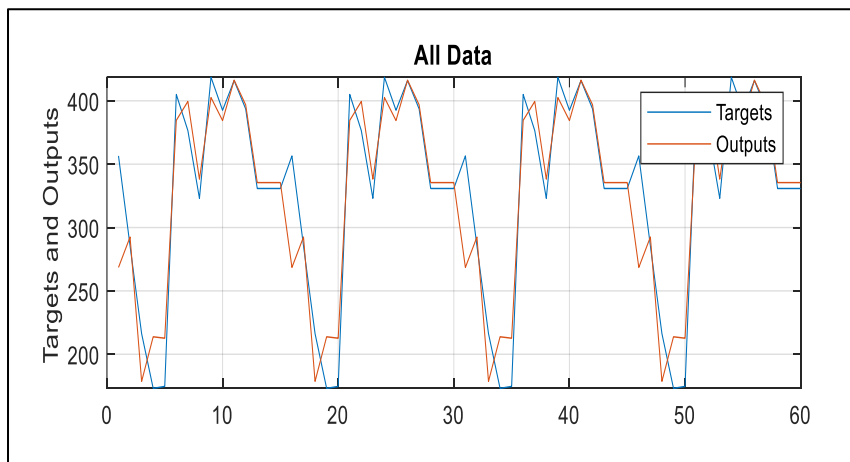


Figure 9: Cross-plot of experimental (target) and simulated (output) results for the ZCNS activation process.

From Figure 9, it is lucid that the target (experimental) and simulated (output) values match well, as confirmed by the moderately low value of the error function (RMSE=32.0) hitherto obtained. Hence, the GMDH-type neural model was able to successfully map the experimental domain, allowing for reasonably accurate estimate(s) of intermittent variations in the achievable BET surface area(s) of ZCNS.

The efficiency of the created RSM (BBD) and GMDH-type BET neural models in predicting the achievable BET surface areas were evaluated using standard statistical indices-squared loss function and root mean squared error (RMSE) as shown in Table 6 (Ayoub et al., 2019; Chebii et al., 2022). The performance index-squared loss function is a good indicator of model predictive ability, because it is very sensitive to outliers and non-negative (Gokcesu, and Gokcesu., 2023).

3.1.3. Comparative Analysis of GMDH-type and RSM BET models

Table 6: Comparison of GMDH-type and RSM BET models for ZCNS activation process.

Run No	RSM	GMDH
	Square Residual	Square Residual
1	3433.95	7747.10
2	200.58	48.78
3	200.58	1417.92
4	3433.95	1655.27
5	2405.63	1448.49
6	562.41	417.059
7	562.41	528.18
8	2405.63	229.34
9	91.25	257.031
10	2163.45	65.191
11	2163.45	0.0767
12	162.23	10.31
13	1.29E-26	21.634
14	1.29E-26	21.634
15	1.29E-26	21.634
16	3433.95	7747.10
17	200.58	48.790
18	200.58	1417.92
19	3433.95	1655.27
20	2405.63	1448.49
21	562.41	417.06
22	562.41	528.18
23	2405.63	229.344
24	91.25	257.031
25	2163.45	65.191
26	2163.45	0.0767
27	162.23	10.307
28	1.29E-26	21.634
29	1.29E-26	21.634
30	1.29E-26	21.634
31	3433.95	7747.10
32	200.58	48.787
33	200.58	1417.92
34	3433.95	1655.27
35	2405.63	1448.49
36	562.41	417.06
37	562.41	528.178
38	2405.63	229.344
39	91.254	257.031
40	2163.45	65.191
41	2163.45	0.0767
42	162.23	10.307

Run No	RSM	GMDH
	Square Residual	Square Residual
43	1.29E-26	21.634
44	1.29E-26	21.634
45	1.29E-26	21.634
46	3433.95	7747.10
47	200.58	48.79
48	200.58	1417.92
49	3433.95	1655.27
50	2405.63	1448.49
51	562.41	417.06
52	562.41	528.178
53	2405.63	229.344
54	91.25	257.031
	RMSE= 35.10	RMSE = 32.0

The RSM and GMDH-type BET models generated squared-error residual values ranging from 1.29×10^{-26} to 3434, and 7.67×10^{-2} to 7747 respectively for achievable BET surface area(s). The lower value(s) of the loss function ascertained for RSM BET model, suggests that the RSM BET predictive model performs better than GMDH. Consequently, the comparatively higher squared-error residual values obtained for GMDH, necessitated further error analysis. From Table 7, Root mean squared error (RMSE) values of 32.0 and 35.10 respectively were also recorded for the GMDH-type and RSM BET models. According to Chebii et al., (2022), RMSE is a standard statistical index for valuating the performance of nonlinear regression

models. The lower RMSE value ascertained for GMDH, confirmed that GMDH model is the more appropriate model for predicting the achievable surface area of ZCNS. Overall, RSM and GMDH techniques have been evidenced to be effective methods for delineating the ZnCl_2 -activated CNS production process.

4. SENSITIVITY ANALYSIS

Sensitivity analysis was carried out to investigate the influence of activation parameters (impregnation ratio, activation time, & activation temperature) on the predicted BET surface experimental data conducted utilising Eq. (6) (Nkurlu et al., 2020):

$$S = \frac{1}{N} \sum_{i=1}^N \left(\frac{\text{percent change in output}}{\text{percent change in input}} \right)_i \times 100 \quad \text{Eq. (6)}$$

Where N is the total number of experimental runs, i is the respective data point, and S is sensitivity value. The lower the S value, the less the activation (process) variable affected the simulated BET surface area value.

Contrariwise, the higher the S value, the greater the input activation variable influences the simulated BET surface area of ZCNS (Nkurlu et al., 2020).

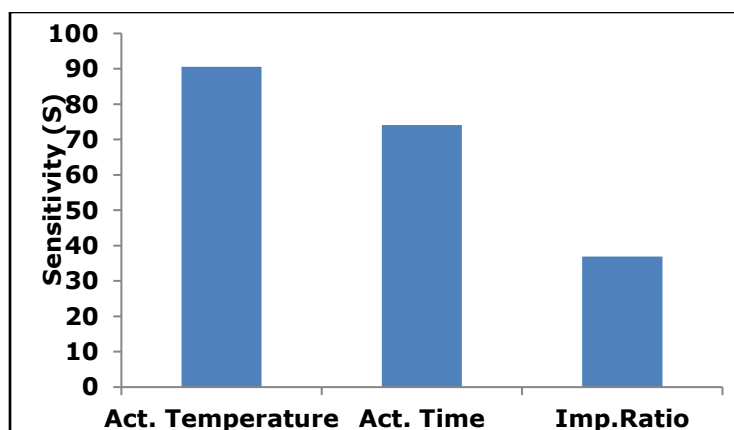


Figure 10: Effect of GMDH input variables on ZnCl_2 -CNS activation process.

From Figure 10, both activation temperature and time had more significant impact on GMDH BET predictive model than impregnation ratio with S values of 90.6% and 74.1% respectively. The low S value of 36.9%

obtained for impregnation ratio signifies that this input had little effect on the BET surface area prediction(s).

5. CONCLUSIONS

In this study, Box Behnken design (BBD) of Response Surface Methodology (RSM)) and novel Group Method of Data Handling (GMDH) approaches were employed to optimize the conditions for production of ZCNS with high BET surface areas. The RSM and GMDH-type neural models obtained via regression analysis and multi-layered iterative algorithm (MIA) respectively, predicted the response of interest ((BET surface area) fairly accurately. The highest BET surface area for ZCNS obtained from RSM optimisation was estimated to be 504 m².g⁻¹ attained at optimal process conditions of activation time (60 min), impregnation ratio (1.50), and activation temperature (873K). The optimal GMDH-type BET model was identified to consist of 3 input variables, and 2 hidden layer(s) having two and one neuron(s) respectively. The root mean square error (RMSE) and correlation coefficient (R) were chosen as statistical indices for evaluating the predictive models performance. With the least RMSE (32.0), and highest correlation coefficient (0.925), The GMDH-type BET model proved to be better compared to the RSM model. These findings confirmed that GMDH-type BET model has the best analytical performance. Lastly, the sensitivity analysis outcome unveiled that activation temperature and activation time had a predominant influence on the performance of the GMDH-type BET neural model.

6. ACKNOWLEDGEMENTS

The authors will like to acknowledge Engr Christopher Obi of Polymer Engineering Department, Nnamdi Azikiwe University, Awka for proof-reading the final manuscript and suggesting a few corrections.

7. REFERENCES

- Adeigbe, O. O., Olasupo, F. O., Adewale, B. D., & Muyiwa, A. A. (2015). A review on cashew research and production in Nigeria in the last four decades. *Scientific Research and Essays*, 10(5), 196–209. <https://doi.org/10.5897/SRE2014.5953>
- AJEMBA, R. O. (2014). Kinetics and equilibrium modeling of lead (II) and chromium (III) ions' adsorption onto clay from Kono-bowe, Nigeria. *Turkish Journal of Engineering and Environmental Sciences*, 38(3), 455–479.
- Akinbiyi, A. O. (2001). *Removal of lead from aqueous solutions by adsorption using peat moss*. Faculty of Graduate Studies and Research, University of Regina.
- Anderson, M. J., & Whitcomb, P. J. (2016). *RSM Simplified: Optimizing Processes Using Response Surface Methods for Design of Experiments, Second Edition* (2nd ed.). Productivity Press.
- Ayoub, Mohammed. A., Almansour, Abdullah. O., & Hassan, Anas. M. (2020). A Novel Formula for Estimating Oil Compressibility Below Bubble Point Pressure Using Group Method of Data Handling: A Comparative Approach. *Day 1 Tue, October 29, 2019*, D012S002R001. <https://doi.org/10.2118/196446-MS>
- Buasri, A., Sirikoom, P., Pattane, S., Buachum, O., & Loryuenyong, V. (2023). Process Optimization of Biodiesel from Used Cooking Oil in a Microwave Reactor: A Case of Machine Learning and Box–Behnken Design. *ChemEngineering*, 7(4), 65. <https://doi.org/10.3390/chemengineering7040065>
- Chebii, S. J., Mukolwe, M. M., & Ong'or, B. I. (2022). River flow modelling for flood prediction using artificial neural network in ungauged Perkerra catchment, Baringo County, Kenya. *Water Practice and Technology*, 17(4), 914–929. <https://doi.org/10.2166/wpt.2022.034>
- Dawei, H. (2012). *Concise Environmental Engineering*. Ventus Publishing ApS.
- Demirbas, E., Kobya, M., & Konukman, A. E. S. (2008). Error analysis of equilibrium studies for the almond shell activated carbon adsorption of Cr(VI) from aqueous solutions. *Journal of Hazardous Materials*, 154(1–3), 787–794. <https://doi.org/10.1016/j.jhazmat.2007.10.094>
- Elibol, M. (2002). Response surface methodological approach for inclusion of perfluorocarbon in actinorhodin fermentation medium. *Process Biochemistry*, 38(5), 667–673. [https://doi.org/10.1016/S0032-9592\(02\)00171-1](https://doi.org/10.1016/S0032-9592(02)00171-1)
- Essa, M. H., Zahrani, M. A. A., & Nesaratnam, S. (2013). Optimisation of activated carbon production from date pits. *International Journal of Environmental Engineering*, 5(3), 325. <https://doi.org/10.1504/IJEE.2013.054708>
- Farlow, S. J. (1981). The GMDH Algorithm of Ivakhnenko. *The American Statistician*, 35(4), 210–215. <https://doi.org/10.1080/00031305.1981.10479358>
- Gokcesu, K., & Gokcesu, H. (2023). *A Note On Nonlinear Regression Under L2 Loss*. <https://doi.org/10.48550/ARXIV.2303.17745>
- Kehinde Ademola, Adesanya, Mutiat Oluwaseyi Agboola-Adedoja, Adejoke Adebisola Adelusi, Qudus Adebayo Ogunwolu, Chinweike Abednego Ugwu, Modinat Adewunmi Alli, & Ayodele Oladipo Akinpelu. (2021).

- Opportunities in Nigerian cashew nut value chain. *World Journal of Advanced Research and Reviews*, 9(1), 168–174. <https://doi.org/10.30574/wjarr.2021.9.1.0008>
- Kulkarni, S. J., & Kaware, J. (2014). Removal of phenol from effluent in fixed bed: A review. *International Journal of Engineering Research and General Science*, 2(5), 35–38.
- Li, R. Y. M., Fong, S., & Chong, K. W. S. (2017). Forecasting the REITs and stock indices: Group Method of Data Handling Neural Network approach. *Pacific Rim Property Research Journal*, 23(2), 123–160. <https://doi.org/10.1080/14445921.2016.1225149>
- Madala, H. R., & Ivakhnenko, A. G. (1994). *Inductive learning algorithms for complex systems modeling*. CRC Press.
- Malik, D. S., Jain, C. K., & Yadav, A. K. (2017). Removal of heavy metals from emerging cellulosic low-cost adsorbents: A review. *Applied Water Science*, 7(5), 2113–2136. <https://doi.org/10.1007/s13201-016-0401-8>
- Mathew Nkurlu, B., Shen, C., Asante-Okyere, S., Mulashani, A. K., Chungu, J., & Wang, L. (2020). Prediction of Permeability Using Group Method of Data Handling (GMDH) Neural Network from Well Log Data. *Energies*, 13(3), 551. <https://doi.org/10.3390/en13030551>
- Montgomery, D. C. (2017). *Design and analysis of experiments* (Ninth edition). Wiley.
- Nwabanne, J. T., & Okoye, A. C. (2013). Treatment of synthetic and battery industry wastewater by electrocoagulation. *Der Chemica Sinica*, 4(6), 32–39.
- Okewale, A., Igbokwe, P., & Adesina, O. (2015). Optimization of the adsorptive dehydration of ethanol–water system. *Optimization*, 39.
- Okiy, K. V. (2006). *Scale-up of an electrochemical reactor for the removal of copper ions from wastewater* [B. Sc. Thesis]. University of Lagos.
- Onu, C. E., Nwabanne, J. T., Ohale, P. E., & Asadu, C. O. (2021). Comparative analysis of RSM, ANN and ANFIS and the mechanistic modeling in eriochrome black-T dye adsorption using modified clay. *South African Journal of Chemical Engineering*, 36, 24–42. <https://doi.org/10.1016/j.sajce.2020.12.003>
- Özer, A., Gürbüz, G., Çalimli, A., & Körbahti, B. K. (2009). Biosorption of copper(II) ions on *Enteromorpha prolifera*: Application of response surface methodology (RSM). *Chemical Engineering Journal*, 146(3), 377–387. <https://doi.org/10.1016/j.cej.2008.06.041>
- Palani, S., Liong, S.-Y., Tklich, P., & Palanichamy, J. (2009). Development of a neural network model for dissolved oxygen in seawater. *Indian Journal of Geo-Marine Sciences*, 38(2), 151–159.
- Peavy, H. S., Rowe, D. R., & Tchobanoglous, G. (1985). *Environmental engineering*. McGraw-Hill.
- S, M. S., M, E. A. A., & Chidambaram, R. (2015). Isotherm Modelling, Kinetic Study and Optimization of Batch Parameters Using Response Surface Methodology for Effective Removal of Cr(VI) Using Fungal Biomass. *PLOS ONE*, 10(3), e0116884. <https://doi.org/10.1371/journal.pone.0116884>
- Senthil Kumar, P., Ramalingam, S., Abhinaya, R. V., Kirupha, S. D., Murugesan, A., & Sivanesan, S. (2012). Adsorption of Metal Ions onto the Chemically Modified Agricultural Waste. *CLEAN – Soil, Air, Water*, 40(2), 188–197. <https://doi.org/10.1002/clen.201100118>
- Singh, R., Gautam, N., Mishra, A., & Gupta, R. (2011). Heavy metals and living systems: An overview. *Indian Journal of Pharmacology*, 43(3), 246. <https://doi.org/10.4103/0253-7613.81505>
- Srivastava, S., Agrawal, S. B., & Mondal, M. K. (2015). A review on progress of heavy metal removal using adsorbents of microbial and plant origin. *Environmental Science and Pollution Research*, 22(20), 15386–15415. <https://doi.org/10.1007/s11356-015-5278-9>
- Stavropoulos, G. G., & Zabaniotou, A. A. (2009). Minimizing activated carbons production cost. *Fuel Processing Technology*, 90(7–8), 952–957. <https://doi.org/10.1016/j.fuproc.2009.04.002>
- Subramaniam, R., & Kumar Ponnusamy, S. (2015). Novel adsorbent from agricultural waste (cashew NUT shell) for methylene blue dye removal: Optimization by response surface methodology. *Water Resources and Industry*, 11, 64–70. <https://doi.org/10.1016/j.wri.2015.07.002>
- Van Dyk, L. D. (2000). *The production of granular activated carbon from agricultural waste products* [MSc Thesis, Stellenbosch University]. <https://scholar.sun.ac.za/items/388fda93-974e-4e4d-9562-0e78cc0f8c31>

Okuy, K. V., Nwabanne, J. T. (2024), JOTCSB, 7(1), 25-42.

Voss, M. S. (2002). *The Group Method for Cartesian Programming: A New Methodology for Complex Adaptive Functional Networks* [PhD Thesis, Marquette University].
https://epublications.marquette.edu/cgi/viewcontent.cgi?article=2797&context=dissertations_mu

Wang, Z., Wu, Q., Zhang, J., Zhang, H., Feng, J., Dong, S., & Sun, J. (2019). In situ polymerization of magnetic graphene oxide-diaminopyridine composite for the effective adsorption of Pb(II) and application in battery industry wastewater treatment. *Environmental Science and Pollution Research*, 26(32), 33427–33439. <https://doi.org/10.1007/s11356-019-06511-1>

Xu, Z., Cai, J., & Pan, B. (2013). Mathematically modeling fixed-bed adsorption in aqueous systems. *Journal of Zhejiang University SCIENCE A*, 14(3), 155–176.
<https://doi.org/10.1631/jzus.A1300029>

Yi, Q. (2009). *Point Sources of Pollution: Local Effects and their Control—Volume II*. EOLSS Publications.
<https://books.google.com.tr/books?id=dq2kCwAAQBAJ>



Ink Migration Barrier and Direct Food Contact Heat Sealing Lacquer Design for Aluminum / Pet Blister Structure

Gizem Topçuoğlu¹ , Canan Uraz^{2*} 

¹Sun Chemical Corporation, ALOSBI, 5004 St. No:10 Aliağa, 35800, İzmir / Türkiye

²Ege University, Faculty of Engineering, Department of Chemical Engineering 35100 Bornova-İzmir, Turkey

Abstract: The packaging industry as a pioneer in waste production is looking for environmentally friendly and green solutions in these days. These factors are driving the development of packaging and forcing the industry to invest in research and development to make flexible packaging more sustainable than the existing packaging options. In this review, the factors of main ingredient's selection on migration barrier properties have been investigated within the new designed heat-sealing lacquer. The new heat-sealing lacquer design has been carried out, which will ensure thermal sealing in Aluminum/Pet Blister Packaging structure, suitable for direct contact food, and at the same time prevent the migration of printed ink to the secondary packaging layer, Pet film side. Because of laboratory tests, the effects and results of heat-sealing lacquer formulations have been assessed and prevented the negative ink migration tendencies in existing heat-seal lacquers for blister packaging structure. That would be possible to use the obtained PET film by recycling processes as a green solution to flexible packaging sector. In this way, Pet films can be separated and used in recycling processes when blister packaging printed with new designed heat-sealing lacquer.

Keywords: Blister packaging, direct food contact, heat-seal lacquer, migration, recycling process.

Submitted: December 14, 2023. **Accepted:** January 22, 2024.

Cite this: Topçuoğlu, G., & Uraz, C. (2024). Ink Migration Barrier and Direct Food Contact Heat Sealing Lacquer Design for Aluminum / PET Blister Structure. Journal of the Turkish Chemical Society, Section B: Chemical Engineering, 7(1), 43-52. <https://doi.org/10.58692/jotcsb.1404932>.

***Corresponding author. E-mail:** canan.uraz@ege.edu.tr.

1. INTRODUCTION

In our daily lives, flexible packaging plays an important role in the preservation, storage, distribution and marketing of food and derivatives. Packaging materials as a principal function is to keep food safe. It protects food from any damage during the transfer to consumer. The other important function is to attract the consumer's attention. Therefore, the design of packaging and the inks that are applied on packaging are important phenomena on the perspectives of marketing. Therefore, the widespread use of plastic based, flexible packaging materials have caused about the waste problem for environment in the last 50 years (TurkChem, 2020). Turkish Plastics Industry published a report on Turkey's environment issues in 2020, report is pointing to 9.54 million tons of plastic are produced in Turkey market in a year. Packaging material wastes constitute 41.9% by weight of the plastic consumed plastic amount (Plastics Industry Report, 2020). Despite this high rate, just 4.46% of these consumed plastic wastes

can be collected in our country for recycling (Pagder, 2020). Based on literature survey and on author's knowledge at the situation in the world, the market research shows that 146 million tons thousand tons of plastic packaging is consumed to waste in world in 2015. Against that huge consumption, only approximately 29.2 million tons of this is collected for recycling in 2016 (Ritchie, 2018).

Figure 1 shows that packaging wastes are dominant for the waste generation globally accounting for 47 percent between 2015 and 2021. The other sectors are others, textile, personal care, storage wastes, construction, and electrical equipment, respectively. Figure 2 represents the waste management percentages in world again between years 2015 and 2021. It can be understood that only 19% of these collected packaging wastes are managed as suitable for recycling. A large portion of

these wastes is going to landfilling or the natural environment and incineration (Ritchie, 2018).

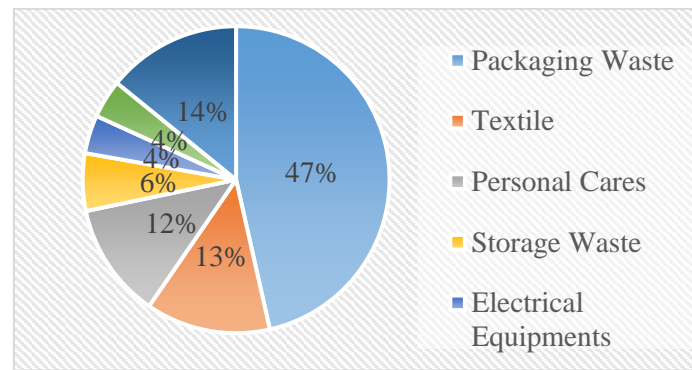


Figure 1: Waste generation in world between 2015 and 2021(Ritchie, 2018)

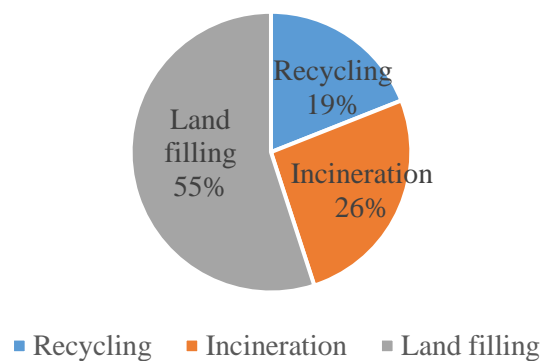


Figure 2: Waste management in world between 2015 and 2021 (Ritchie, 2021)

So that, recycling of these packaging wastes is a necessity. The increasing awareness of environmental protection and economic consideration direct us to regain these values, which are classified as a waste. These waste materials are our valuable raw materials stocks and energy stocks, which can be recyclable.

The packaging industry is seeking for innovative environmental solutions to avoid depleting raw material reserves. The environmental pollution can be decreased by the help of new environmentally designs for packaging sector. The main result of that small amount of recycling rate can cause the impurities on consumed packaging materials. However, the inks and paints applied on packaging materials cause a migration that pollutes flexible packaging materials. As a result, consumed packaging material will not be suitable for recycling processes due to stain and impurities on it. A study by Pinter et al. also showed that contamination issues affect the quality of the recycled material in terms of opacity and densitometric color properties. Blushing and staining by any ink are considered as unrequested parameters for mechanical recycling. Because of these impurities in recycling processes, the recycling rates and repetition are reducing. Today, PET packages constitute the biggest consumption amount plastic wastes. Therefore, blister packaging has experienced noticeable growth over the past years. The blister packaging market

was valued at USD 21.3 billion in 2020. Blister Packaging is projected to be worth USD 38.17 billion by 2027. The compound annual growth rate (CAGR) of 7.2% during the forecast period (2021 - 2027) (Blister Packaging Market Report, 2021). Thereof, recycling of PET wastes has become an important phenomenon because of increasing awareness of environmental protection, economic requirements, and raw material depletions. According to market research and available data, we can understand that PET is one of the most common thermoplastic polymers for packaging industry. Again, in 2021, Pinter et al, considered that PET would be the most recyclable food-packaging plastic. The use of this material is expected to increase. The reason behind is to ability of absorption of post-consumer contaminations at lower levels, when we evaluate with other plastics like polyethylene and polypropylene. That chemical characteristic of PET makes it more acceptable for the recycling process in terms of high recycling rate and percent of usage values (Pudack et al., 2019).

These huge consumptions and forecast amounts again direct us to the necessity of recycling. The widespread use, chemical and commercial properties need to be evaluated in terms of the environment. Therefore, every product that is placed on the market should include some thought to its end-of-life and how its associated packaging will be disposed of and recycled. The biggest

parameter preventing this recycling of PET is that the material is contaminated with ink.

The aim of this study is to design a heat-sealing lacquer, which will prevent contamination of ink to PET material used in blister packaging. The new heat-sealing lacquer design prevents the transfer of ink to secondary substrate, PET material after sealing. The migration of ink from aluminum material to PET film because of the heat-sealing process. The newly designed formulation of heat-sealing lacquer prevents ink migration that pollutes flexible packaging materials. With the help of a new design heat-sealing lacquer, the obtained PET film after separation processes can be suitable to reprocess in recycling processes for sustainability. The new heat-sealing lacquer is also designed to allow recycling and at the same time, it will be

suitable for direct food contact (DFC) product status. The improved packaging will provide food safety and help reduce the carbon footprint by the help of recycling of packaging material. Thereby, significantly contributing to the sustainability of the recycling of PET can be available.

2. EXPERIMENTAL SECTION

2.1. Packaging Materials

The blister packs are combined with two different films. The primary material is aluminum film which the design to be printed with ink and the secondary (other) material is PET film. Both materials are adhered with thermally to create blister packaging (Allen, 2010).

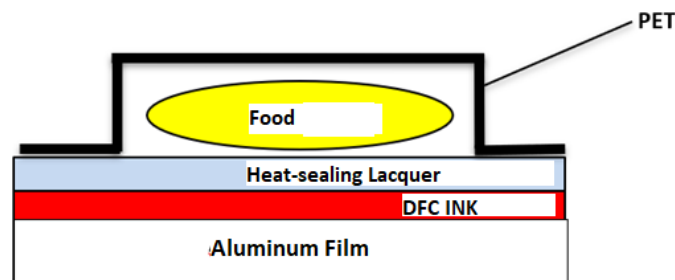


Figure 3: Blister Packaging Structure.

The heat-sealing lacquer and the printing ink are two main components that accompany these two major layers. The first component ink supply packaging's visual design, aesthetic, and instructive aspects. Another component, heat-sealing lacquer is applied for giving adhesion between the two halves of the blister. Figure 3 shows the direction of heat seal lacquer application side and structure of the blister packaging. Heat seal lacquer applied on the primary material, which is aluminum foil on the top of ink printed designs. This application provides sealing between primary material and the secondary material, which is PET film by the help of heat-sealing lacquer. Sealing of flexible packaging film can be closed by the most common method which has been done by seal bar (seal jaw) sealing in the food industry (Ilhan et al., 2021).

2.2. Methods

After detailed literature and market research related the DFC HSL groups done, the formulations of heat-sealant lacquer have been developed with various resin groups belongs to variable producer which learnt from literate survey and old experiences on heat-sealing lacquers. The heat-sealing lacquer designed in this study prevents the migration of ink to the PET film while providing thermal sealing in blister packaging applications with the help of compatible resin and additive selection. Thus, PET film is not contaminated and stained with ink. It is possible to use the obtained PET film by recycling as pure material source again. Therefore, heat-sealing lacquer allows excellent thermal sealing of used materials. Therefore, as a primary packaging level based on the product's proximity and intended usage of blister packs are in direct contact with the food products (Lalpuria et al., 2012).



Figure 4: Current Heat-Sealing Lacquer Applied PE Film.



Figure 5: New Heat-Sealing Lacquer Applied PET Film.

In Figure 4 shows that when the blister packaging, which applied with current heat-sealing lacquer, separated, the ink migrates from aluminum material to PET. Since the PET film is contaminated with ink, it cannot be recycled. However, with the new study, as seen in Figure 5, there is no ink contamination have been seen on separate PET film. When the PET film is separated from the aluminum after the heat-sealing process, the PET film stays clean which is suitable for recycling.

Experimental studies were first named ADHS coding system to understand the effect of resin types initially. Then, within selected resins, HSL formulation studies were followed to heat seal formulation roofs to find the best match with the desired design parameters. All the test measurements were carried out at Sun Chemical facilities.

In laboratory tests, the selection of resin types has been evaluated according to their following fundamental requirements initially.

- Adhesion
- Heat sealing strength
- Ink migration properties on PET, after separation of structure

In all formulations, the solid contents of variable resins were set to 25% value for fair consideration of resin selections. Out of 28 commonly used resin types, 8 of them were chosen according to the performances below. The new formulations of heat-sealing lacquer have been developed with these selected resin groups.

- Film-forming properties
- Adhesion
- Sealing strength
- Tear resistance
- Resistance properties (heat, mechanical and chemical)
- Solvent release

- Anti-blocking property
- Stability

In addition, non-migratory resin type for protecting ink contamination to PET side was the most important phenomena for these selections. Extra performance and resistance properties that could be obtained with the use of more than one resin were evaluated. Thus, co-binder usage was evaluated; the compatibility of resins was tested. As a second step of study, additive usage in formulations gives other wanted properties of formulations. Additives alter the lacquer physical properties to boost different situations, like enhancing the flexibility of the printed film, increasing mechanicals resistance such scrub, rub off. Additionally, they can promote adhesion, surface properties and other required special effects.

Formulation structures that would not cause the migration of ink and any ink stain to the PET film side after separation of blister pack while providing thermal sealing in blister packaging applications were tested.

3. RESULTS AND DISCUSSION

3.1. Adhesion Control and Viscosity Measurements

Adhesion as a control parameter is the primary requirement as mentioned before for designed lacquer. Therefore, the resistance of the coated substrate to mechanical and chemical deformations, which can cause the removal from that dried, solid coated substrate in terms area, were measured for that fundamental purpose. Also, for multicoating systems, as in that study the term of inter-coating adhesion force refers to the resistance of a heat-sealing lacquer coating layer from the bottom ink coating layer.

Table 1: Viscosity and Dilution Rates of Formulations with Common Solvents Used.

Formulation No	Initial Viscosity (F4, @ 20 °C)	%Dilution Rate with ETAC to V=18"	% Dilution Rate with ETOH to V=18"	% Dilution Rate with ETOH:Ethoxy Propanol (1:1) to V=18"
HSL1	26	12	9	11
HSL2	42	36	23	29
HSL3	13	0	0	0
HSL4	74	60	50	60
HSL5	45	35	33	35
HSL6 (Final formulation)	60	46	42	46

Table 1 shows initial viscosity values of studied and existing-conventional lacquers. There are also percent of dilution rates are tabulated with different solvents to adjust 18 seconds printing viscosity,

which is appropriate gravure printing. Final formulation HSL6 is compatible with all solvents as a good opportunity for variable applications.

3.2. Heat Sealing Strength

Heat-sealing strength was the other important parameter for this study. The sealing quality and integrity are essential requirements for final design of blister packaging. Evaluations of sealing strength and adequate final sealing property were done at first varnish's formulations with variable resin types.

All prepared drawdowns of ADHS varnishes, sealed with heat sealing device at conditions were 1 bar during 1 second, and 180 °C temperature as a condition 1 parameters. After heat-sealing process, the sealing strength measured in terms Newtons with Loyd device.

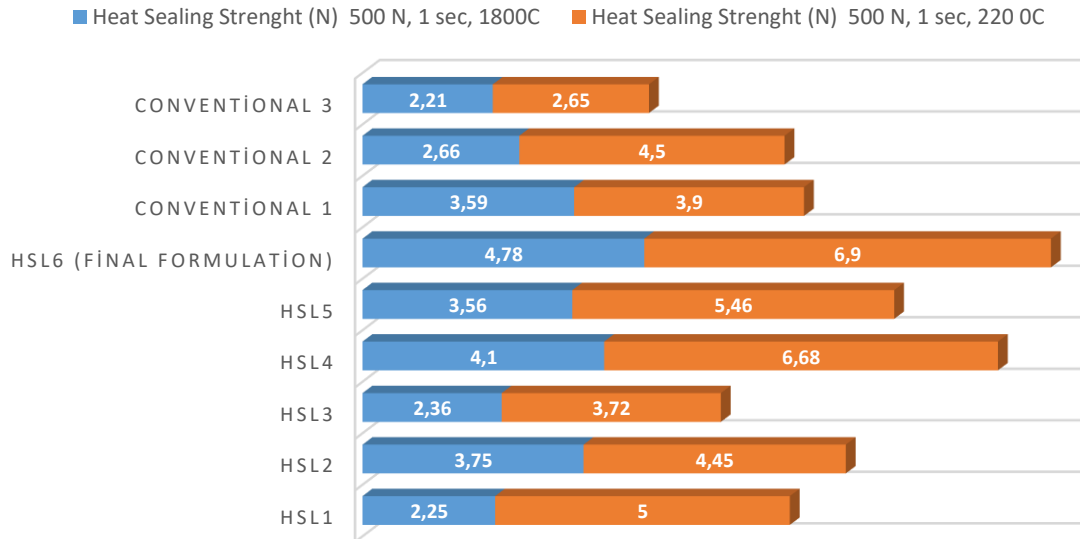


Figure 6: HS Strengths in Newton at sealing condition 1 and 2.

From Figure 6, it was seen that at both temperature conditions HSL 6 formulation has higher bond strength than other studied and existing

conventional heat seal lacquers. In addition, high temperature effect better bond strength was observed as expected.

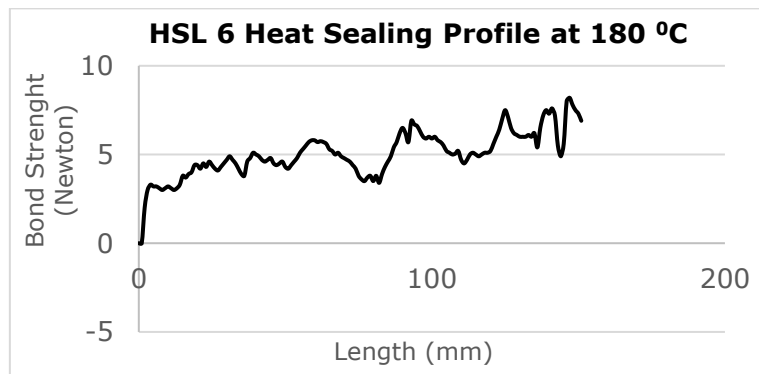


Figure 7: HSL 6 HS Profile at 180 °C.

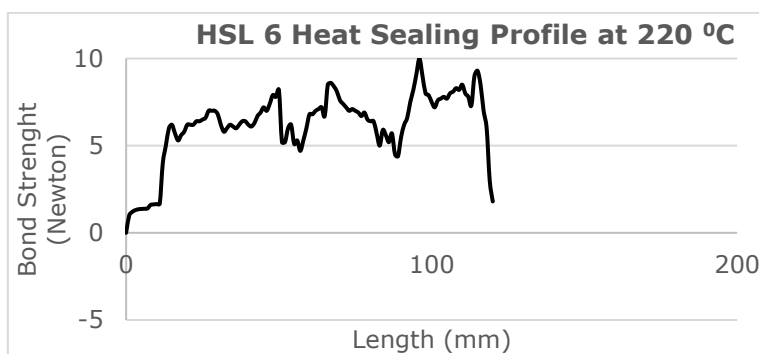


Figure 8: HSL 6 HS Profile at 220 °C.

In addition, Figure 7 and Figure 8 show the heat-sealing strength profile of HSL 6 at sealing condition 1 and condition 2. In figure's X-axis, the load results plotted on the graph in terms of newton and Y-axis shows the length of measured printed the strips with printed full structure of design. In Figure 8, film tearing was observed at 220°C temperature sealed strip, while measuring the sealing force with the device. Therefore, that indicates quite a high enough bond strength that tears the aluminum film.

3.3. Migration and Rub-Off Test Results

The migration and rub-off were the main issue for this study. With the currently used heat-sealing lacquer design, the ink, which applied to main surface, aluminum side of blister, migrates to the

secondary material (PET) surface. Because of that migration, the PET film was stained as seen below figure, which evaluated as one grade. Therefore, both surfaces of packaging are damaged by ink. Both surfaces cannot be recycled in this circumstance. Within the new design parameters, all ADHS varnishes were tested to find non-migratory resin types. Test results were rated between 1 and 5 scale by visual controls in Figure 9.

In results, grade 1 represents complete ink migration to PET side. Grade 5 represents the clear PET, no ink migration in Figure 9 after heat-sealing and cooling steps of prints. PET and aluminum were necessary to peel from each other. Then, PET film controlled for any removal, migration of ink.



Figure 9: Migration and Rub-Off on PET film.

3.4. Fourier Transform Infrared Spectroscopy (FTIR) Results

Migration and rub-off results were measured by FTIR for the HSL formulations. In FTIR tests, the peeled PET films after heat sealing and cooling processes were analyzed to be sure that there was no residual from the ink contamination, which indistinguishable by the visual tests on PET film side. FTIR analyses of four samples were performed with wave numbers between 4000 and 600 cm^{-1} on PET peeled film. Fourier Transform Infrared Spectroscopy was used to identify the surface of peeled PET film and neat PET film by using infrared light. Therefore, the result of FTIR analysis observed functional groups, characteristic peaks and impurities of the samples compared to neat, unprinted PET film. The sample results were interpreted as no migration when parallel to the scanned wavelength and peaks for the neat PET film surface. There were three trials done in that step as

an elimination of all laboratory test results. The below characteristics bands show these three peeled samples in red, blue, and green colors, respectively. In addition, the unprinted PET sample was represented in purple color. From the fingerprints of these four results, we can say that the green and purple peaks overlapped. The other two characteristics bands had represented different peak and small vibrations due to absorption increase and different chemicals migration from applied ink and HSL formulations of samples.

FTIR was used to check the efficiency of the final design HSL 6, so from the result of spectrum, the green colored transmittance bond shows the same functional groups present on neat PET film. The spectrum of transmittance bond of HSL 6 and pure PET film showed higher than 95 % similarities with their transmittance bond with same vibrations as seen Figure 10.

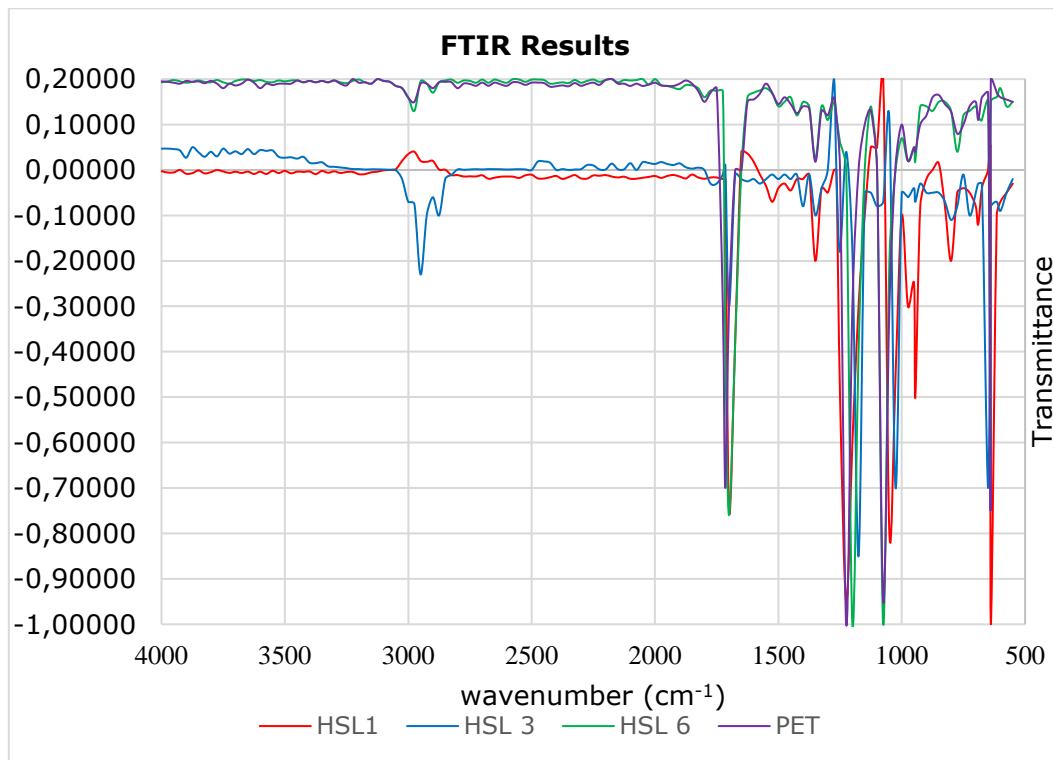


Figure 10: FTIR Result of HSL Formulations.

3.5. Coefficient of Friction (CoF) Control Results

Formulations HSL 5 and HSL 6 were tested to get the correct coefficient of friction levels to suit the printing process requirements. The amount and types of used wax particles were adjusted for this purpose. In addition, the conventional lacquers CoF values were compared to new design because of

their old industrial trials based on the positive feedback. As a target value, CoF set to between 0.25 and 0.50. Therefore, The CoF test results were shown in Table 2, HSL 6 formulation measured in the target value ranges and parallel results with respect to conventional lacquers in face-to-face and face to metal test methods with successfully.

Table 2: CoF Test Results.

Formulation No	COF	
	Face to Face	Face to Metal
HSL6	0.45	0.25
HSL5	1.92	1

3.6. Block Resistance Test Results

When printing processes on non-absorbent, flexible materials like aluminum, the designed lacquer with a strong adhesion, elasticity and sealing properties it is getting very hard to balance the drying and anti-blockage properties at the same time. The usage of appropriate wax compounds and additives to lacquer formulations gives positive effect also in terms of blocking properties as well as the tendency to migration, slip and scratching resistances (Leach at al., 1993). Furthermore, efficient drying

conditions controlled to ensure that applied lacquer set to avoid blocking issues in the printing process indispensably. Figure 11 shows block test result of HSL formulations at different conditions. From drawdowns it was seen that some block and migration problems on HSL 4. Some part of coated ink migrates to other side of aluminum film. In addition, increased test temperature caused more block and migration tendency for HSL 4. Therefore, the HSL 4 formulation was eliminated because of the block resistance test by visually.

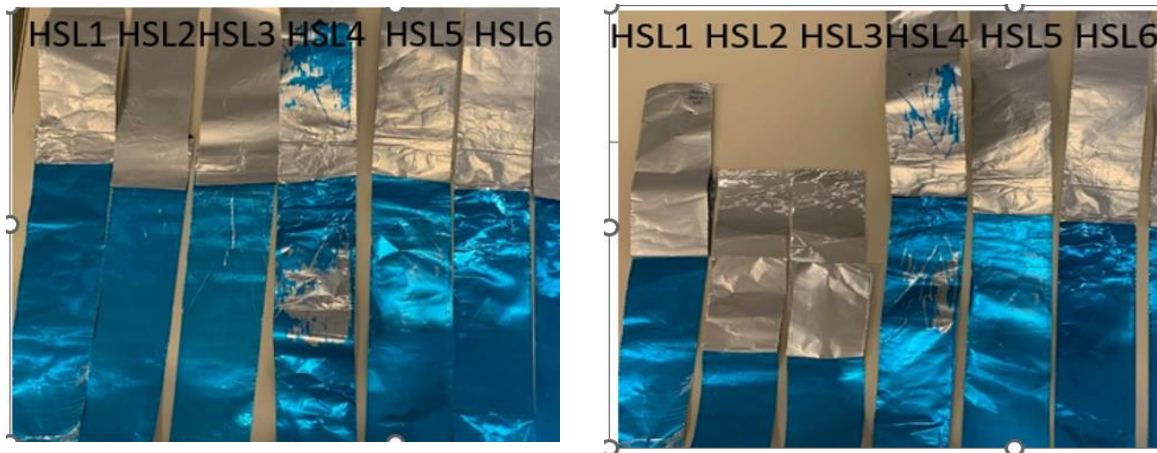


Figure 11: Block Test Result of Drawdowns at conditions 45 °C, 3 days, 45 kg & 20-25 °C, 1 week, 10 tons.

Table 3 was tabulated according to block formation of drawdowns under both test conditions. As seen table HSL 6 and conventional heat-sealing lacquers had been evaluated 0 which means no formation of

blocking. The aluminum film can be peeled off over the coating surface easily, Other HSL formulation could not passed this test.

Table 3: Numerical Block Test Results.

Block formation: 5 (high blocking) - 0 (no block formation)						
Conditions:	HSL 1	HSL 2	HSL 3	HSL 4	HSL 5	HSL 6
45°C, 3 days, 45 kg	2	0	0	5	2	0
20-25°C, 1 week, 10 tons	4	3	2	5	4	0

3.7. Solvent Retention Test Results

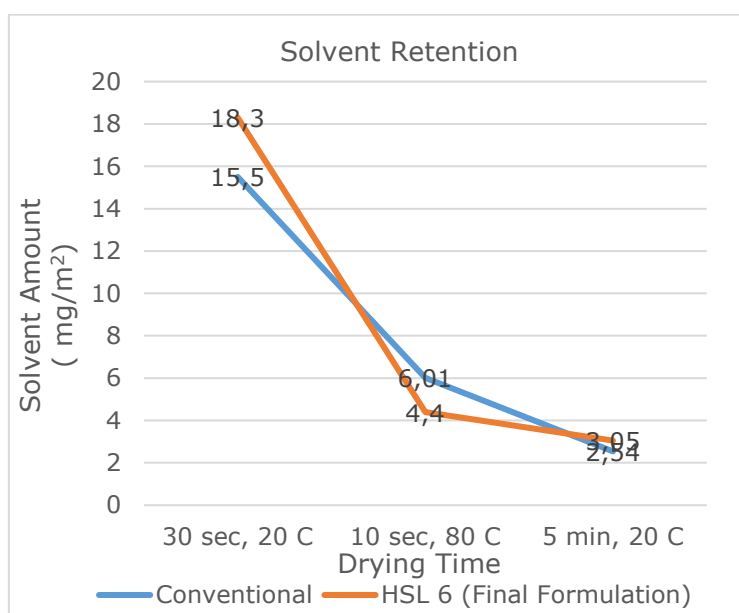
The presence of residual solvents in packaging changes the taste and odor of the finished products as the first to notice. Residual solvent prevents the packaging from closing by sealed securely. The formulation of lacquer designs is taken to ensure and tested in term of solvent release properties. In efficient drying or inappropriate resin and solvent selection in formulation structure cause blocking issues in the printed reels. The printed substrates that come in contact with food need to be controlled according to strict regulations and standards. Therefore, retained total solvents amount was limited with the 10 mg/m² for various converters as a threshold in food packaging. By nature of solvent-based lacquers, a gravure printed substrates still contains some amount of solvent after drying processes. When consideration is done for, the commonly used threshold values for residual

solvent amount the formulations to be compatible low-odor and solvent retention grades. Figure 12 shows the graphical representation of HSL 6 formulation and conventional heat-sealing lacquer in the interval of different drying conditions to understand the solvent retention profile of final prints. From the graph, we can understand that HSL 6 releases the solvent with a steeper acceleration and similarity in terms of drying and retention profile with conventional one. In addition, in Table 4 the total solvent residual amounts are shown in terms of mg/m².

New design HSL 6 show lower solvent residual amounts in certain drying conditions compared to industrial threshold for solvent residual at 10 sec., 80 °C and 5 min., 20 °C drying conditions which is lower values of currently used conventional heat-seal lacquer.

Table 4: Residual solvent amounts [mg/m²] for different drying conditions.

Drying Conditions	Conventional 1	HSL 6 (Final Formulation)
30 sec, 20 °C	15.5	18.3
10 sec, 80 °C	6.01	4.4
5 min, 20 °C	2.54	3.05

**Figure 12:** Residual solvent amounts [mg/m²].

4. CONCLUSION

The study dealt with the heat-sealing lacquer which has ink migration barrier property and applicable for direct food contact for Aluminum / PET Blister packaging to used resin and additive types in formulation. With the help of these selected components, finished packaging material PET film will be suitable for recycling. The heat-sealing lacquer to be designed has been provided thermal sealing and other technical properties in blister packaging applications as like as currently used conventional lacquers, which are not recyclable due to migration issue. Since the blister, packages made with the newly designed heat-sealing lacquer observed that prevents ink contamination to the PET film side.

Therefore, the PET film is suitable for use in recycling processes. Thus, the biggest consumed plastic waste of PET package is possible to use the obtained PET film by recycling as pure material source again when the new designed heat-sealing lacquer is used. In addition, recycled PET can be used as a resource again in raw material reserves.

Environmental pollution will be decreased; new environmental solutions will be presented to the packaging industry. Environmental protection and

economic saving can be done. According to laboratory tests and literature surveys, elastomeric PU was chosen as the main resin in the new design. Good sealing performance was achieved by using PVB resin with Elastomeric PU resin.

1- 5 % amount of CAB resin gives excellent anti-blocking and release property to heat-sealing lacquer formulation. On the other hand, it is experienced that adhesion promoter usage created migration tendency of ink to PET side.

1 - 3 % PE wax usage improved rub, mar, and abrasion resistance of final formulation also, decreased FTF CoF value from 1.92 to 0.45, which is suitable for printing process.

The new formulation has higher heat-sealing bond strength than existing conventional heat-sealing lacquers, which are not recyclable.

Therefore, according to that observation the factors of resin and additive selection on migration properties of heat-sealing lacquer for Aluminum / Pet Blister structure was completed successfully with the laboratory results and industrial trial.

In addition, another valuable output is this requirement carried out by using the resources of our country. The most importantly, the printed

blister packages with this new designed heat-sealing lacquer can now be recycled and gain re-value as a raw material and energy stock in comply with the circular economy plan.

5. CONFLICT OF INTEREST

The authors declare no conflict of interest.

6. ACKNOWLEDGMENTS

The authors would like to thank Sun Chemical Co. to their contribution for their help in laboratory tests and plant-site production trials.

7. REFERENCES

- Allen, K. W. (2010). A Critical Assessment of Factors Effecting Blister Pack Formation in the Pharmaceutical Industry. Loughborough University. Thesis. 293. <https://hdl.handle.net/2134/8509>
- Chaudhary, T. (2021). Blister Packaging Market Information by types (Carded Blister Packaging, Consumer Goods Blister Packaging, Clamshell, Blister Packaging), by applications (pharmaceuticals, food & beverages, consumer goods & others), by production methods (Thermoforming & Cold forming), by materials (PVC, PVDC, COC, Cold Form Foil and others), Forecast to 2030. Blister Packaging Market Report.110. <https://www.marketresearchfuture.com/reports/blister-packaging-market-1181>
- Ilhan,İ., Turan,D., Gibson,I.Klooster, R. T. (2021). Understanding the factors affecting the seal integrity in heatsealed flexible food packages. Packaging Technology and Science. 34(3), 14. <https://doi.org/10.1002/pts.2564>
- Lalpuria, M., Anantheswaran, R., & Floros, J. (2012). Packaging technologies and their role in food safety. In Microbial Decontamination in the Food Industry: Novel Methods and Applications. 703-733 Elsevier Ltd. <https://doi.org/10.1533/9780857095756.4.701>
- Leach, R.H.; Pierce, R.J. (1993). The Printing Ink Manual, Blueprint. Additives Handbook.(2011) By Dr. Joseph V. Koleske, Robert Springate and Dr. Darlene Brezinski.
- More V. (2020). PET Bottle Recycling Market Research Report Information by Recycling Process, Forecast till 2030, <https://www.marketresearchfuture.com/reports/PET-bottle-recycling-market-2865>
- Pudack, C., Stepanski, M., Fassler, P. (2020). PET Recycling – Contributions of Crystallization to Sustainability. Chemie Ingenieur Technik. 92, 452-458, <https://doi.org/10.1002/cite.201900085>
- Pinter, E., Welle, F., Mayrhofer, E., Pechhacker, A., Motloch, L. Lahme, V., Grant A., Tacker, M. (2021). Circularity Study on PET Bottle-To-Bottle Recycling. Sustainability.13, 7370, <https://doi.org/10.3390/su13137370>
- Ritchie, H. (2018). FAQs on Plastics. Our World in Data. <https://ourworldindata.org/faq-on-plastics>
- Turkchem. (2020). Waste PET Bottle Recycling Products, <https://www.turkchem.net/atik-pet-sise-geri-donusum-urunleri.html>
- Turkish Plastics Industrialist's Association (2020), <https://pagder.org/eng/haberdetay.php?id=210>



Solar Energy Driven Chemical Looping Air Separation

Y. Görkem Bak , Deniz Üner* 

¹Middle East Technical University, Chemical Engineering Department, Ankara, 06800, Türkiye

Abstract: Chemical looping is emerging as a feasible alternative to carry out reduction and oxidation processes under different process conditions. This technology proves especially useful when reduction and oxidation processes proceed with different time constants. With the possibility of incorporation of solar energy to the endothermic end of the process, chemical looping technology has recently become more popular. Chemical looping air separation (CLAS) is an alternative to cryogenic separation, by utilizing solar thermal energy. In this process a reducible metal oxide is heated to a temperature such that the metal releases its lattice oxygen. In the second step, the metal oxide is exposed to air and oxygen is captured by the oxide while pure nitrogen is released at the outlet and the loop is closed. Mn_2O_3 is selected as the oxygen carrier to perform chemical looping cycles. Oxygen mobility of the metal oxide and reversibility through redox cycles are tested with thermogravimetric analysis (TGA). The redox cycles are designed such that the air oxidizes, and the steam reduces the material. The reduction behavior of manganese (III) oxide under inert atmosphere is tested in TGA. It is proved that steam acts as an inert gas under the reaction conditions. The use of steam at the reduction stage results in a more convenient separation of the sweep gas (steam) from the oxygen released from the oxide. It is demonstrated that a redox cycle between Mn_2O_3 and Mn_3O_4 can be performed isothermally. The capability of the system to be coupled with solar energy makes it more alluring for environmentally friendly option seekers. The use of solar irradiation is tested with parabolic mirrors to observe the power output. Overall, CLAS process works on milder conditions which is crucial in reducing the energy and equipment costs, and its advantages regarding energy efficiency increase even more when solar energy is incorporated into the system.

Keywords: Chemical Looping Air Separation, Solar Energy, Sustainable Production

Submitted: December 13, 2013 . **Accepted:** February 06, 2024.

Cite this: Bak, Y. G., & Üner, D. (2024). Solar Energy Driven Chemical Looping Air Separation. Journal of the Turkish Chemical Society, Section B: Chemical Engineering, 7(1), 53–60. <https://doi.org/10.58692/jotcsb.1404612>.

*Corresponding author. E-mail: uner@metu.edu.tr.

1. INTRODUCTION

The importance of air separation arises from the necessity of supplying pure gases to chemical processes. Fresh air is almost 99% composed of nitrogen and oxygen, while the remaining is mainly argon along with some other noble gases and impurities. The details regarding the constituents of air can be seen in Table S.1 in the supplementary document. To the present day, the most successful method for air separation has been the cryogenic distillation of air, known as the air separation unit (ASU) in the chemical plants (Smith & Klosek, 2001). Cryogenic distillation proves effective in terms of providing excellent purity and achieving high production rates (Tesch et al., 2020). However, immense energy intensity associated with complexity of the liquefaction process and required

equipment make the cryogenic process unfavorable. In the cryogenic distillation, air is liquefied in a multi-step comprehensive process which includes compression, expansion, and heat exchangers leading to a limitation in thermodynamic second law efficiency to merely 25% (Krzystowczyk et al., 2021). On the other hand, CLAS is a self-contained air separation process working at atmospheric pressures and temperatures that can be achieved by focusing solar irradiation. According to a computational study performed by Li et. al., CLAS works on a specific energy consumption of 0.66 MJ/kg O_2 while conventional cryogenic distillation consumes 0.78 MJ/kg O_2 (Krzystowczyk et al., 2021). This implies a 15% decrease in energy consumption in the separation of air with further potential when it is coupled with solar energy.

Chemical looping air separation (CLAS) is an alternative to cryogenic separation, by utilizing solar thermal energy. In this process a reducible metal oxide is heated to a temperature where a lower oxidation state is more favorable, such that the metal oxide releases its lattice oxygen. In the second step, the metal oxide is exposed to air, and oxygen is captured by the oxide while pure nitrogen is released from the system and the loop is closed (Moghtaderi, 2010). The reactions for the proposed cycle are given below (K. Wang et al., 2013).

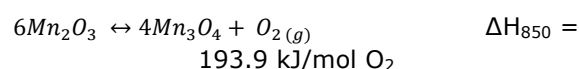


Although the pure and mixed metal oxides are evaluated in cyclic systems such as chemical looping oxygen uncoupling (CLOU) (Azimi et al., 2013; Shulman et al., 2011), and chemical looping combustion (CLC) (Abad et al., 2006; Adánez et al., 2018), CLAS seems to be the most sustainable solar energy storage method considering the product yield in the system (Bulfin et al., 2017). The simple design used in chemical looping air separation technology makes it more appealing for gas separation applications on a small scale (V. Shah et al., 2022). As a result of working at milder conditions and possible energy intensifications, its power consumption is lower than the conventionally used processes (Tao et al., 2022; K. Wang et al., 2016). Large scale applications of the CLAS process depend on selecting a convenient oxygen carrier and design of stable reactors that can withstand temperatures over 800 °C (Krzyszowczyk et al., 2021).

The most important aspects in the selection of the oxygen carrier are showing favorable reaction kinetics, transportation of oxygen with sufficient capacity, high mechanical and chemical resistance over repeated redox cycles, low cost, and environmental compliance. Manganese oxides in

this context are found sufficient to provide these effects in chemical looping air separation process by many researchers (K. Shah et al., 2012; Song et al., 2014; W. Wang et al., 2016; X. Wang et al., 2021). It is found that dual mixed and supported copper, cobalt, and manganese oxides can show promising results when performing redox cycles and to create a powerful alternative to cryogenic distillation (Moghtaderi, 2010). However, the performance of unsupported single metal oxides (especially Mn oxides) in the steam-air redox cycle is not investigated thoroughly in the literature.

At room temperature, the most stable form of manganese oxides is Mn_2O_3 which reduces to Mn_3O_4 at around 900 °C under air atmosphere. The reversible reaction of manganese oxides during the redox cycle is given as follows (Mattisson et al., 2009).



The reduction and oxidation of metal oxide can be triggered by inlet gas conditions in an isothermal process. Thus, energy and time saving in the process is improved by circumventing the time-consuming thermal transfer between the two steps of the cycle. The actual partial pressure of oxygen in the reaction chamber must be lower than its equilibrium value in order for the material to be stimulated to release oxygen to establish the equilibrium. Feed gas conditions for such stimulation include air at the oxidation step, and steam at the reduction step. Sweeping the oxygen in the reaction chamber with steam allows for a simple separation process of the product from the sweep gas. At a constant working temperature of 800-850 °C the material can be oxidized by air and reduced by steam. This method of pressure swing can facilitate the redox cycle by reducing the time needed to switch between reduction and oxidation, energy costs, and thermal stress on the material. The schematic of the proposed system is given in Figure 1.

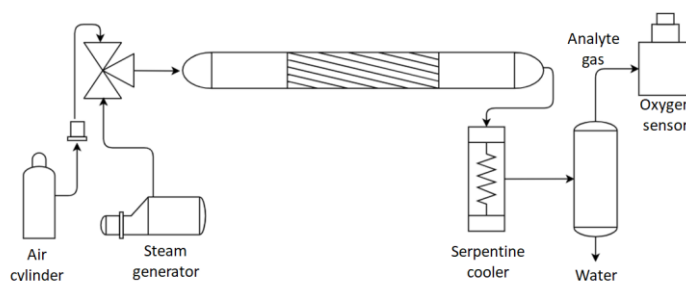


Figure 1: Chemical looping air separation experimental setup.

Coupling with solar energy will be accomplished by integrating the process into a parabolic mirror. These parabolic dishes are very successful in providing thermal energy with minimal losses since they directly concentrate the sun rays to the focal

point (Tescari et al., 2022). Reactor placement and focus adjustment are the crucial issues when coupling CLAS with solar energy (Khan et al., 2022; Patil et al., 2021). To utilize solar irradiation with

maximum efficiency, thermal losses should be minimized in the process.

2. EXPERIMENTAL SECTION

2.1. Materials

Manganese (II) oxide (MnO) is supplied from Aldrich Chemicals (99%, powder, -60 mesh). The material is used as is supplied commercially. Prior to the experiments, MnO is pre-oxidized under air flow.

2.2. Characterization

2.2.1. Thermogravimetric Analysis (TGA)

Thermal gravimetric analysis experiments are conducted with Shimadzu DTG-60H TG/DTA. The redox behavior of the material under dry air (99.9%, Oksan) flow is investigated with a temperature profile of 1 °C/min up to 1000 °C.

2.2.2. Cyclic TGA

To observe the reversibility of manganese oxides during the redox cycles, a cyclic analysis in TGA is performed. MnO is pre-oxidized to Mn₂O₃ and the cycle starts. Temperature ramp is altered throughout the experiment. Additionally, hold times are added to promote complete reduction and oxidation at the respective stage.

2.2.3. TGA Under Inert and Inert-Humidified Gas Conditions

To observe the effect of a non-oxidizing gas flow on the redox equilibrium, nitrogen gas (99.999%, Linde) is fed to the Mn₂O₃ in the analysis chamber. Temperature profile is 5 °C/min up to 950 °C.

To reveal the effect of water vapor, nitrogen is passed through a wash bottle before entering the analysis chamber of the thermogravimetric analyzer. The temperature of the water in the wash bottle is adjusted to observe the effect of partial pressure of water in reduction of manganese oxides. Temperature profile is the same as dry nitrogen reduction. Wash bottle temperature is adjusted to 25 °C and 50 °C.

2.2.4. Packed Bed Redox Cycle System

Manganese (II) oxide is filled into a quartz reactor and fixed by quartz wool. Length and overall diameter of the reactor are 600 mm and 12 mm respectively. Mass of MnO in the packing is 10 grams, corresponding to 0.14 moles. In the laboratory experiments, a homemade tubular oven is used to provide heat input to the system. Isothermal operation at 825 °C is conducted. Prior to

redox cycle, pre-oxidation of MnO to Mn₂O₃ is carried out. During the oxidation cycle, material in the packing is oxidized under airflow at 80 mL/min feed rate from the dry air cylinder. The consecutive reduction cycle is accomplished by feeding steam into the reactor from a homemade steam generator.

2.3. Instruments

2.3.1. Oxygen Sensor

A micro-fuel cell oxygen sensor module was procured from City Technologies company (model: CiTiceL AO2 Oxygen Sensor). Its circuit connections are assembled using an Arduino board and an additional ADS 1115 high-resolution analog-to-digital converter. For the measurement of oxygen concentration in a control volume, a polyamide block is carved, and a tee connection is built inside for the gas flow path and sensor junction. The block was carved such that the control volume was kept as small as possible to avoid a reduction in the sensitivity of the sensor along with an increase in response time.

2.3.2. Steam Generator

The steam generator used in the system is built from the boiler of an out-of-use steam iron. The electronic connection of the boiler is separated from the iron so that the boiler works as a standalone steam generator. Steam output is directed into the system through a hose connection coupled with stainless steel junction at the end. The maximum power of the steam generator is 1400 W.

3. RESULTS AND DISCUSSION

3.1. Thermogravimetric Analyses

3.1.1. Determination of The Working Capacity

The oxygen mobility on the material through the redox cycles can be screened via an observation over the mass of the oxygen carrier. Oxygen permeates through the lattice of manganese oxide until it reaches the saturation limit, so total mass of oxygen carrier is the main criterion that has influence on the overall capacity. The mass increase due to oxygen uptake for different phases of manganese oxides is given in Table 1. Calculation is based on stoichiometric reaction and mass balance, the details for the calculation can be found in supporting information document.

Table 1: Oxygen uptake of manganese oxides due to corresponding reactions.

Reaction	Oxygen Uptake (wt. %)
$3 \text{ MnO} + \frac{1}{2} \text{ O}_2 \rightarrow \text{ Mn}_3\text{O}_4$	7.52
$2 \text{ MnO} + \frac{1}{2} \text{ O}_2 \rightarrow \text{ Mn}_2\text{O}_3$	11.30
$\text{ MnO} + \frac{1}{2} \text{ O}_2 \rightarrow \text{ MnO}_2$	22.58

The calculation based on stoichiometric reactions will facilitate the comprehension of the materials phase conversion throughout the TGA experiments.

The result of thermogravimetric analysis to determine the working capacity is given in Figure 2.

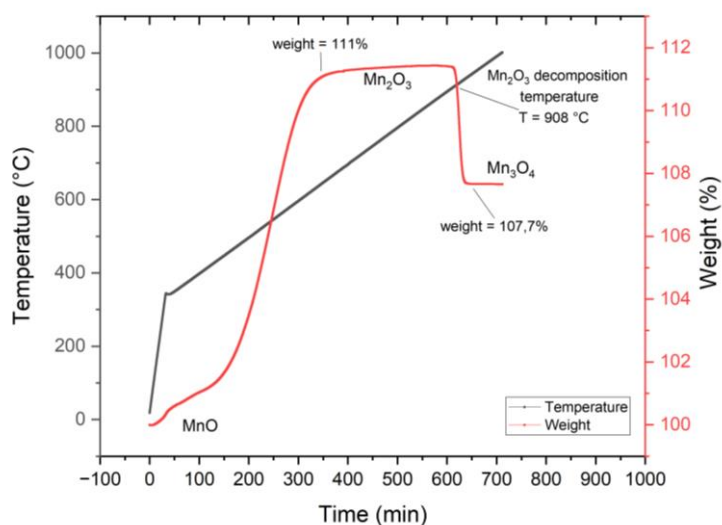


Figure 2: Thermogravimetric analysis for observation on working time capacity of manganese oxides.

Results obtained from TGA indicate that the weight change of the material complies with reaction stoichiometries as well as shift point temperatures dictated by thermodynamic limits. It is seen that the material is oxidized from rocksalt manganese (II) oxide to bixbyite (Mn_2O_3) up to a certain saturation level and the rate of oxidation then slows down. Oxidation occurs over a wide range of temperatures relying on the chemical kinetics stimulated by the increase in temperature while reduction to hausmannite (Mn_3O_4) is sharp and distinct driven by the thermodynamic limit that lies around 900 °C.

3.1.2. Reversible Interaction with Oxygen

When performing redox cycles with manganese oxides, it is possible to utilize temperature adjustments to induce the material to oxidize or reduce. Metal oxides usually prefer to be at a higher

oxidation state at lower temperatures, holding a greater amount of oxygen in their lattice. As the temperature goes up, the oxygen carrier tends to release oxygen driven by thermodynamic phase equilibrium. The crucial parameter is the reversibility of the material between reduced and oxidized phases over consecutive cycles. Manganese oxide is tested in a cyclic temperature profile to observe its reversible interaction with oxygen as well as if a change in the capacity occurs over successive cycles. Different heating rates, temperature intervals, and hold times are used to interactively reduce or oxidize the material when necessary. The results regarding the TGA for temperature induced redox cycle are given in Figure 3.

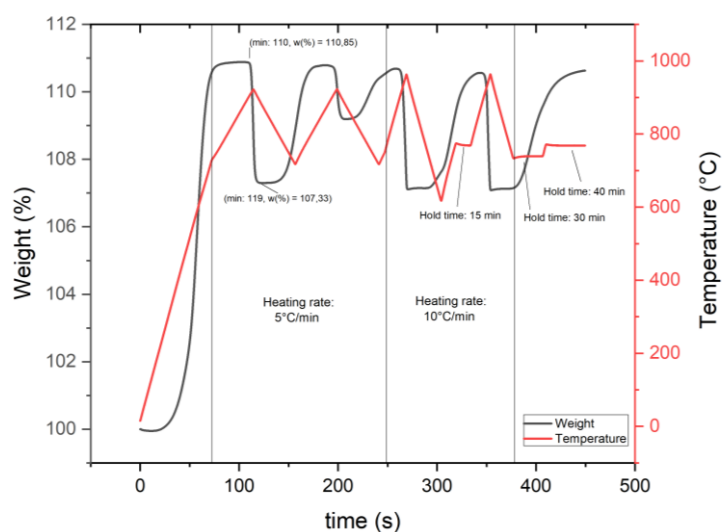


Figure 3: TGA cyclic temperature profile with manganese oxide.

3.1.3. Effect of Inert Atmosphere and Steam on Reduction

Previously oxidized manganese (II) oxide samples are reduced under the flow of dry and humidified N₂. Oxidation is performed up to the Mn₂O₃ phase. Humidification in the reduction stage is carried out

via wash bottles at 25 °C and 50 °C. The results are shown in Figure 4. It should be noted that prior to all reduction experiments, the material was oxidized to Mn₂O₃ as indicated by weight increase in TGA and the profiles were identical.

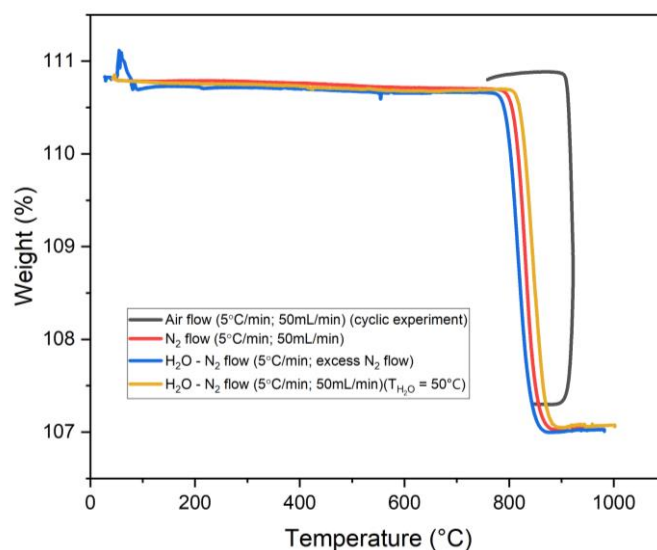


Figure 4: Mn₂O₃ reduction profiles under different gas flow conditions.

It can be seen from the profiles that reduction under an inert atmosphere has resulted in a decrease in the reduction temperature to around 800 °C. Effect of inert and humidified gas conditions did not show great significance on the redox equilibria. It is demonstrated that water vapor acts as an inert gas at the reaction conditions and has a reducing effect on the material by sweeping the released oxygen from the reaction chamber.

3.2. Packed Bed Redox Cycle

The performance of manganese oxide packing in chemical looping air separation is tested by an oxidation step with air feed and a reduction step feeding steam into the reactor. The oxygen concentration in the output gas is monitored using a micro-fuel cell oxygen sensor. In the first step, starting material MnO is oxidized to Mn₂O₃ with a temperature profile of 5 °C/min up to 850 °C under dry air feed at 80 mL/min. The results of the output gas concentration and the temperature profile in preliminary oxidation are given in Figure 5.

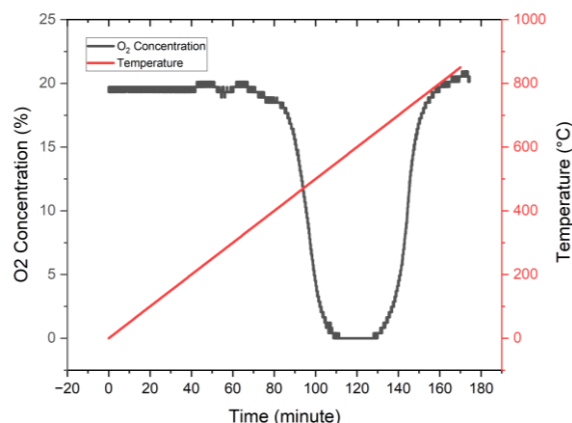


Figure 5: The oxygen concentration of the output gas and temperature profile during the oxidation of MnO to Mn₂O₃.

The result given in Figure 5 is an investigation on the output gas concentration when temperature programmed oxidation of MnO is carried out. From

the O₂ concentration results, it is seen that a gradual decrease in the beginning occurs due to the limitation in oxidation kinetics. With the increase in

the temperature, oxidation rate also increases, and all the incoming oxygen molecules are reacted with metal oxide packing, allowing for pure nitrogen production at the outlet. Total amount of oxygen that is absorbed is found to be 0.034 mol by the curve area which agrees well with the reaction stoichiometry. The details for the curve area calculation can be found in the supplementary document.

For the cyclic experiments, gas condition varied after the pre-oxidation of the material and a redox

cycle between Mn_2O_3 and Mn_3O_4 is performed. When the saturation of the material for oxygen is established as indicated by the equilibration of oxygen profile in the sensor, inlet gas is switched to steam to favor reduction of the metal oxide. Then, the gas condition is switched to air to re-oxidize the material, completing the cycle. The process is conducted isothermally at 825 °C. The result regarding the oxygen concentration profile during the redox cycle experiment is given in Figure 6.

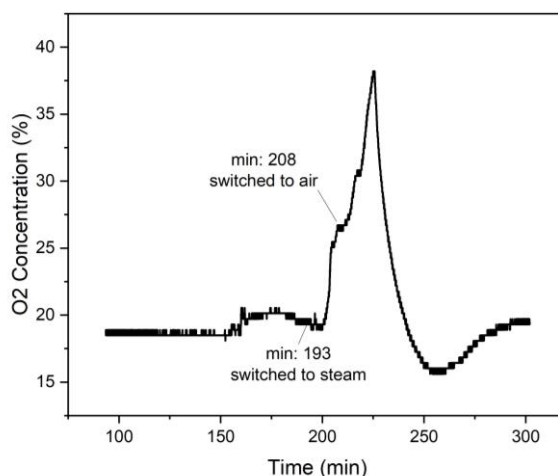


Figure 6: Oxygen concentration profile during redox cycle.

Steam flow started at a certain point for a 15-minute time interval. Due to the condensation units assembled after the reactor, steam condensed and did not sweep the oxygen gas further. Therefore, inlet gas condition is changed to air and a further sweep of the released oxygen is achieved. However, this caused simultaneous oxidation of the metal oxide bed that was oxygen deficit after a 15-min steam period.

The oxygen mobility on the material can be calculated by the peak area in the oxygen molar flow rate with respect to time plots. The procedure for the calculation of peak areas is given in supporting information. The results indicate that 0.0085 mol of oxygen is released during the reduction step. At the reoxidation step, 0.0053 mol

of oxygen is incorporated into the structure. Even if any simultaneous oxidation of the material is ignored, the oxygen release corresponds to 70 percent of the maximum capacity.

3.3. Parabolic Dish Power Measurements

The power output that can be obtained from a parabolic dish is tested with a 0.7 m diameter parabolic mirror. A water vessel with dimensions of 5 cm height and 2.5 cm diameter is insulated with a cordierite block and placed at the center of the focal point. A thermocouple is inserted in the water mass and the actual temperature is observed throughout the experiment. The resulting temperature profile is given in Figure 7.

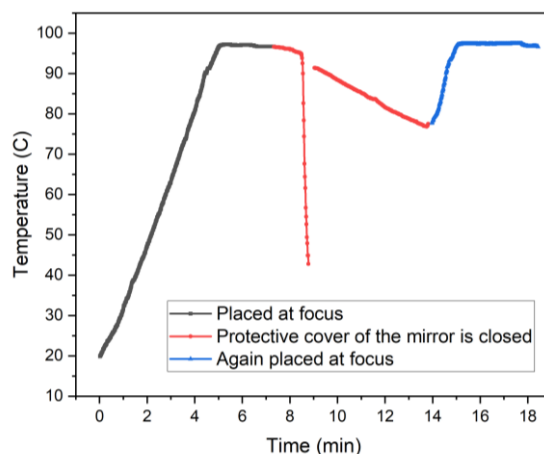


Figure 7: The temperature profile of water heated with parabolic mirror.

The power input is calculated as given in supplementary information with the help of the definite temperature ramp and known water mass. It is found that the parabolic mirror has provided the focus with 100 W of power. Considering that the solar energy available at the time of the experiment was 152 W, an irradiation efficiency of around 66% is achieved in the insulation system. The details of the calculation for the energy obtained with solar irradiation are given in supplementary information.

4. CONCLUSION

Within the scope of the study, a unique reactor system is designed and constructed to perform redox cycles and test metal oxides for their performance in CLAS. The designed system led to the production of pure nitrogen at the outlet stream during the oxidation stage, and the production of oxygen at the reduction stage. The redox cycle is kept between Mn_2O_3 and Mn_3O_4 phases of manganese oxides. This is achieved by feeding air to oxidize, and steam to reduce the material at a constant temperature. The peak area calculations indicate that 0.034 mol oxygen is used in total throughout the oxidation of 10 g of manganese (II) oxide, which agrees well with the stoichiometric calculations. Considering that the redox cycle is performed between Mn_2O_3 and Mn_3O_4 , the capacity is 0.012 mol O_2 per cycle, 10 g of oxide basis. The volume equivalent of this value results in a cycle capacity of 30 mL of O_2 and 110 mL of N_2 per gram of metal oxide. Moreover, the redox cycle experiments have revealed that at least 70 percent reduction is achieved under steam flow. However, since air is fed midway to reduction, simultaneous oxidation occurs while sweeping. Material re-oxidizes very slowly in the consecutive step since the condensation of water in the pipeline and wetted packing material cause an additional mass transfer, blocking the oxygen to penetrate through the lattice of the metal oxide. The use of superheated steam could be the solution to prevent this issue.

The possible practical applications of CLAS in the industry rely on studies that aim to discover

optimum operating conditions and materials that exhibit more favorable properties for the process. Since the CLAS allows the air separation process to be performed at a much smaller scale and under milder conditions, it is the most viable option for distributed plants that operate on renewable energy. Not only does it prove successful by opening a path where solar energy can be utilized to perform air separation, but it also offers advantages in terms of decreasing the specific energy consumption and reducing the fabrication costs for equipment.

5. ACKNOWLEDGMENTS

State Oil Company of Azerbaijan Republic (SOCAR) is acknowledged for their partial financial support through the project code ODTU TTO GC-009-2022.

6. REFERENCES

- Abad, A., Mattisson, T., Lyngfelt, A., & Rydén, M. (2006). Chemical-looping combustion in a 300 W continuously operating reactor system using a manganese-based oxygen carrier. *Fuel*, 85(9), 1174–1185. <https://doi.org/10.1016/j.fuel.2005.11.014>
- Adánez, J., Abad, A., Mendiara, T., Gayán, P., de Diego, L. F., & García-Labiano, F. (2018). Chemical looping combustion of solid fuels. In *Progress in Energy and Combustion Science* (Vol. 65, pp. 6–66). Elsevier Ltd. <https://doi.org/10.1016/j.peccs.2017.07.005>
- Azimi, G., Leion, H., Rydén, M., Mattisson, T., & Lyngfelt, A. (2013). Investigation of different Mn-Fe oxides as oxygen carrier for chemical-looping with oxygen uncoupling (CLOU). *Energy and Fuels*, 27(1), 367–377. <https://doi.org/10.1021/ef301120r>
- Bulfin, B., Vieten, J., Agrafiotis, C., Roeb, M., & Sattler, C. (2017). Applications and limitations of two step metal oxide thermochemical redox cycles; A review. In *Journal of Materials Chemistry A* (Vol. 5, Issue 36, pp. 18951–18966). Royal Society of Chemistry. <https://doi.org/10.1039/c7ta05025a>

- Khan, M. I., Asfand, F., & Al-Ghamdi, S. G. (2022). Progress in research and technological advancements of thermal energy storage systems for concentrated solar power. In *Journal of Energy Storage* (Vol. 55). Elsevier Ltd. <https://doi.org/10.1016/j.est.2022.105860>
- Krzystowczyk, E., Haribal, V., Dou, J., & Li, F. (2021). Chemical Looping Air Separation Using a Perovskite-Based Oxygen Sorbent: System Design and Process Analysis. *ACS Sustainable Chemistry and Engineering*, 9(36), 12185–12195. <https://doi.org/10.1021/acssuschemeng.1c03612>
- Mattisson, T., Lyngfelt, A., & Leion, H. (2009). Chemical-looping with oxygen uncoupling for combustion of solid fuels. *International Journal of Greenhouse Gas Control*, 3(1), 11–19. <https://doi.org/10.1016/j.ijggc.2008.06.002>
- Moghtaderi, B. (2010). Application of chemical looping concept for air separation at high temperatures. *Energy and Fuels*, 24(1), 190–198. <https://doi.org/10.1021/ef900553j>
- Patil, V. R., Kiener, F., Grylka, A., & Steinfeld, A. (2021). Experimental testing of a solar air cavity-receiver with reticulated porous ceramic absorbers for thermal processing at above 1000 °C. *Solar Energy*, 214, 72–85. <https://doi.org/10.1016/j.solener.2020.11.045>
- Shah, K., Moghtaderi, B., & Wall, T. (2012). Selection of suitable oxygen carriers for chemical looping air separation: A thermodynamic approach. *Energy and Fuels*, 26(4), 2038–2045. <https://doi.org/10.1021/ef300132c>
- Shah, V., Jangam, K., Joshi, A., Mohapatra, P., Falascino, E., & Fan, L. (2022). The Role of Chemical Looping in Industrial Gas Separation. In *Sustainable Separation Engineering* (pp. 199–237). Wiley. <https://doi.org/10.1002/9781119740117.ch5>
- Shulman, A., Cleverstam, E., Mattisson, T., & Lyngfelt, A. (2011). Chemical - Looping with oxygen uncoupling using Mn/Mg-based oxygen carriers - Oxygen release and reactivity with methane. *Fuel*, 90(3), 941–950. <https://doi.org/10.1016/j.fuel.2010.11.044>
- Smith, A. R., & Klosek, J. (2001). A review of air separation technologies and their integration with energy conversion processes. In *Fuel Processing Technology* (Vol. 70). www.elsevier.com/locate/proc
- Song, H., Shah, K., Doroodchi, E., Wall, T., & Moghtaderi, B. (2014). Reactivity of Al₂O₃- or SiO₂-Supported Cu-, Mn-, and Co-based oxygen carriers for chemical looping air separation. *Energy and Fuels*, 28(2), 1284–1294. <https://doi.org/10.1021/ef402268t>
- Tao, Y., Tian, W., Kong, L., Sun, S., & Fan, C. (2022). Energy, exergy, economic, environmental (4E) and dynamic analysis based global optimization of chemical looping air separation for oxygen and power co-production. *Energy*, 261. <https://doi.org/10.1016/j.energy.2022.125365>
- Tescari, S., Neumann, N. C., Sundarraj, P., Moumin, G., Rincon Duarte, J. P., Linder, M., & Roeb, M. (2022). Storing solar energy in continuously moving redox particles – Experimental analysis of charging and discharging reactors. *Applied Energy*, 308. <https://doi.org/10.1016/j.apenergy.2021.118271>
- Tesch, S., Morosuk, T., & Tsatsaronis, G. (2020). Comparative Evaluation of Cryogenic Air Separation Units from the Exergetic and Economic Points of View. In *Low-temperature Technologies*. IntechOpen. <https://doi.org/10.5772/intechopen.85765>
- Wang, K., Yu, Q., Hou, L., Zuo, Z., Qin, Q., & Ren, H. (2016). Simulation and energy consumption analysis of chemical looping air separation system on Aspen Plus. *Journal of Thermal Analysis and Calorimetry*, 124(3), 1555–1560. <https://doi.org/10.1007/s10973-016-5237-9>
- Wang, K., Yu, Q., & Qin, Q. (2013). The thermodynamic method for selecting oxygen carriers used for chemical looping air separation. *Journal of Thermal Analysis and Calorimetry*, 112(2), 747–753. <https://doi.org/10.1007/s10973-012-2596-8>
- Wang, W., Zhang, B., Wang, G., & Li, Y. (2016). O₂ release of Mn-based oxygen carrier for chemical looping air separation (CLAS): An insight into kinetic studies. *Aerosol and Air Quality Research*, 16(2), 453–463. <https://doi.org/10.4209/aaqr.2014.07.0140>
- Wang, X., Shao, Y., & Jin, B. (2021). Thermodynamic evaluation and modelling of an auto-thermal hybrid system of chemical looping combustion and air separation for power generation coupling with CO₂ cycles. *Energy*, 236. <https://doi.org/10.1016/j.energy.2021.121431>



Amorphous Silica Production from Serpentine and its Techno-Economic Analysis

Yalçın ÇAKAN,¹  Mehmet GÖNEN*² 

¹Betek Boya ve Kimya San. A.Ş., Gebze Organize Sanayi Bölgesi, 3200.Sokak No:3206 Gebze/Kocaeli, Türkiye

²Süleyman Demirel University, Department of Chemical Engineering, Batı Yerleşkesi, E13 Blok Çünür/Isparta, Türkiye

Abstract: The production of silica from the reaction of serpentine mineral with sulfuric acid has been investigated. Silica production process was developed by using optimum parameters of 67.3 °C temperature, 4.8 M acid concentration and 57.1 min. reaction time. Techno-economic analysis of the silica production process was made using a SuperPro Designer software (Version 9.0). Simulation has been performed for different annual plant capacities between 4,000 t and 16,000 t. The optimum production cost of silica was obtained for an annual plant capacity of 12,000 t. The total capital investment and operating costs for silica production facility designed was calculated as US\$40,247.000 and US\$4.24/kg, respectively. The payback period of the facility investment was determined as 4.8 years. The tailing waste of chrome ore could be used as raw material to produce silica and magnesium sulfate in an economic way.

Keywords: Amorphous Silica, Serpentine, Optimization, SuperPro Designer, Techno- Economic Analysis

Submitted: February 11, 2024. **Accepted:** February 28, 2024.

Cite this: Çakan, Y., & Gönen, M. (2024). Amorphous Silica Production from Serpentine and its Techno-Economic Analysis. Journal of the Turkish Chemical Society, Section B: Chemical Engineering, 7(1), 61–68. <https://doi.org/10.58692/jotcsb.1435352>.

*Corresponding author. E-mail: mehmetgonen@sdu.edu.tr.

1. INTRODUCTION

Serpentine is a general name used for minerals having the structure of magnesium hydrated silicates. The general composition of those minerals is as following: $Mg_{3-x}(M)_xSi_{2-y}(T)_yO_5(OH)_4$, where the site M could be Mg^{2+} , Fe^{2+} , Fe^{3+} , Al^{3+} , Ni^{2+} , Mn^{2+} , Zn^{2+} and the site T by Si^{4+} , Al^{3+} , Fe^{3+} (Carmignano et al., 2020). The structural configuration of serpentine is shown in Figure 1. It is a layer with a thickness of 0.72 nm in which the Mg trioctahedral sheet $[MgO_2(OH)_4]^{6-}$ is linked to the tetrahedral silicate sheet $[Si_2O_5]^{2-}$ (Carmignano et al., 2020; Fedoročková et al. 2014).

Serpentine is found as chrysotile, lizardite and antigorite in nature. But their crystal structures are different from each other. Serpentine could transparent, white, grey and sometimes green tones, yellow and rose pink in colors. The most widely found serpentine mineral is chrysotile. Although lizardite, antigorite, and chrysotile have the similar chemical composition, serpentines have different layered structures ended up fibrous chrysotile, lamellar agglomerated antigorite and lizardite elongated mineral particles (Zhou et al., 2017; Pietrikova et al., 2004). Serpentine is usually used in specific paint production, fire prevention, paper coating, and vehicle brake systems.

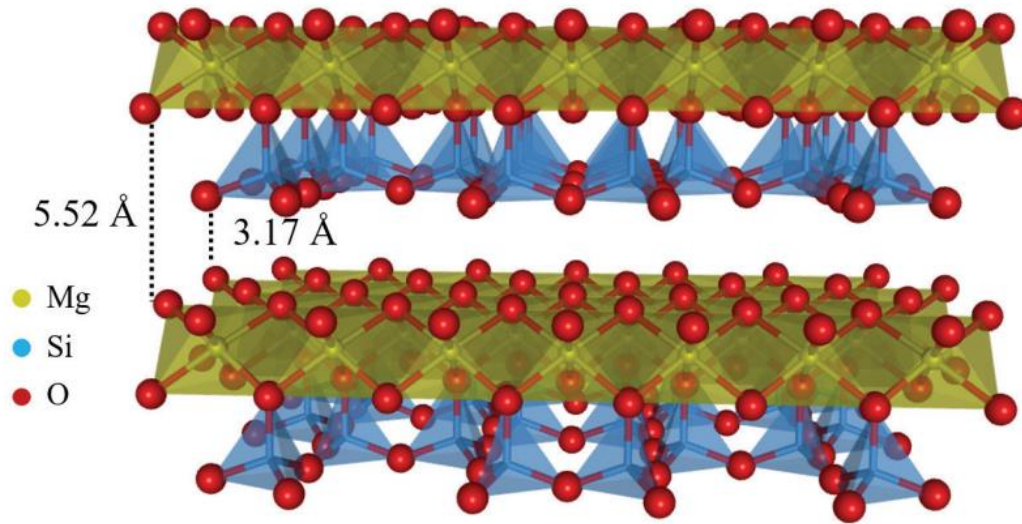
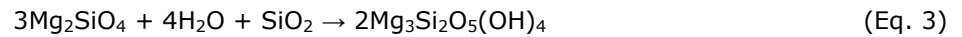


Figure 1. Basic structure of serpentine mineral (Carmignano et al., 2020).

Serpentine minerals are formed by the hydration of olivine minerals which are known as forsterite and fayalite (Mg^{2+} , Fe^{2+}) $_2\text{SiO}_4$ as given in Eqn. 1 to 3. Carbonates and hydroxide are formed as by-products in the following equations (Çevik, 2006). The quality

of dunite mineral is greatly affected during the serpentine formation. The weakened mineral structure enables the dissolution of the mineral in leaching.



Serpentine a silicate mineral which has rich in magnesium and silicon. The structure of serpentine having 35-40%wt. MgO, 30-35%wt. SiO_2 and 15-20%wt. H_2O . However, it has trace amounts of Fe, Al, Ca, Cr, and Ni. Serpentine mineral consists of silicate layers which are connected to magnesium hydroxide $\text{Mg}(\text{OH})_2$ by weak ionic bonds (Fedoročková et al., 2014). Serpentine minerals are easily dissolved due to the presence of these ionic bonds. Serpentine minerals are formed as concentrated waste of chromium production plant in Türkiye. The abundance of serpentine in Earth's crust makes it is cheap and accessible.

precipitated silica is US\$ 3.8 Bn in 2022 and estimated to increase with rate of 4.4% from 2023 to 2031 (Global Industry Report, 2023). The important producers of silica in the world are Evonik Industries, PPG Industries, Wacker Chemie AG, AkzoNobel N.V., Tosoh Corporation, Cabot Corporation, and Solvay SA.

Silicon is the second most abundant element which are found as compounds after oxygen. The 25.7% of earth crust consist of silicon compounds (Norton, 1993). SiO_2 , silicon dioxide, or widely known as silicate in industry make bond with metals (magnesium, aluminum, calcium and iron) to form magmatic and metamorphic rocks and silicate minerals (Flörke et al., 2000). Silica has many polymorphic structures such as crystalline silica, amorphous silica and synthetic amorphous silica. Crystalline silica can be found in nature as silicone dioxide and the most encountered type is quartz. Amorphous silica means that it has no crystalline unit in its structure. Synthetic amorphous silica can be produced via different techniques from silica sources. The use of synthetic amorphous silica has been increasing each year in the world. The global industry analysis reported that the worldwide demand for

Hereinafter, the term "silica" will be used instead of "amorphous precipitated silica" in the text. Silica is a white powder having the density of 1.9-2.2 $\text{g}\cdot\text{cm}^{-3}$. It has SiO_2 content of 95%wt or greater. The surface of area of silica varies between 50-400 $\text{m}^2\cdot\text{g}^{-1}$ which enables it to be used as filling materials (Florke et al., 2000). Silica produced is named according to the specific technique utilized, such as precipitated silica and pyrogenic silica (Lazaro et al., 2012). There are two main methods utilized in silica production: wet method and thermal technique. Pyrogenic silica is obtained in the gas phase reaction of tetrachlorosilane and hydrogen at an elevated temperature. HCl gas formed as by-product is separated by adsorption from the process to be reused in the production of SiCl_4 (Flörke et al., 2000). Wet method consists of two steps: first steps is the synthesis of sodium silicate solution via the reaction between olivine and NaOH/KOH at high pressure and temperature (120-200 °C) in an autoclave and the second step is the reaction of sodium silicate with acidic solution to give precipitated silica as product (Raza et al., 2018). Commercially sodium silicate known as water glass is directly used in silica

production. When the process is evaluated overall, due to the high energy consumption and CO₂ emissions it is not sustainable and environmentally friendly.

Precipitated silica can also be produced from natural silicate minerals like olivine, serpentine using the wet process. The production of precipitated silica from olivine mineral was studied by Lazaro and his co-workers (Lazaro et al., 2019). Olivine mineral having particle size range of 0.1-0.5 mm and of 0.2-1.2 mm was dissolved by using 3 M H₂SO₄ at 50 °C for 24 h. A high quality ordered mesoporous silica production in a one-step synthesis with the use a micellar liquid crystal prepared from the non-ionic surfactant Triton X-100 was investigated. The produced mesoporous silica has the surface area up to 1000 m²/g and narrow pore size distributions around 2-4 nm (Lazaro et al., 2019). The production of Mg(OH)₂ and MgO was investigated using serpentine mineral (Ballhorn and Franke, 1996). As the serpentine has less stable structure, it is easily digested by acids. The reaction between serpentine and sulfuric acid produces precipitated silica and sulfate salts as by-products depending on the impurity content of the mineral.

Silicic acid is initially formed in an aqueous phase during acid dissolution of silicate minerals. Silicic acid monomers form oligomers and polymerize to form larger units at certain conditions pointed by Iler (1979). Silicic acid can be produced in both acidic and basic solutions. In acidic medium, viscosity of the mixture increases depending on polymerization degree of Si(OH)₄ units. Aggregation and flocculation occur in an acidic medium regardless of charge balance. As the reaction progresses, released SiO₂ from mineral structure hydrolyzes to form silica polymeric units and silica gels. In the production of silica from minerals by using acids, product should be separated from the reaction media as soon as possible to prevent the gel formation. Recovery of Mg from H₂SO₄ leaching solution of serpentine was studied Chen and his coworkers (2023). Fe³⁺, Al³⁺, and Cr³⁺ in solution were precipitated increasing pH to 4 by adding MgO. After this step, 6 g/L Na₂S solution was added to the filtrate and reacted for 1.0 h to remove Ni²⁺, Co²⁺, and Mn²⁺ in the form of NiS, MnS, and CoS, respectively. Finally, diluted solution was mixed with ammonia to precipitate Mg(OH)₂ at a temperature range of 40-70 °C; and the pregnant solution was further mixed with NH₄HCO₃ to precipitate (4 MgCO₃.Mg(OH)₂.4H₂O). The purity of Mg(OH)₂ was reported as 98.48% (Chen et al., 2023).

Production of potassium-magnesium chloride from the chromite ores concentration plant tailings was studied in the literature. Chromite ores concentration plant tailings used as Mg source was firstly threatened by wet magnetic separation. Concentrated raw material was dissolved by using concentrated HCl to produce magnesium chloride and amorphous silica. The purity of amorphous silica was reported as 95.75%wt. To produce purer magnesium chloride, Mg(OH)₂ was added into solution to increase pH so that impurities can precipitate. Finally, KOH

was added stoichiometrically into the purified MgCl₂ solution at 90 °C to produce carnallite (Top and Yıldırım, 2017). In most of the studies in literature, temperature, acid type, acid concentration and reaction time have been investigated and optimized (Pietriková et.al., 2004; Çiftçi et al., 2020). There is no information about the techno-economic analysis of the developed process.

SuperPro Designer is a software which enables the modelling and simulation of the developed process to determine its feasibility. The process can be designed either in batch or continuous mode. The required data e.g. physical and chemical properties of raw materials and products, economic parameters, reaction parameters and utilities for the process can be selected from its database if available, or experimentally obtained from lab studies and from the market. After designing the process, mass and energy balances are calculated simulations are performed. The feasibility of boric acid production from colemanite mineral was investigated by using SuperPro Designer. The fixed capital investment and annual operating costs of the boric acid plant are calculated as US\$170.7 M and US\$70.1 M/y, respectively, for a 100 kt/y capacity. Boric acid production cost with the impurity of <100 ppm was calculated as US\$0.70 kg⁻¹. A 6.3 years of payback time was estimated for the developed process considering environmental effects (Gönen et al., 2022).

The feasibility analysis for silica (SiO₂) production from the reaction of serpentine mineral and sulfuric acid has been aimed in this study. Silica production process was formed in SuperPro Designer software, version 9.0 (Intelligent Inc., USA). Mass and energy balances were made for the developed process for different plant capacities. Payback periods (PBP) for those capacities were estimated from the simulation results.

2. EXPERIMENTAL SECTION

2.1. Materials

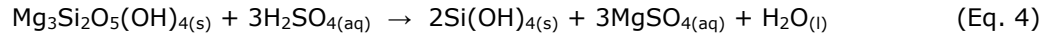
Serpentine mineral is an inert powder formed as a waste from the processing of chromite ores concentration plant tailings in Bursa, Türkiye. The serpentine mineral used in the experiments was supplied as -150 µm from Hayri Ögelman Inc. In the experiments, sulfuric acid was used to digest the serpentine mineral to produce an amorphous silica. The sulfuric acid used in the experiments is 98%wt. Chemical analysis of the serpentine mineral used in the experiments was carried out using X-Ray Fluorescence.

2.2. Methods

In the production of silica from the reaction of serpentine mineral with sulfuric acid, solid/liquid ratio: 10%, stirring rate: 1000 rpm and particle size of serpentine mineral: -150 µm were kept constant. Temperature range of 50-70-90 °C, the acid concentration of 3.0-4.0-5.0 M and the reaction time of 20-40-60 min. were chosen as experimental parameters and optimized in the previous study

(Çakan and Gönen, 2022). Those optimized parameters were used in the process design and development in SuperPro Designer program. The heterogenous reaction between serpentine and

sulfuric acid in an aqueous phase was carried out in a stirred glass reactor as given in Eq. 4.



The solid phase formed in the reaction was silica and the liquid phase containing the magnesium sulfate. Vacuum filtration method was used to separate the solid phase from the solution. The amorphous silica obtained in the filtration was washed with distilled water to purify and dried in an oven at 105 °C. X-Ray Fluorescence analysis was performed for determining the chemical composition of silica. FTIR analysis was performed for the bond structure of silica. Conversion in the reaction was determined by using the Mg concentration measured by ICP-OES analysis. A 4.8 M acid concentration, 67.3 °C temperature and 57.1 min reaction time were determined as the optimum conditions of the reaction.

2.3. Economic Analysis

Those optimized parameters were entered as a data into the SuperPro Designer program. Silica production process was designed in a continuous mode. After the continuous operation of the process is determined, the raw materials, by-products,

utilities and products used in the whole process were defined in the program. Then equipment to be used in the process were selected. The silica production process consists of a continuously stirred tank reactor (CSTR), belt filtration, washing unit, drying unit and neutralization tank. The acid concentration of 4.8 M, reaction temperature of 67.3 °C and the reaction time of 57.1 min. were used as a reaction parameter in the SuperPro Designer program. The stoichiometric reaction was selected in the reactor. The reaction mixture at the end reaction was fed to the filtration unit. The amount of solid to be separated in the filtration unit was determined from the experimental results and used in the program. After the filtration unit, silica is fed to the washing units where soluble MgSO_4 salt was removed. Finally wet silica was dried in drying unit. The magnesium solution obtained from filtration was neutralized with ammonia to obtain magnesium sulfate and ammonium sulfate solution. The flow diagram drawn with the SuperPro Designer program in line with these data is shown Figure 2.

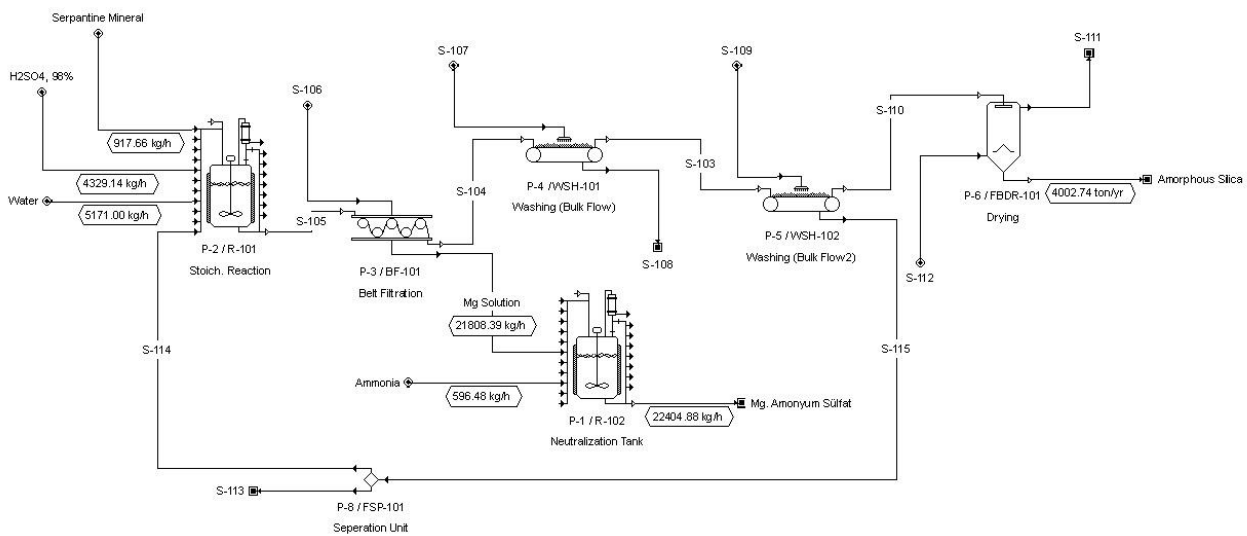


Figure 2: Flow diagram of the silica production process.

The economic analysis of the proposed facility was carried out by evaluating the facility capacity and purchase costs and production costs of the serpentine mineral. As seen in Table 1, total capital investment is obtained by summing total direct cost (TDC), total indirect cost (TIC), contingency (CFC), working capital and startup costs. For direct cost (DC), it consists of piping, facility construction, equipment cost, installation, and other related costs. Indirect costs consist of engineering and construction-related expenses. The economic parameters (e.g., purchase cost of raw materials and other consumables and selling price of products) were obtained from the market.

The total production cost was estimated from the mass and energy balances, prices of raw materials, chemicals, labor cost, and utilities as shown in Table 2. Transportation cost of raw materials and products to the plant and market was excluded from the production cost calculation, as it is assumed that the plant was built in close to the mining site. Labor and utility costs parameters were selected from the software database as given in Table 2. Reactor design parameters e.g., residence time, reaction temperature, conversion was obtained from experimental studies (Çakan, 2022). The solubility of magnesium sulfate was taken from the literature (Chen et al., 2023; Carmignano et al., 2020). A straight-line method was used for depreciation calculations in which a 10-year period and a salvage

value of 5% of the equipment purchase price were considered (Turton; et al. 2009). The feasibility of the suggested process is determined using the payback time (PBT) equation, which is given in Eqn. 5.

$$\text{Payback Time (years)} = \frac{\text{Total Investment}}{\text{Net Profit}} \quad (\text{Eq. 5})$$

Table 1: Total capital investment (US\$M) parameters and results for silica production process.

Items	Estimation approach	Plant capacity (t./y)			
		4000	8000	12000	16000
Total Direct Cost (TDC)					
Equipment purchase cost (PC)	Listed equipment cost	3.33	4.21	5.84	7.79
Installation	Equipment specific	1.22	1.60	2.15	2.89
Process piping	0.2 x PC	1.17	1.47	2.04	2.72
Instrumentation	0.1 x PC	1.33	1.69	2.34	3.12
Insulation	0.03 x PC	0.10	0.12	0.17	0.23
Electricals	0.1 x PC	0.33	0.42	0.58	0.78
Buildings	0.05 x PC	1.50	1.90	2.63	3.50
Yard improvement	0.1 x PC	0.50	0.63	0.87	1.17
Service facilities	0.2 x PC	1.33	1.69	2.34	3.12
Total Indirect Cost (TIC)					
Engineering and supervision	0.25 x TDC	2.70	3.43	4.74	6.34
Construction expenses	0.35 x TDC	3.79	4.81	6.64	8.87
Contractor's fee & Contingency (CFC)					
Contractor's fee	0.05 x (TDC + TIC)	0.86	1.10	1.52	2.03
Contingency	0.1 x (TDC + TIC)	1.73	2.20	3.04	4.05
Working Capital		1.19	2.36	3.54	4.72
Startup cost		1.00	1.26	1.74	2.33
Total Capital Investment (TCI = TDC + TIC + CFC)		22.11	28.91	40.25	53.69

Table 2. Operating cost parameters.

Items	Estimation Approach & Assumption
Total variable production costs	
Raw materials	From mass balance
Labor- dependent	Annual salary: 20,000 US\$
	Supervision factor: 0.15
Utility cost	Electricity: 0.10 US\$/kWh
	Steam: 12 US\$/MT
	Stream (high pressure) 20 US\$/MT
	Process water: 0.12 US\$/m ³
	Cooling water: 0.05 US\$/m ³
	Chilled water: 0.4 US\$/m ³
Maintenance & repair for Equipments	7% of the TCI
Laboratory cost for QC and QA	15% of the total labor cost
Operating supplies	15% of the equipment maintenance and repair cost
Royalties	4% of the capital cost
Fixed Charges	
Depreciation (10 year straight line)	Depreciated 5% of the TCI
Insurance	1% of the TCI
Plant overhead costs	50% of labor, equipment maintenance and repair cost
General Expenses	
Administrative costs	15% of operating labor cost
Distribution and marketing costs	No less than 2% of the total operating cost

3. RESULTS AND DISCUSSION

Serpentine mineral Mg₃Si₂O₅(OH)₄ is a good source of Mg and Si. Especially, serpentine is produced as tailing waste of chromite concentration plants in Türkiye. The utilization of these waste mineral for

production of magnesium products, such as MgSO₄ and Mg(OH)₂; and precipitated silica can be economic and feasible. Another issue is that the quantity of tailings has been increased with respect to chrome ore production in Türkiye (Top and Yıldırım, 2017).

Precipitated silica could be produced from both olivine and serpentine minerals. As the serpentine is more labile than olivine mineral based on the structural configuration, serpentine mineral is easily digested by acids. Secondly, as serpentine is obtained as a tailing waste during the chrome ore concentration, there is no need to extra mining processing. Because of those issues, serpentine mineral obtained from Ögelman Mining Inc., was used as raw material to produce silica and magnesium sulfate solution. The techno-economic analysis of silica production from serpentine mineral was performed using SuperPro Designer software.

3.1. Total Capital Investment

Technical and economic investigations of the silica production process from serpentine mineral were examined for different plant capacities. It allows the determination of annual operating cost (AOC), total capital investment (TCI) and unit production cost of amorphous silica. The necessary parameters in determining the technical analysis for the entire project were made using 2022 data. The construction of the facility, simulated with SuperPro Designer, started in 2022 and completion is expected to take 30 months. The project life is determined as 15 years, the number of annual working days is 330 days and the commissioning period is 4 months. Net present value (NPV) is calculated using 4% interest rate. The amortization of the capital investment is assumed to be 10 years and the initial cost of the salvage fee is assumed to be 5% of the equipment initial cost (Peters and Timmerhaus, 1991).

The total capital investment (TCI) equipment purchasing costs of the silica production facility were determined from the database of the program, and the costs of products and raw materials were determined from the global market prices. The size of the equipment and the number of equipment required for the capacity were calculated with the defined mass and energy balances. Care was taken to select stainless equipment suitable for the sulfuric acid used to dissolve the mineral in the reaction. The total capital investment of the amorphous silica production process is between US\$ 22.11 M and US\$ 53.69 M, depending on the capacity of the facility (4–16 kt/year), as shown in Table 2. In addition, it can be seen in Table 2 that the investment cost increases depending on the production amount in chemical plants. According to the examined facility capacities, the payback period of the investment was

determined as 5.3 years for 4,000 t/year. It was observed that by increasing the facility capacity by 12,000 t/year, the payback period decreased to 4.8 years. It was observed that there was no change in the payback period because of further increasing the facility's capacity. For this reason, 12,000 t/year was considered in the technical and economic analysis. The total capital investment required for the annual production of 12,000 t of amorphous silica was determined to be US\$ 40.25 M.

Increasing the capacity of the amorphous silica production facility had a direct impact on the number of equipment. Depending on the capacity, the purchasing costs of the necessary process units have increased. Total direct cost (TDC) is obtained by adding up the installation, process piping, instrumentation, insulation, electricity, buildings, facility construction, yard improvement and service facilities. These items are estimated by multiplying the equipment purchase cost by the coefficients specified in Table 1. For example, process piping is seen as 0.2 times the cost of purchasing equipment. The process piping cost was determined as US\$1.17 M and US\$2.72 M. for production capacity of 4,000 t/year and 16,000 t/year, respectively. After determining the total direct cost (TDC), total indirect costs (TIC) were calculated. Total indirect costs, engineering, and supervision are estimated at 0.25 times the total direct costs. Total non-direct costs were determined as US\$ 6.49 M at a production capacity of 4,000 t/year. Total indirect costs were determined as US\$ 15.21 M. at a production capacity of 16,000 t/year. The total direct cost and non-direct cost varied in the same way as the contractor's fee and contingency (CFC). Total capital investment (TCI) was determined by the sum of these variables. In the study, US\$ 22.11M, US\$ 28.91M, US\$ 40.25M. and US\$ 53.69M TCI were obtained in the production capacities examined as 4,000 t/year, 8,000 t/year, 12,000 t/year and 16,000 t/year, respectively.

Figure 3 represents the variation of both total capital investment and production cost with annual plant capacity ranging from 4,000 t to 16,000 t. As the plant capacity is increased the investment cost increased as well, which is common for the most chemical plants. However, a decrease in production cost was observed when plant production capacity has been risen. The minimum production cost was determined as US\$ 4.24/kg for the plant capacity of 12,000 t/yr.

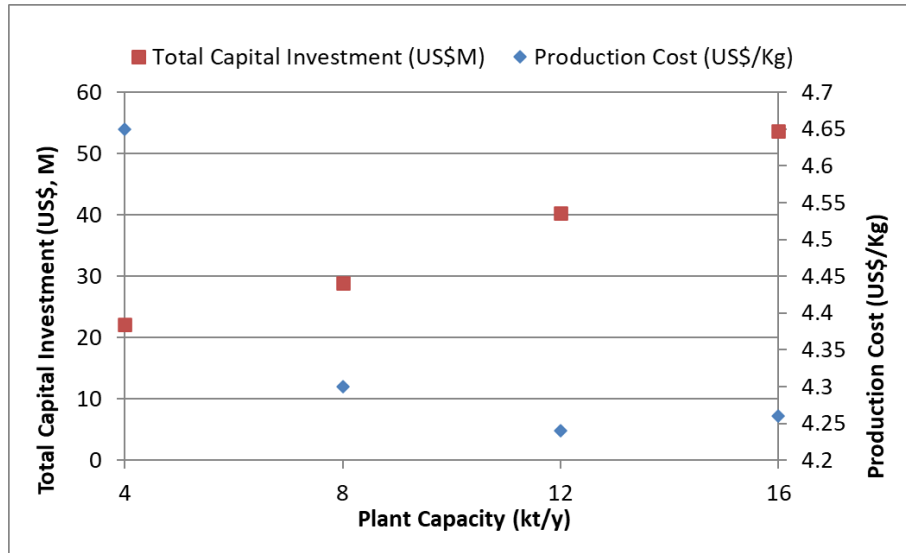


Figure 3: The effect of plant capacity on total capital investment and production costs.

On the other hand, payback time is a good indicator whether the investment is a good choice or not. For this reason, payback time was calculated for each plant capacity and given in Table 3. The minimum

payback time was obtained for 12,000 t annual silica production capacity. If there is a market demand for the silica where the plant would be constructed, this value is remarkable.

Table 3: Payback period of investment according to the plant capacity.

Plant capacity (t./y)	4000	8000	12000	16000
Payback Time (y)	5.32	5.20	4.77	5.86

3.2. Annual Operating Cost

Annual operating cost (AOC) was calculated as US\$45,588,000 for an amorphous silica production capacity of 12,000 t. Raw material cost was determined as the most important expense with 84.4% of the total cost of the facility. When the raw material cost was examined, it was seen that it the highest cost due to the price of sulfuric acid. The purchase price of sulfuric acid and serpentine was entered to the software as US\$ 300/t and US\$ 20/t, respectively. The second most important expense of the facility is facility maintenance, local taxes, insurance, equipment depreciation and other general expenses with 14.4%.

The silica production cost for annual plant capacity of 12,000 t using a purchasing cost of 20 US\$/t of serpentine mineral, was determined as US\$ 4.24/kg. The unit production income of the facility is calculated as US\$ 5.03/kg. The most important factors on which the amorphous silica production cost depends are raw materials (84.4%) and facility expenses (14.4%). In the amorphous silica production facility from the serpentine mineral, the purchase price of sulfuric acid constitutes a significant part of the raw material cost. Sulfuric acid (98%) is sold in the market between US\$ 250/t – US\$ 350/t. The purchase price of sulfuric acid was entered into the program as US\$ 300/t.

In the silica process, the production rates of magnesium sulfate solution and amorphous silica are determined as 407,963 t/year and 11,855 t/year, respectively. The revenue prices of these products

were entered into the program as US\$0.06/kg and US\$2.57/kg, respectively. In line with these data, the revenues of magnesium sulfate were calculated as US\$ 24.48 M and the revenues of amorphous silica was calculated as US\$29.65 M. The total revenue of the facility was determined as US\$ 54.12 M. Annual operating cost (AOC) is determined as US\$ 45.59 M/year. The gross profit of the facility is calculated as US\$ 8.53 M/year, taxes (40%) are US\$3.4 M/year, and the net profit is US\$ 8.44 M/year.

4. CONCLUSION

Serpentine mineral occurring as tailing waste in chrome ore mining was utilized for silica production. The feasibility analysis of the silica production process from serpentine mineral and sulfuric acid in an aqueous phase was performed from mass and energy balances calculated through modeling of the developed process at different annual capacities between 4,000 t - 16,000 t. The total capital investment for the silica production process was determined between US\$ 22.11 M - US\$ 53.69 M depending on the facility capacity ranging from 4,000 t/year to 16,000 t/year. The production cost of silica was determined as US\$4.24/kg for 12,000 t plant capacity. Total capital cost was determined to be US\$40,247,000, annual operating cost was US\$45,588,000, and total annual revenue for main product was US\$54,122,000. The payback period for 12,000 t/year amorphous silica production capacity was calculated as 4.8 years which is feasible value.

5. CONFLICT OF INTEREST

No potential conflict of interest was reported by the authors.

6. ACKNOWLEDGMENTS

Authors would like to thank Hayri Ögelman Mining Inc. for their support in providing serpentine mineral used as raw material in the experimental study.

7. REFERENCES

- Ballhorn, R. and Franke, W., (1996), EP0791559A1. European Patent Office, Frankfurt, DE.
- Carmignano, O. R. D., Vieira, S. S., Brandão, P. R. G., Bertoli, A. C., & Lago, R. M. (2020), Serpentinites: Mineral structure, properties and technological applications. *Journal of the Brazilian Chemical Society*, 31, 2-14.
- Chen, Y., Yang, X., Wu, L., Tong, L., & Zhu, J. (2023). Recovery of Mg from H₂SO₄ Leaching Solution of Serpentine to Precipitation of High-Purity Mg(OH)₂ and 4MgCO₃·Mg(OH)₂·4H₂O. *Minerals*, 13(3), 318
- Çakan, Y. (2022), Serpantin mineralinden amorf silica üretimi ve proses şartlarının optimizasyonu. (Publication No: 765850) (Master's dissertation, Süleyman Demirel University)
- Çakan, Y., & Gönen, M. (2022), Serpantin Mineralinden Amorf Silika Üretimi ve Proses Şartlarının Optimizasyonu. *Yekarum*, 7(2), 33-47.
- Çevik, E. (2006), Topuk Köyü Ve Civarındaki (Orhaneli, Bursa) Dünitlerin Mineralojik Ve Jeokimyasal Özellikleri Ve Olivin Açısından Endüstriyel Kullanımının Değerlendirilmesi (Doctoral dissertation, İstanbul Technical University, Fen Bilimleri Enstitüsü), İstanbul.
- Çiftçi, H., Arslan, B., Bilen, A., Arsoy, Z., & Ersoy, B. (2021). Optimization of leaching conditions for extraction of magnesium from a chromite beneficiation plant tailing predominantly containing lizardite. *Bulletin of the Mineral Research and Exploration*, 164(164), 251-259.
- Fedoročková, A., Plešingerová, B., Sučík, G., Raschman, P., & Doráková, A. (2014), Characteristics of amorphous silica prepared from serpentine using various acidifying agents. *International Journal of Mineral Processing*, 130, 42-47.
- Flörke, O.W., Graetsch, H., Brunk, F., Benda, L., Paschen, S., Bergna, H.E., Roberts, W.O., Welsh, W.A., Chapman, D.M., Ettliger, M., Kerner, D., Maier, M., Meon, W., Schmoll, R., Gies, H. Schiffmann, D. (2000). Silica. In *Ullmann's Encyclopedia of Industrial Chemistry*, (Ed.). https://doi.org/10.1002/14356007.a23_583
- Global Analysis Report, Precipitated Silica Market Size, Trends, Analysis 2023-2031 (transparencymarketresearch.com), Access date: February 05, 2024
- Gönen, M., Rodene, D. D., Panda, S., & Akcil, A. (2022), Techno-economic analysis of boric acid production from colemanite mineral and sulfuric acid. *Mineral Processing and Extractive Metallurgy Review*, 43(3), 402-410.
- Iler, R.K. (1979) *The Chemistry of Silica: Solubility, Polymerization, Colloid and Surface Properties, and Biochemistry*. John Wiley and Sons Ltd., New York.
- Lazaro, A., Brouwers, H. J. H., Quercia, G., & Geus, J. W. (2012). The properties of amorphous nano-silica synthesized by the dissolution of olivine. *Chemical Engineering Journal*, 211, 112-121.
- Lazaro, A., Chen, Y. X., Verhoeven, C., & Hendrix, Y. (2019). One-step synthesis of ordered mesoporous silica from olivine and its pore size tailoring. *Journal of Cleaner Production*, 238, 117951.
- Norton, L. D. (1993). Micromorphology of silica cementation in soils. In *Developments in Soil Science* (Vol. 22, pp. 811-824). Elsevier.
- Pietriková, A., Búgel, M., & Golja, M. (2004). Preparation of SiO₂ powder through leaching of serpentine. *Metalurgija*, 43(4), 299-304.
- Peters, M. S., Timmerhaus, K. D., & West, R. E. (1991). Cost estimation. *Plant design and economics for chemical engineers*, 150-215.
- Raza, N., Raza, W., Madeddu, S., Agbe, H., Kumar, R. V., & Kim, K. H. (2018). Synthesis and characterization of amorphous precipitated silica from alkaline dissolution of olivine. *RSC advances*, 8(57), 32651-32658.
- Top, S., & Yıldırım, M. (2017). Preparation of synthetic carnallite and amorphous silica from chromite beneficiation plant tailings. *Gospodarka Surowcami Mineralnymi*, 33.
- Turton, R., R. C. Bailie, W. B. Whiting, J. A. Shaeiwitz. (2009). *Analysis, synthesis and design of chemical processes*. Boston, MA: Pearson Education Inc.
- Zhou, S., Wei, Y., Li, B., Ma, B., Wang, C., & Wang, H. (2017). Kinetics study on the dehydroxylation and phase transformation of Mg₃Si₂O₅(OH)₄. *Journal of Alloys and Compounds*, 713, 180-186.



Effect of hBN on Response Times of PEO-Based Electrochromic Devices

Özge AKPINAR SARIHAN ^{#1,2}, İbrahim İNANÇ ^{#1,2}, Gediz UĞUZ^{#3}

¹ University of Ondokuz Mayıs, Nanoscience and Nanotechnology Program, Samsun, Turkey.

² University of Ondokuz Mayıs, Metallurgy and Materials Engineering Department, Samsun, Turkey.

³ University of Ondokuz Mayıs, Chemical Engineering Department, Samsun, Turkey.

Abstract: In this study, all solid state electrochromic devices (ECDs) without plasticizer such as propylene carbonate were fabricated by sol-gel spin coating method. WO₃ nanoparticles and PEO based polymer electrolyte solutions with hBN and without hBN nanoparticles were prepared. These solutions were sol-gel spin- and dip-coated on ITO-glass, respectively. For determining the effect of hBN nanoparticles, four configuration of ECDs were fabricated. The fast bleaching and coloring times of fabricated ECDs were obtained with hBN nanoparticles in WO₃ and PEO based polymer electrolyte thin films as 1.15 seconds. Glass/ITO/hBN-WO₃/hBN-PEO-based-polymer electrolyte/ITO/Glass electrochromic device is turned on and off 60 times. After 60 cycle, the device coloring time changed to 2-3 seconds, bleaching times changed to 30 seconds.

Keywords: Electrochromic devices, polymer electrolyte, sol-gel process, hBN nanoparticles.

Submitted: February 10, 2024. **Accepted:** March 22, 2024.

Cite this: Akpınar Sarihan, Ö., İnanç, İ., & Uğuz, G. (2024). Effect of hBN on Response Times of PEO-Based Electrochromic Devices. Journal of the Turkish Chemical Society, Section B: Chemical Engineering, 7(1), 69–76. <https://doi.org/10.58692/jotcsb.1435022>.

*Corresponding author. E-mail: ozgeakpinar86@hotmail.com

1. INTRODUCTION

Optical transmittance of electrochromic devices (ECD) are arranged reversibly and persistently by applying a small voltage (Pehlivan et al., 2014). An ECD has an ion conductive layer (electrolyte) is sandwiched between an electrochromic and ion storage layer. Electrochromic and ion storage are coated on transparent conductive electrodes. The device is protected by coating transparent conductive electrodes on plastic and glass surfaces. Ions are transferred between the ion storage and electrochromic layers through the electrolyte layer (Fu, 2010; Eren, 2018). The electrolyte layer, small ions such as protons H⁺ or lithium ions Li⁺, rarely Na⁺ and Ag⁺, are used (Eren, 2018; Solovyev et al., 2016).

Solid electrolytes have properties such as not leaking, easy to prepare, and perform good adhesion to electrolytes (Jeong et al., 2021). Polymer electrolyte consists of polymers and salt. PEO or PEO-derived polymers dissolved lithium salts well that do not allow crystallization even at low temperatures. Despite the advantages, Solid polymer electrolytes have low room-temperature conductivity (Fullerton-Shirey et al., 2010).

Usually, both crystalline and amorphous phases are present in polymer electrolytes. Amorphous phases have higher conductivity than crystalline phases, and ionic conductivity increases by adding plasticizers to amorphous phases (Fu, 2010). Polymer electrolyte conductivity is increased by the addition of nanoparticle filler (Fullerton-Shirey et al., 2010). Additionally, device's performance is increased by adding nanoparticles to polymer electrolytes (Pehlivan et al., 2014).

Tang et al. (2017) fabricated LiClO₄-PEO based ECD as an electrochromic layer, WO₃ film was coated by thermal evaporation, as ion storage layer TiO₂ film was coated by sol-gel dip coating method and the electrolyte layer LiClO₄/PEO/PC (1,3,3) were used. Optical modulation of 65% and 90k cycle stability were determined (Tang et al., 2017). The effects of SiO₂ and ITO nanoparticles on the electrochromic properties of polymer electrolytes were investigated (Pehlivan et al., 2014).

WO₃ is the most promising among electrochromic materials. Coloration occurs with the entry of ions into the WO₃ lattice, and bleaching occurs with the exit of the ions (Cremonesi et al., 2004). Adding metal nanoparticles such as Au, Ag and Pt enhances the coloration efficiency and durability of WO₃ nanoparticle films (Hoseinzadeh et al., 2017). hBN

nanoplates improve mechanical properties, ionic conductivity and thermal stability in comparison bulk hBN microparticles (Hyun et al., 2019). Electrolytes consisting of PEO/LiTFSI/h-BN show high ionic conductivity. The PEO/LiTFSI/h-BN electrolyte has better cycling stability (140 cycles) than PEO/LiTFSI without h-BN electrolyte (39 cycles) (Li et al., 2020).

The preparation methods are very sensitive to nanostructures. Also, there is a fragility of nanostructures and the deterioration of their structures when used with ECD devices with gel electrolytes (Xie et al., 2019).

This study aims to fabricate of cost effective ECDs consisting of WO_3 nanoparticles, polymer electrolyte without plasticizer such as propylene carbonate thin films by sol gel process, determining hBN nanoparticles effects on response times of these fabricated ECDs.

To the best of our knowledge, WO_3 /PEO-LiTFSI-hBN without propylene carbonate-based ECD has hitherto been unexplored for electrochromic applications.

2. EXPERIMENTAL SECTION

2.1. Preparation of WO_3 solutions with hBN and without hBN nanoparticles

WO_3 nanoparticles were dissolved with isopropanol (IPA) and deionized (DI) water (1:1:1 ratio) and the solution was mixed with a magnetic stirrer for 3 h at room temperature. For preparing the WO_3 solution with hBN, %2 hBN nanoparticles were added to the solution.

2.2. Preparation of PEO-based Polymer Electrolyte with and without hBN

LiTFSI was dissolved in acetonitrile (ACN) at room temperature for 1 h. After adding PEO to the solution, it is mixed for 5 hours. To prepare polymer electrolyte solution with hBN, 1% hBN nanoparticles were added.

2.3. Fabrication of Four Types of Electrochromic Devices

ITO/glasses were cleaned with acetone, ethanol, and IPA, respectively for 5 minutes in an ultrasonic cleaner. WO_3 solutions were spin-coated on conductive transparent ITO-glass at 2000 rpm for 20 seconds and annealed at 100 °C for 10 min. This process was adapted from Jeong (2021) to a thickness of $1 \mu\pm 0.1$ (Jeong et al., 2021). Polymer electrolytes were dip coated at a speed of 1 mm/s on conductive transparent ITO-glass substrates and annealed at 100 °C for 10 min. These two processes are repeated three times. This process was adapted from Zhang et al. (2015) to a thickness of $30 \mu\pm 2$. WO_3 and polymer electrolyte thin films were sandwiched. Edges of ECDs were sealed with silicon guns so humidity that disturbs devices was prevented. Four types of ECDs were fabricated. WO_3 thin films were fabricated with hBN and without hBN by sol-gel spin coating method and polymer electrolytes were fabricated with hBN and without hBN by sol-gel dip coating method. They were sandwiched in four configurations as given in Table 1.

Table 1: Four configurations of ECDs.

Device	Cathode	Electrolyte
ECD1	WO_3 /hBN	PEO/LiTFSI/ hBN
ECD2	WO_3	PEO/LiTFSI/hBN
ECD3	WO_3 /hBN	PEO/LiTFSI
ECD4	WO_3	PEO/LiTFSI

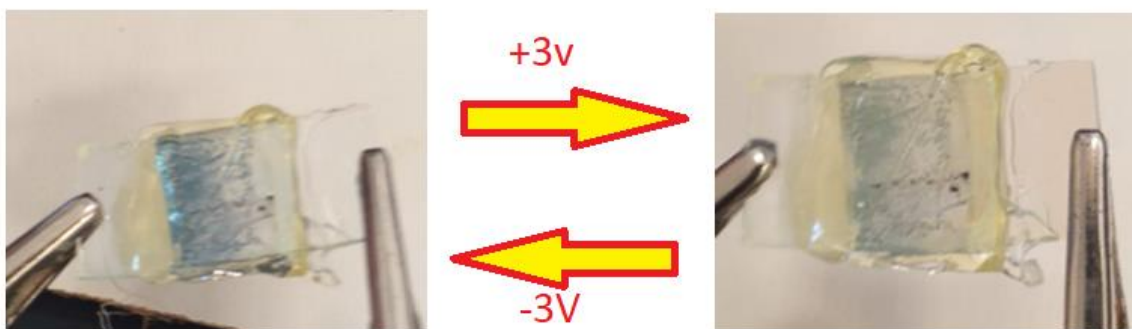


Figure 1: Fabricated ECD based on WO_3 with hBN, polymer electrolyte without hBN.

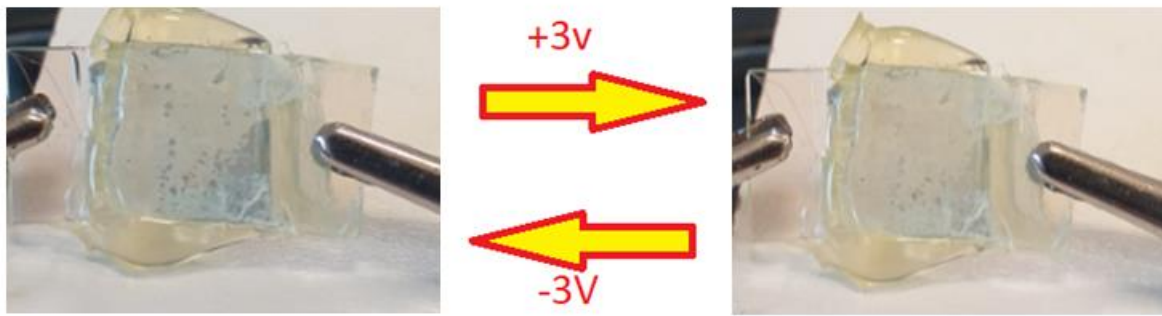


Figure 2: Fabricated ECD based on WO_3 without hBN, polymer electrolyte without hBN.

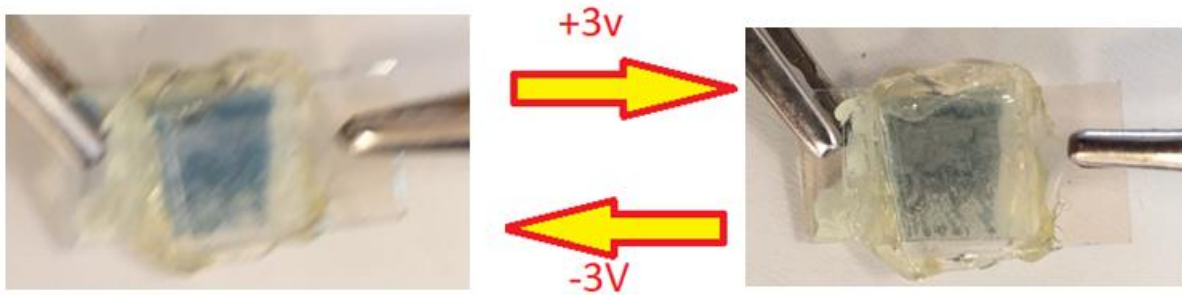


Figure 3: Fabricated Electrochromic Device based on WO_3 without hBN, polymer electrolyte with hBN.

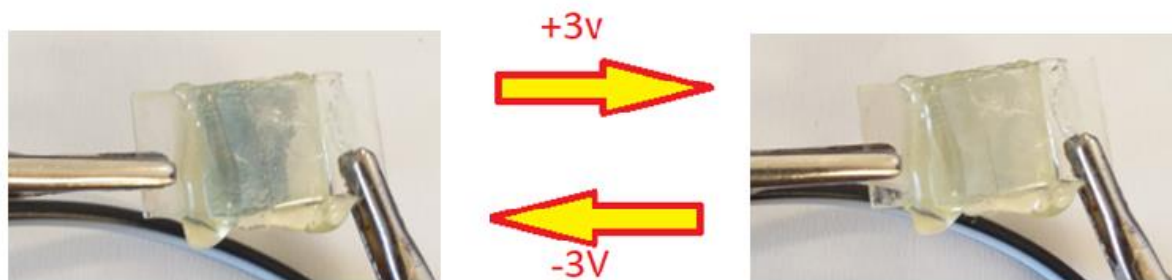


Figure 4: Fabricated Electrochromic Device based on WO_3 with hBN, polymer electrolyte with hBN.

3. RESULTS AND DISCUSSIONS

3.1. Scanning Electron Microscopy (SEM) Results of the WO_3 and Polymer Electrolyte Thin Films

Figure 5 shows SEM images of thin films. Figure 5a shows that the WO_3 thin film is highly porous with a large active surface area. Figure 5b shows a polymer electrolyte thin film that has a smooth surface and clumps of hBN embedded unsmooth.

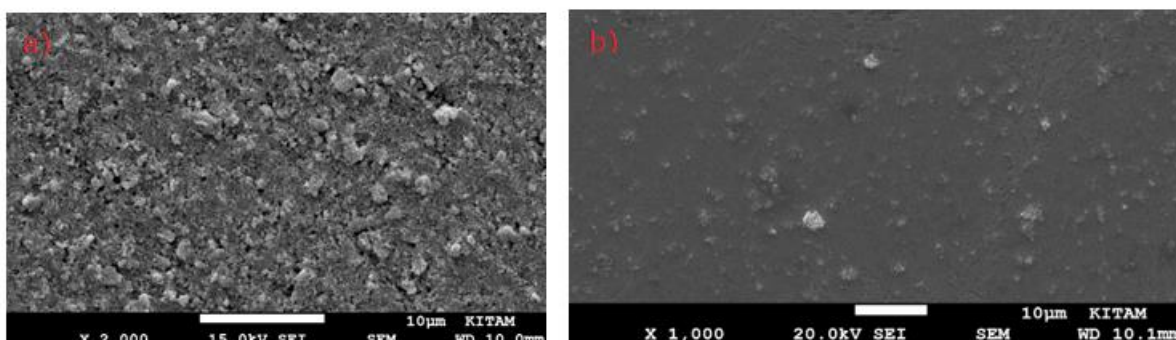


Figure 5: SEM Image of WO_3 at 2 kx and polymer electrolyte thin film at 1 kx.

Figure 6 shows the EDX (Energy Dispersive X-Ray) spectra of thin films. Figure 6a provides evidence for the chemical quality of WO_3 thin film. The EDX spectrum exhibits the characteristic peaks of Oxygen,

Tungsten, Indium and Tin in the film. Tungsten and Oxygen peak from the Tungsten oxide phase and Indium and Tin peak from the ITO phase. However, the absence of any other peaks except these elements is evidence of the chemical quality of grown films without any elemental impurities. Figure 6b displays the EDX elemental analysis of polymer

electrolyte. Au peaks are observed in EDX spectra. Au coating of samples was required in the SEM to enable the imaging of samples. Carbon and Oxygen are obtained from the PEO phase; Fluorine and sulfur elements are obtained for the formation of LiTFSI. At the same time, relatively smaller amounts of Pd and Cu are observed.

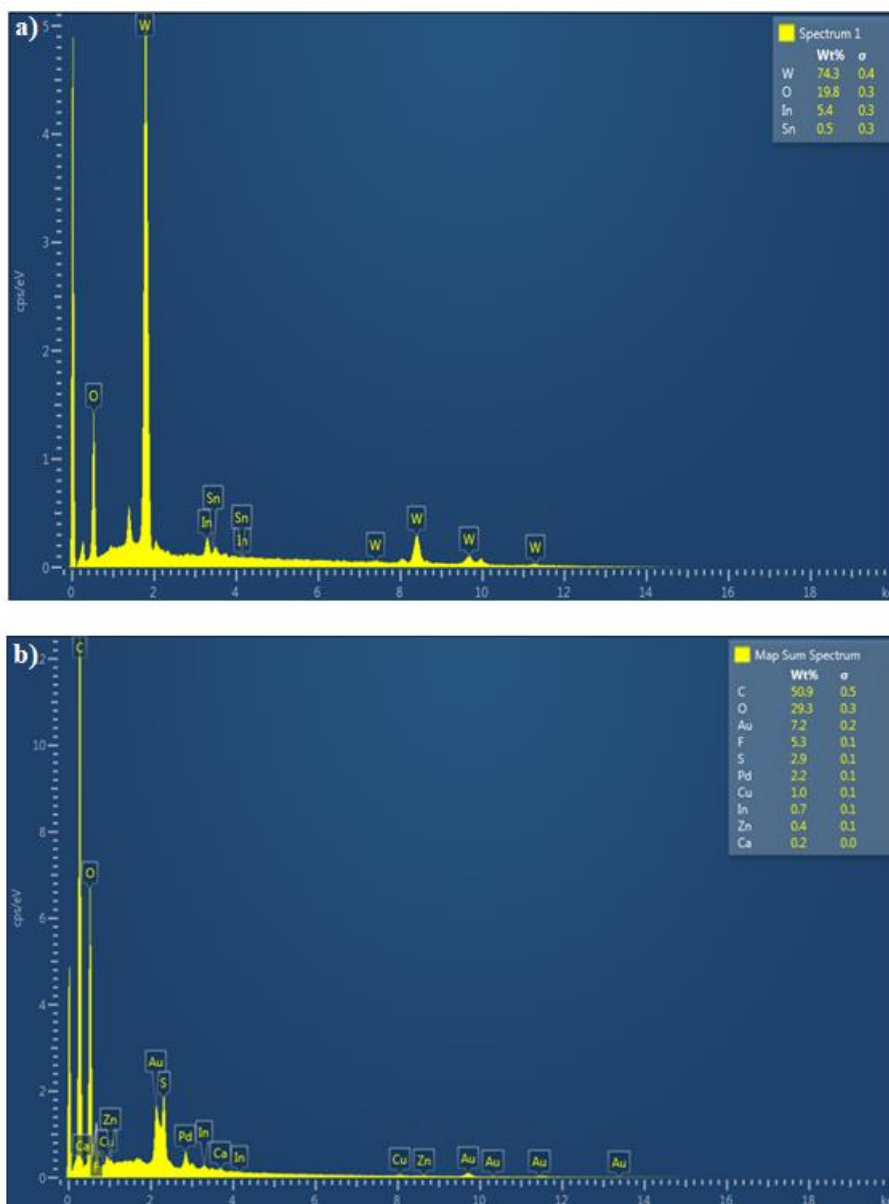


Figure 6: EDX spectrum of a) WO_3 , b) polymer electrolyte thin film.

3.2. Fourier Transform Infrared Spectroscopy (FTIR) Results of Polymer Electrolyte Thin Films

FTIR spectrum of polymer electrolyte thin film is displayed in Figure 7. FTIR results show the bands appeared around $3500\text{-}3600\text{ cm}^{-1}$ were assigned for O-H group and intermolecular bonding. The

vibrational frequency corresponding to CH_2 rocking mode appears at $700\text{-}800\text{ cm}^{-1}$. For asymmetric SO_2 stretching mode and S- CF_3 bonding mode, wavenumbers are spotted at 1447 and 2250 cm^{-1} . For the C- SO_2 -N bonding mode of LiTFSI wavenumber is at 1377 cm^{-1} . N-S bonding mode is obtained at 3170 cm^{-1} wavenumber. C-H bonding mode exists between $2900\text{-}3000\text{ cm}^{-1}$ wavenumbers.

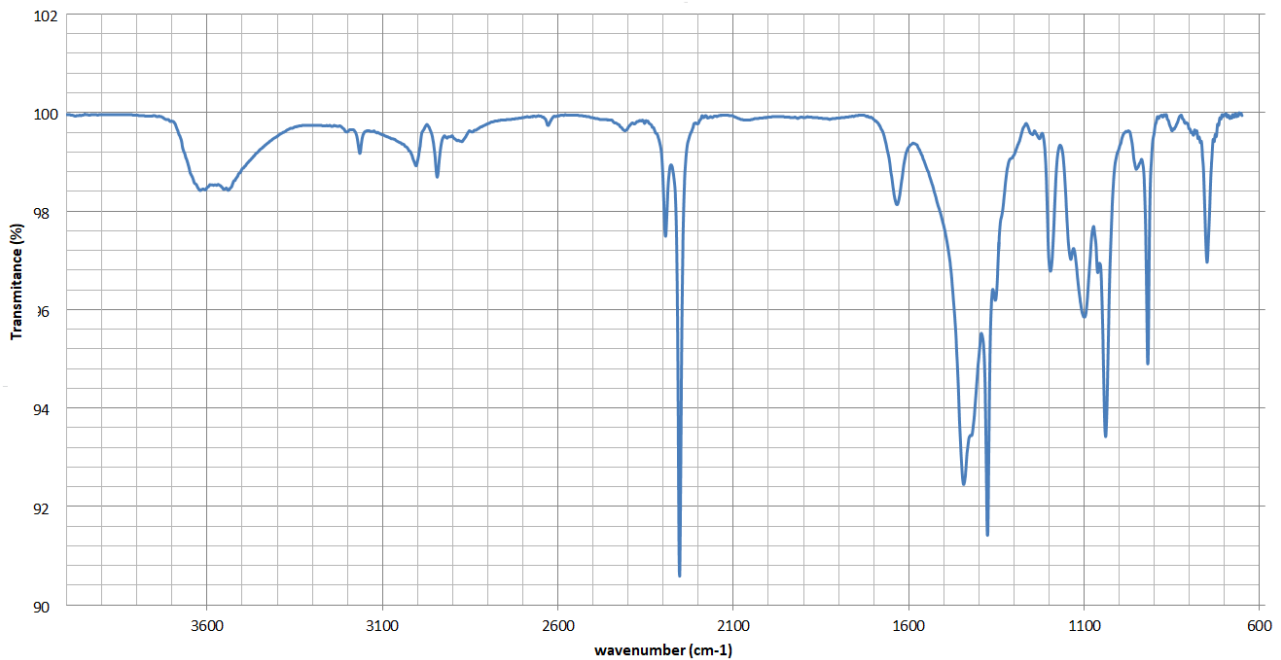


Figure 7: FTIR spectrum of polymer electrolyte with LiTFSI.

3.2. UV-Visible (UV-Vis) Spectroscopy Results of Polymer Electrolyte and WO₃ Layer

UV-Vis spectra of polymer electrolyte layer and WO₃ cathode layer are shown in Figure 8. The UV-Vis spectrum of polymer electrolyte thin film for the wavelength range of 300 and 800 nm is displayed in Figure 8a. It is clear that the transparency of the film increases with increasing wavelength. Transparency ranges between 80-90% which is ideal for ECDs. In

Figure 8b, The UV-Vis image of a WO₃ thin film for wavelength range of 300 and 800 nm is displayed. Transmittance of WO₃ coated on PET-ITO increases with increasing wavelength. From the transmission spectrum, it is clear that the transparency of the film increases with increasing wavelength. Transparency of the film is suitable for electrochromic devices and similar to Zhang et al. (2022).

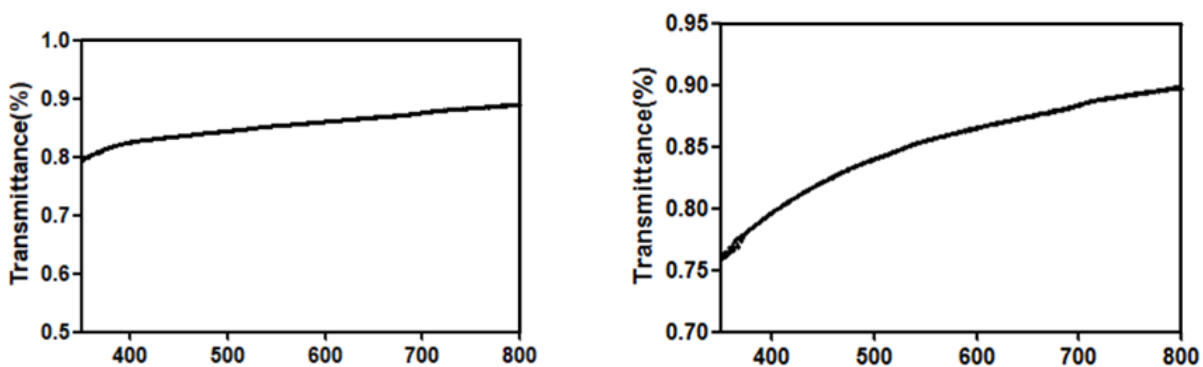


Figure 8: UV-Vis spectra of polymer electrolyte and WO₃ layer. The X axes are wavelength.

3.2. X-ray Diffraction (XRD)

XRD technique was used to obtain the crystallographic structure of WO₃-coated on PET-ITO. WO₃ nanoparticles that were purchased from Nanografi company have a high purity of 99.99% in the orthorhombic phase and a size between 20-60 nm. In Figure 9, XRD spectrum of WO₃ thin film is displayed. Strong and sharp diffraction peaks are

observed at $2\theta = 23.1^\circ, 23.6^\circ, 24.4^\circ, 26.5^\circ, 28.8^\circ, 33.3^\circ, 34.2^\circ, 41.7^\circ, 53.5^\circ, 55.9^\circ$, all of which are associated to the (002), (020), (200), (120), (112), (022), (202), (222), (400) and (420) crystalline planes of the orthorhombic phase of WO₃ with a good crystallization which is important for stability.

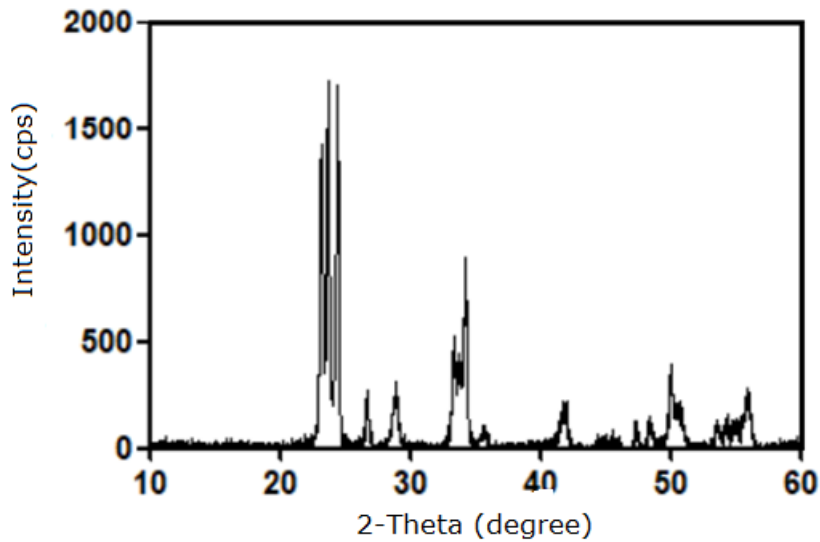


Figure 9: XRD spectrum of WO₃ thin film.

3.3. Performance of ECDs

The bleaching and coloring time of fabricated ECDs in this study was obtained in nearly 1-2 seconds. Reasonably good response times are obtained compared to the coloration and bleaching times in the literature. Glass/ITO/hBN-WO₃/hBN-PEO Electrolyte/ITO/Glass configuration of ECD cycled 60 times. After 60 cycles, the device coloring time changed to 2-3 seconds and bleached times changed to 30 seconds.

In Table 2, measured with standard deviation of these values, coloring (t_c) and bleaching (t_b) times of fabricated ECDs with hBN and without hBN are displayed. Results were determined by taking the average of 10 cycles of ECDs. Figure 9 shows adding hBN for both electrolyte and electrochromic layer decreases coloring (t_c) and bleaching (t_b) times of ECDs

Table 2: Coloring and bleaching times of four configurations of ECDs.

Sample	Cathode	Electrolyte	t_c (s)	t_b (s)	STD (t_c (s))	STD (t_b (s))
ECD1	WO ₃ with hBN	PEO/LiTFSI/ hBN	1.15	1.15	0.24	0.24
ECD2	WO ₃	PEO/LiTFSI/hBN	1.65	1.51	0.21	0.44
ECD3	WO ₃ with hBN	PEO/LiTFSI	2.27	1.97	1.43	1.17
ECD4	WO ₃	PEO/LiTFSI	1.50	2.14	1.28	1.49

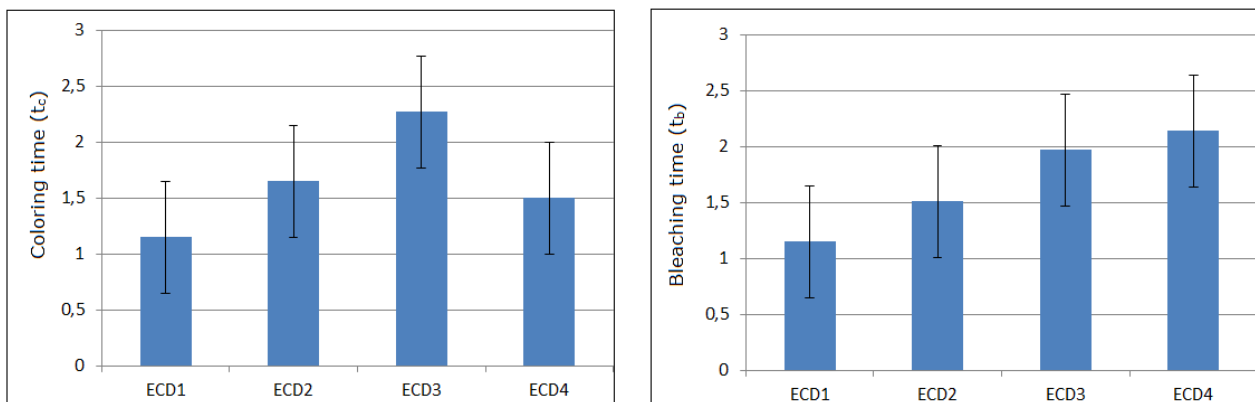


Figure 10: Graphics of coloring and bleaching times of four configuration of ECDs.

The transmittance of ECD1 was measured by a fabricated Arduino-based electronic device in our thin film laboratory. In Figure 10, the transmittance of

ECD1 is displayed for 10 s switching time. Coloring (t_c) and bleaching (t_b) times were obtained as a few seconds. Transmittance changes from 64 to 59% or

vice versa. The results of transmittance in Figure 10 are consistent with the results of Xie (2019).

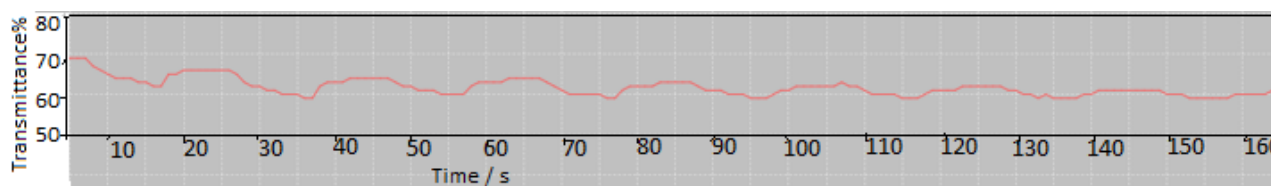


Figure 11: Transmittance over time of fabricated ECD1 for 10 seconds interval switching.

4. CONCLUSION

All solid-state electrochromic devices (ECDs) without plasticizers, such as propylene carbonate, were fabricated by the sol-gel spin coating method. PEO-based polymer electrolytes and WO_3 solutions with and without hBN were prepared successfully. WO_3 solution and polymer electrolyte were spin and dip coated respectively on ITO-glass substrate. After annealing, thin films were sandwiched and four types of ECDs were fabricated. Colored and bleached states were obtained by giving -3 V and +3 V voltage from the edges. The bleaching and coloring time of ECD1, ECD2, ECD3 and ECD4 are 2.14-1.5, 1.97-2.27, 1.51-1.65, and 1.15-1.15 seconds, respectively. These results show that hBN nanoparticles for both electrochromic and electrolyte layers decrease the switching times. The fast bleaching and coloring times are obtained from ECD1. ECD1 was cycled 60 times. After 60 cycles, the device coloring time changed to 2-3 seconds and bleached times changed to 30 seconds.

For the characterization of WO_3 cathode and polymer electrolyte layers, SEM, EDX, UV-Vis and FTIR characterization techniques were used. SEM results show that smooth and homogenous thin films are obtained. EDX spectrum shows chemical composition. EDX results prove the chemical quality of grown layers without any elemental impurities. UV-Vis results show that between 300-800 nm range polymer electrolyte and WO_3 cathode layers have enough transmittance for ECDs. The WO_3 film coated on ITO/Glass substrate exhibits %85 transmission at 550 nm. Chemical bonds of the polymer electrolyte layer are determined with FTIR.

5. REFERENCES

- Cremonesi, A., Bersani, D., Lottici, P. P., Djaoued, Y., Ashrit, P. V. (2004). WO_3 thin films by sol-gel for electrochromic applications. *Journal of Non-Crystalline Solids* 345&346, 500-504.
- Eren, E. (2018). Li⁺ doped chitosan-based solid polymer electrolyte incorporated with PEDOT:PSS for electrochromic device. *Journal of the Turkish Chemical Society*. 5(3), 1413-1422.
- Fu, X. (2010). Polymer electrolytes for electrochromic devices. *Electronic and Optical Materials*, 471-523.
- Fullerton-Shirey, S. K., Maranas J. (2010). Structure and Mobility of PEO/LiClO₄ Solid Polymer Electrolytes Filled with Al₂O₃ Nanoparticles. *J. Phys. Chem. C*, 114, 9196-9206.
- Hoseinzadeh, S., Ghasemiasl, R., Bahari, A., Ramezani, A. H. (2017). The injection of Ag nanoparticles on surface of WO_3 thin film: enhanced electrochromic coloration efficiency and switching response. *J Mater Sci: Mater Electron*, 28, 14855-14863.
- Hyun, W. J., Moraes, A. C. M., Lim, J. M., Downing, J. R., Park, K. Y, Tan, M. T. Z., Hersam, M. C. (2019). High-Modulus Hexagonal Boron Nitride Nanoplatelet Gel Electrolytes for Solid-State Rechargeable Lithium-Ion Batteries. *ACS Nano*, 13, 9664-9672.
- Jeong, C.Y., Kubota, T., Chotsuwan, C., Wungpornpaiboon, V., Tajima, K. (2021). All-solid-state electrochromic device using polymer electrolytes with a wet-coated electrochromic layer. *Journal of Electroanalytical Chemistry*, 897, 115614.
- Li, Y., Zhang L., Sun Z., Gao G., Lu S., Zhu M., Zhang Y., Jia Z., Xiao C., Bu H., Xi K., and Ding S. (2020). Hexagonal boron nitride induces anion trapping in a polyethylene oxide based solid polymer electrolyte for lithium dendrite inhibition. *J. Mater. Chem. A*, 8(19), 9579-9589.
- Pehlivan, İ. B., Marsal, R., Pehlivan, E., Runnerstrom, E. L., Milliron, D. J., Granqvist, C. G., Niklasso, G. A. (2014). Electrochromic devices with polymer electrolytes functionalized by SiO₂ and In₂O₃:Sn nanoparticles: Rapid coloring/bleaching dynamics and strong near-infrared absorption. *Solar Energy Materials & Solar Cells*, 126, 241-247.
- Solovyev, A. A, Zakharov, A. N., Rabotkin, S. V. Kovsharov, N. F. (2016). Electrochromic Device with Polymer Electrolyte. *Journal of Electronic Materials*, 45(8), 3866-3871.
- Tang, X., Chen, G., Liao, H., Li, Z., Zhang, J., Luo, J. (2020). Unveiling mechanical degradation for a monolithic electrochromic device: Glass/ITO/ WO_3 /LiClO₄ (PEO)/TiO₂/ITO/glass. *Electrochimica Acta*, 329, 135182.

- Xie, Z., Liu, Q., Zhang, Q., Lu, B., Zhai, J., Diao, X. (2019) . Fast-switching quasi-solid state electrochromic full device based on mesoporous WO₃ and NiO thin films. *Solar Energy Materials and Solar Cells*, 200, 110017.
- Zhang, B., Luo, J., Chen, Z., Wu, L., Li, J., Tian, Y., Liu, S. (2022). Synthesis, characterization and dual-band electrochromic properties of Nb-doped WO₃ films. *Journal of Electroanalytical Chemistry*, 918.
- Zhang, Y., Zhao, Y., Gosselink, D., Chen, P., (2015). Synthesis of poly(ethylene-oxide)/nanoclay solid polymer electrolyte for all solid-state lithium/sulfur battery. *Ionics*, 21, 381-385.